UNIVERSITY OF GENOVA

POLYTECHNIC SCHOOL

DIME

Department of Mechanical, Energy, Management

and Transportation Engineering

PH.D. IN MACHINES, ENERGY STYSTEMS, ENVIRONMENTAL
AND TRANSPORT ENGINEERING

Curriculum: Machines, Energy Systems, Environmental and Propulsion
Engineering

Surge Detection in Turbocharger Compressors for Automotive Application and Development of a Control-Oriented Model

Tutor: Prof. Silvia Marelli

Candidate: Anna Misley

May 22nd, 2020

Abstract

The increasingly strict regulations on emissions and fuel consumption of internal combustion engines for automotive applications has pushed researchers and manufacturers to develop new technologies and control strategies. One of the solutions widely adopted for gasoline engines is downsizing coupled with turbocharging. While this improves an engine's emissions and fuel consumption, turbocharging has its own challenges. The limitation to high performance boosting and boost pressure control lies in the difficulty of predicting and controlling the instability phenomenon that occurs in centrifugal compressors for small mass flow rates. Many different approaches have been followed to study and analyze the behavior of the compressor during this unstable operation and many different models have been developed as a result: ranging from high-fidelity multi-dimensional models to simplified lumped parameter models. The development of control-oriented models is still limited due to the difficulty of accurately representing the complex fluid dynamic phenomena occurring in the compressor while being able to execute on embedded hardware in real time. This work will identify the main causes that lead to a transition from stable to unstable behavior which will provide the knowledge required to develop a control-oriented model.

This work describes the design of two experimental investigations performed at the University of Genoa test bench and the development of a one-dimensional distributed-parameter model of the centrifugal compressor and piping system. The aim of the first experimental investigation was to analyze the behavior of the compressor in stable conditions far from and close to the stability limit and to investigate the effect of the compressor outlet circuit on the transition to unstable behavior. The data and the knowledge collected were used to develop a compressor and piping system model that could represent the physical phenomena observed. Following the development of the model, the second experimental investigation was performed to collect data to calibrate and validate the model. The second experimental investigation also offered the opportunity to study the behavior of the compressor during deep surge in more detail. Specifically, the increased number of measurements allowed for study of the shape and position of the cycles occurring during deep surge conditions. The model was then used to perform a preliminary analysis of the parameters and loss mechanisms that cause a transition from stable to unstable behavior.

I

Table of Contents

List of Figures

VII

VIII

List of Tables

1 Introduction

Internal combustion engines have been the predominant mean of propulsion in passenger cars. The power to weight ratio, the compactness, the light weight and the low production cost of this energy system are four of the reasons why internal combustion engines have been used in passenger cars since the early development of vehicles. The main quality that makes internal combustion engines so desirable, however, is their ability to perform fast transients and work at high efficiency in off-design operating conditions.

In the last forty years, significant attention has been focused on the emissions produced by automotive internal combustion engines. The European Commission (EC) and the United States of America Environmental Protection Agency (EPA) have introduced progressively stricter regulations to limit the production of NO_x, CO, HC, soot particles and CO_2 [1]. In addition to these severe regulations, the tests that evaluate the pollutants produced by vehicles have been redesigned to better represent the behavior of vehicles on the road and put an even tighter belt on engine design and control. The Worldwide harmonized Light vehicles Test Cycles (WLTC) took effect on the 1st of September 2017; it is based on the statistical analysis of real-world driving data instead of the previously used and outdated EC's New European Drive Cycle (NEDC) [2] The length of the tests in terms of kilometers and time and the number of accelerations and decelerations increased with respect to the NEDC. Manufacturers have therefore been obliged to develop new technologies to reduce fuel consumption, without compromising vehicle performance and drivability.

Many different technologies have been introduced to reduce emissions in gasoline and diesel engines. The most effective solution adopted in gasoline engines is the three-way catalyst, which reduces the emissions of HC, CO and NO_x, bringing the production below the regulation targets. The reduction of CO_2 emissions, though, is correlated to the fuel consumption; requiring the improvement in the system's efficiency or new vehicle architectures. Electric and hybrid propulsion systems have also been introduced in the market in an attempt to curb fuel consumption. At the same time, substantial efforts are being dedicated to improving the capabilities and efficiencies of internal combustion engines. The main strategies introduced for gasoline engines include: Variable Valve Actuation, Gasoline Direct Injection (GDI) and downsizing coupled with turbocharging [3], [4], [5]. Downsizing is always coupled with turbocharging to maintain a similar engine power output and vehicle performance. Reducing the displacement of the engine increases the global efficiency for two reasons: the reduction of rotating masses reduces the friction losses, and the reduction of cylinder surface area reduces the heat losses. In addition, the increase in mean effective pressure produced by the compressor reduces the specific fuel consumption.

In this scenario, a detailed knowledge of the behavior of the turbocharger and the engine is fundamental to develop efficient systems [6], [7], [8], [9], [10]. The components' behavior in all operating conditions also provides information for optimal matching of the engine and the turbocharger, as shown in Fig. 1.1 where the engine map is contained within the turbocharger steady-state map.

1
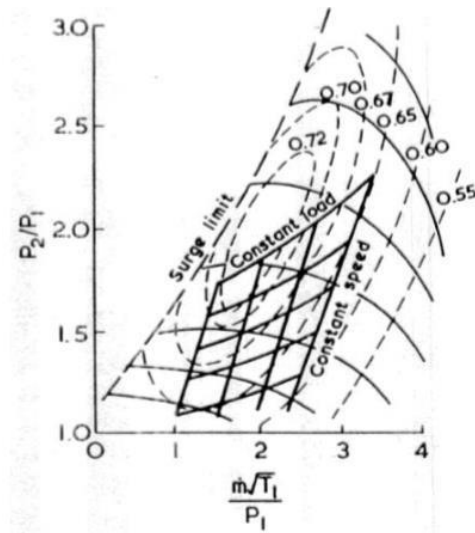
Fig. 1.1 – Engine-Turbocharger Matching. Adapted from [11]

The high efficiency areas of the compressor are close to the surge line, in Fig 1.1 these are shown as a dashed contour map. Working in proximity of the surge line allows operating conditions with the highest global efficiency of the whole system. Identifying the position of the surge line would allow the designer to match the two machines in a wider range of operating conditions and exploit the high efficiency part of the turbocharger map. The engine and turbocharger are coupled in lower efficiency areas to keep the compressor operating condition far from the unstable region, because the stationary map does not consider the dynamic effects that can lead to instability in certain transients. During fast engine transients, the compressor operating condition can cross the surge line and become unstable, this scenario is shown in Fig. 1.2.
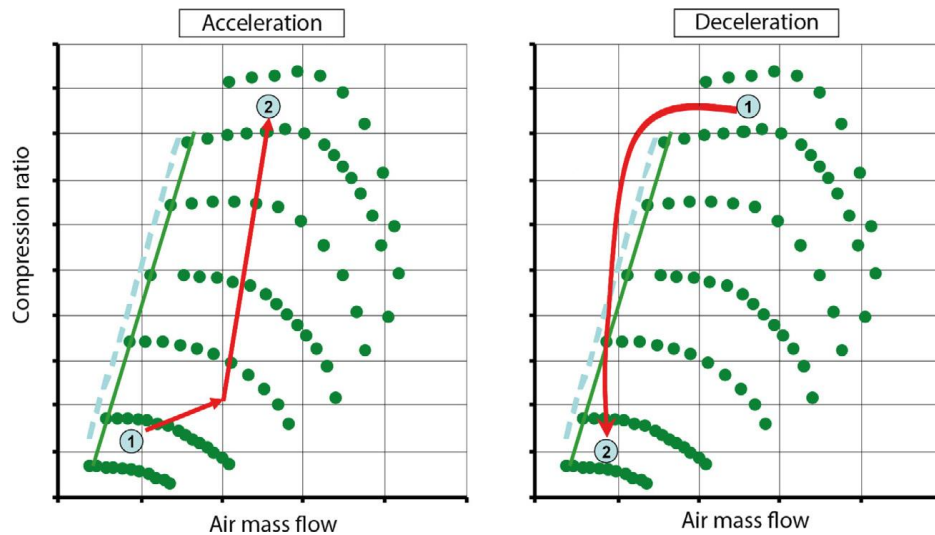
Fig. 1.2 – Acceleration and Deceleration Transients. Adapted from [12]

2

Mass flow rate, pressure and turbocharger rotational speed oscillations appear during surge. These oscillations cause noise and vibration in the compressor, which can lead to the failure and damage of the compressor blade as well as stress on the shaft and bearings of the turbocharger if the compressor operates in surge for an extended amount of time. Surge is a global instability phenomenon generated by the interaction between the compressor and the intake and exhaust pipe system surrounding the compressor. The different time scales that govern compressor and pipe system behavior generate oscillations in the pressure along the system, reflecting in mass flow rate and turbocharger speed oscillations. When the compressor operating condition becomes unstable, the reduction in compressor outlet pressure generates an imbalance in the pressure gradients along the system which triggers an oscillating behavior, called surge. When the mass flow rate oscillations are limited and flow direction does not reverse, the behavior is defined as mild surge, while when the flow reverses and the cycle extends to the negative mass flow rate region of the compressor map, the behavior is defined as deep surge. The different surge cycles corresponding to mild and deep surge are shown in Fig. 1.3.
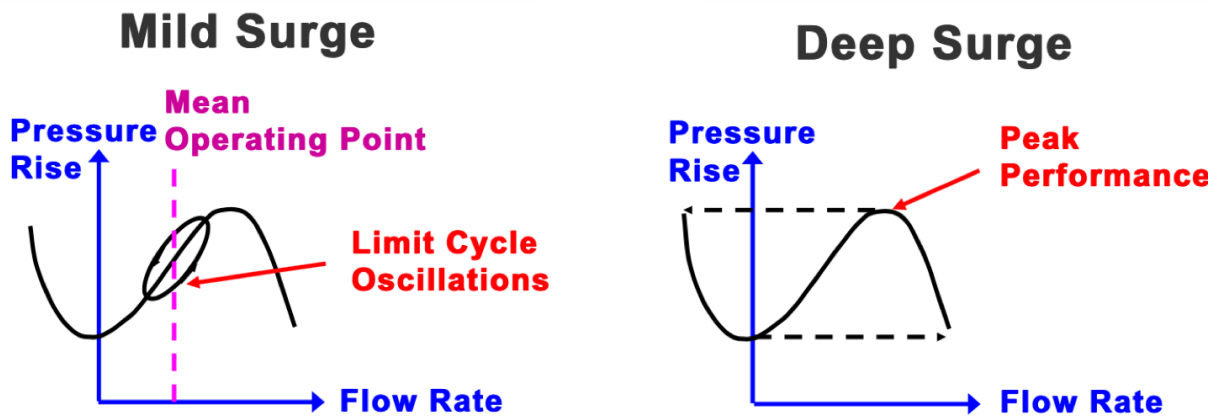
Fig. 1.3 – Mild and Deep Surge. Adapted from [13]

The analysis of surge has gathered considerable interest in recent years, as it is the limiting factor to achieving stable operations of the compressor at high boost pressure conditions [14], [15], [16]. In fact, poor knowledge of the physical phenomena that lead to the onset of surge will inevitably require engine designers and control engineers to adopt conservative methods, thereby limiting the benefits that could be achieved with boosting technologies.

In 1976, Greitzer introduced a mathematical model to describe the instabilities of axial compressors and confirmed his theory with experimental results [17], [18], [19]. Greitzer modeled the compression system by describing the behavior of three components, shown in Fig. 1.4: the compressor installed in a pipe system, a plenum and a throttle valve. Compressor and valve are characterized by the lengths L_c and L_t and by the sections S_c and S_t; the plenum is characterized by its volume V_p. The variables of the model are the pressures and the mass flow rate at each component. The assumptions are the following: the flow is incompressible, one-dimensional and non-viscous; the compression is isentropic; the temperature is constant throughout the system; the pressure in the plenum is uniform and the fluid contained in it is at rest; and finally, the valve is quasi-static.

3
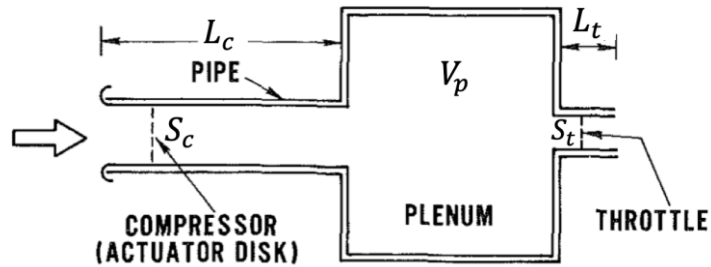
Fig. 1.4 – Greitzer's Schematic Representation of the Compressor System. Adapted from [10]

The model consists of four ODEs: the first three are derived from the conservation of mass and momentum for the 3 components of the system, while the fourth describes the rotating stall phenomena. In centrifugal compressors, representing rotating stall with a single ODE is too complicated. In addition, more recent studies of centrifugal compressors do not show the rotating stall behavior Greitzer describes in axial compressors before entering surge [20], [21]. For this reason, the equation that described rotating stall is neglecting when analyzing centrifugal compressors. The compressor mass flow rate dynamics are largely driven by the difference between the plenum pressure and the compressor pressure (compressor characteristic) at the same compressor speed and mass flow. The compressor characteristic is modeled with a cubic relationship with respect to mass flow. The throttle mass flow rate is driven by pressure difference across the throttle. The mass flow rate dynamic equations are a result of the momentum conservation in each component, while the equation for the dynamic pressure rise derives from the mass conservation in the plenum.

Following studies by Hansen et al. confirmed the validity of Greitzer's model also for centrifugal compressors [22], [23]. Hansen conducted a thorough experimental investigation on a small centrifugal comparison and compared the experimental data to the model calculations, validating Greitzer's model. Hansen then performed a stability analysis and correlated the maximum mass flow rate perturbation that maintained stable conditions. This procedure was performed for different valve positions. Greitzer's lumped parameter model can well represent the pressure and mass flow rate oscillations that occur during surge behavior but does not consider many of the parameters that affect surge and the transition into surge.

Many experimental studies have been conducted to analyze, in detail, different geometrical and physical aspects that could generate a transition into surge [24]. Kosuke Toyama et al. performed a very thorough investigation aimed at analyzing instantaneous signals in the compressor and at identifying parameters that could help explain the physical phenomena that lead to surge [20]. He noted that when the diffuser-inlet pressure recovery factor reached a value of 0.4, the flow at the diffuser inlet deteriorated and surge occurred. This work also highlighted the importance of analyzing the interactions between the compressor and the circuit in which it was installed, which was studied in a work by Marelli et al. [25]. Marelli analyzed the effect of circuit geometry on the position of the surge line by varying the compressor outlet circuit volume and length, showing that in steady conditions the geometry does not affect the stability limit. Galindo et al. showed the effect of compressor inlet circuit geometry on the minimum mass flow rate reachable in stable conditions [12]. Galindo designed and tested four different compressor inlet circuit configurations, shown in Fig. 1.5. Configuration (a) is the reference and

4

consists of a constant-diameter straight tube which guarantees a fully developed flow at the compressor inlet (L> 10D). Configuration (b) is characterized by a conical narrowing placed at a fixed distance from the rotor. Configuration (c) is a convergent-divergent nozzle optimized to minimize total pressure losses; Configuration (d) is a converging nozzle, obtained by removing the part placed after the restriction from configuration (c). The work by Galindo highlighted the improvement on the surge margin of the different configurations. Configurations (b) and (c) move the surge margin to lower mass flow rates and cause an increase of the efficiency over the whole operating range. Configuration (d) has a greater impact than configurations (b) and (c) on the surge margin at higher mass flow rates but the maximum flow rate reduces and the efficiency in the area decreases.
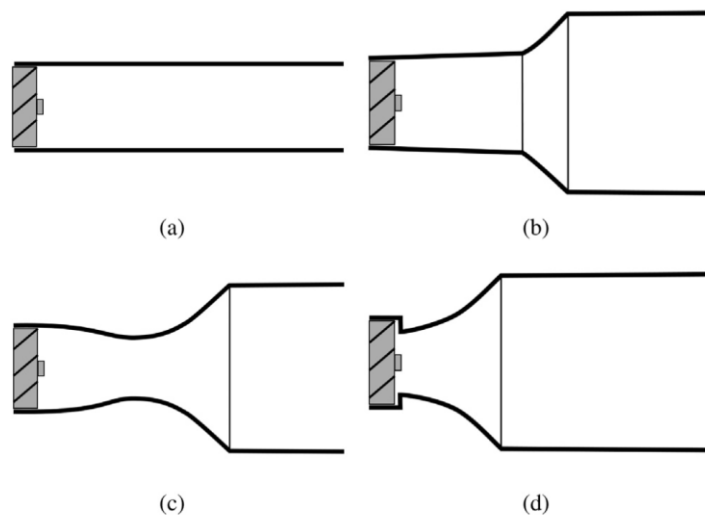
Fig. 1.5 – Four Different Compressor Inlet Configurations Tested by Galindo [5]

Some studies also concentrated on the effect of a pulsating flow on compressor stability [26], [27], [28]. Marelli coupled two different turbochargers to two engine heads (one two-cylinder and one four-cylinder head) and studied the effect of valve opening strategies and of the number of cylinders on the stability limit [29]. The work shows that the 2-cylinder configuration and the early closing of the intake valve extended the compressor stable zone. Shu also investigated the effect of pulsating back pressure in a work concentrated on the evaluation of the compressor performance in unsteady flow conditions [30]. Shu highlighted that pulsating back pressure delays surge occurrence at the three investigated rotational speeds.

Researchers Galindo, Climent, Guardiola and Tiseira also published interesting results on the influence of unsteady flow on the performance of small centrifugal compressors [31]. The work concentrated on correlating the amplitude and frequency of the pulsating flow to the position of the surge line. During the investigation carried out at the test bench of the Universidad Politecnica de Valencia, the compressor stability limit was defined and measured in steady and unsteady flow conditions in an extended range of conditions. The surge limit was identified for five different turbo rotation speed values, with varying frequency and amplitude of the pulsations. The frequency and amplitude values of the oscillations were chosen in the range

5

between 40 and 66.67 Hz to recreate engine flow conditions. The results collected by Galindo have shown that, in the presence of pulsating flow, the stability limit tends to move towards lower mass flow values than in the steady case. The results also show that the shift in the position of the surge line is affected only by the amplitude of the pulsating flow. The frequency of the oscillation does not affect the position of the stability limit.
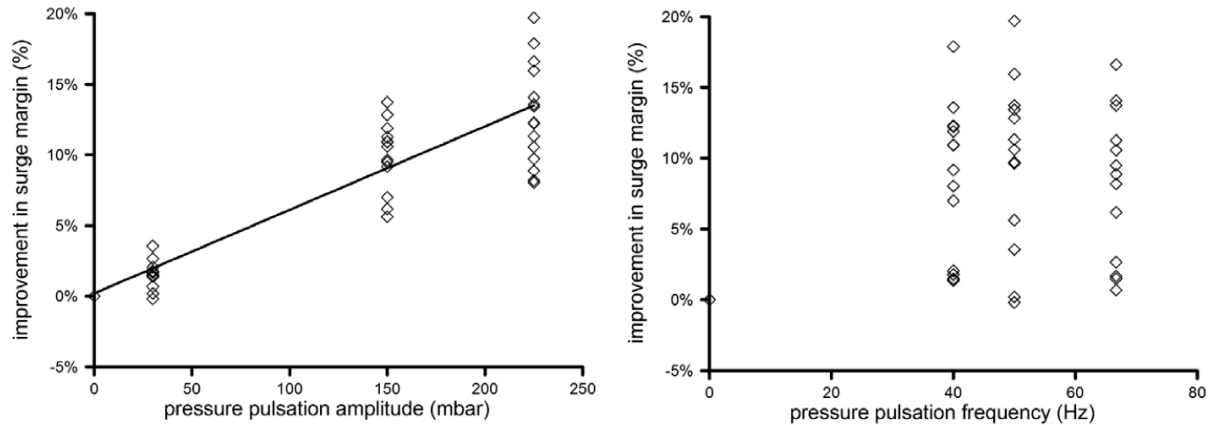
Fig. 1.6 – Effect of Amplitude and Frequency of Oscillations on the Surge Margin [31]

The complexity of the phenomena leading to surge in a centrifugal compressor, such as secondary flows, moved researchers to concentrate on multi-dimensional modeling and experimental activity. Most multi-dimensional high-fidelity compressor models are almost universally used to study the inception and development of stall as opposed to surge [32], [33], [34], [35]. Stall develops in the compressor at low mass flow rate condition and is not caused by the interactions between the compressor and the system, as opposed to surge. For this reason, studies concentrate on the compressor physical phenomena that cause stall and can lead to surge. The study of the stall phenomena using these elaborate models and through rigorous experimental characterization (PIV or high density of internal pressure sensors) have provided an important insight into the dominant multidimensional flow patterns within compressors. Early studies focused on the jet-wake flow profile at the impeller exit definition [36]. Following work by Dean and Senoo formalized the presence of the jet-wake profile and proposed equations to explicitly model the jet-wake regions of the flow [37].

Current research on stall inception often uses the assumption of jet-wake, such as the work by Ljevar that imposes a jet-wake profile at the exit of the impeller to study inception of diffuser stall in a vaneless centrifugal compressor [38]. Ljevar developed a two-dimensional incompressible flow model of the vaneless diffuser core flow. Since the wall boundary layers are not considered, this model applies only to wide vaneless radial diffusers with parallel diffuser walls. The analysis studied the influence of geometry parameters and diffuser inlet flow conditions on the two-dimensional vaneless diffuser flow stability. The inlet flow parameters were the impeller tip speed, the mass-flow rate, and shape and intensity of the jet-wake pattern. The diffuser parameters analyzed were the diffuser radius ratio and the number of impeller blades. The analysis showed two different operating conditions which occur the mean flow angle at the impeller outlet is greater or smaller than a defined value, called the critical flow angle. Stable and stall behavior are shown in Fig. 1.7. Ljevar also noted that the two-dimensional

6

rotating instability is associated with rotating stall in wide vaneless diffusers, implying that this instability might contribute to the vaneless diffuser rotating stall.
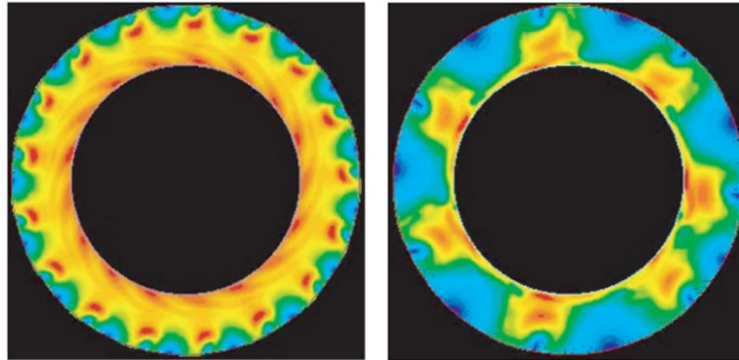
Fig. 1.7 – Stable Operating Condition (Left) and Two-Dimensional Rotating Instability (Right) [38]

An experimental and modeling work by Schleer et al. analyzed the effect of clearance effects on the onset of instability [39]. Schleer analyzed the time-resolved measurements of the static pressures, by installing pressure sensors along the flow to detect clearance vortices and stall precursors. The work also analyzed the sequence of events leading to rotating stall in the diffuser. A stability analysis revealed that inlet tip recirculation is triggered, when the leakage vortex approaches the adjacent blade. This leads to a sudden increase of random pressure fluctuation in the inducer section and a change in the loading distribution. If the flow is throttled further, rotating stall is initiated in the diffuser while the inlet recovers. For increased tip clearance, the onset of rotating stall is shifted to higher mass flows while the onset of tip recirculation is not affected by a change in tip clearance width.

Since surge can cause damages not only to the compressors but also to the components downstream the compressor, surge control has attracted attention in many fields. Current industry utilizes black-box models, which rely on the steady-state compressor characteristics to define the limits of the stability region. The compressor steady-state characteristics are generally limited to a small operating range, when the data is provided by the compressor manufacturers. The data collection for the map calculation is time-consuming and expensive. The compressor maps also do not provide any information on the dynamics of the compressor and on the interaction between the compressor and the surrounding system. Given that surge is a global phenomenon generated by the pressure gradients along the line, the implementation of a control model based entirely on the steady-state characteristic requires high safety margins. This approach not only reduces the compressor and engine operating region, but it also cuts out the most efficient compressor operating points. The necessity to have a control-oriented model that could capture the behavior of the system and the physics inside the compressor pushed researchers to develop simplified models. High-fidelity multi-dimensional models are too computationally intensive to be able to run in a real-world control application. The importance of this type of model though lies in the ability to increase knowledge in surge phenomena that can be applied to a control-oriented model [40], [41].

7

For this reason, Gravdahl and Egeland built further upon the Moore-Greitzer model for a vaneless centrifugal compressor. They used the same lumped parameter model that neglects stall dynamics and a physics-based compressor characteristic to predict the pressure rise dynamics [42]. Their physics-based characteristic derives from the mean-line analysis of the flow in the compressor where conservation laws and thermodynamic principles are applied. In addition, they incorporated simple correlations for enthalpy and heat losses that reduce the pressure rise and compressor efficiency. In addition, Gravdhal introduced the momentum balance equation on the turbocharger shaft, taking into account the speed variations and the turbine power input. Although the Gravdahl-Egeland model is an improvement on the cubic approximation used by Moore and Greitzer, the model still lacks the ability to capture the subtleties of the compressor behavior near surge, where the characteristic curves are nearly flat. The loss models employed by Gravdahl and Egeland are very basic, especially when compared to empirical loss correlations employed by other mean-line analysis models that are formulated to capture specific effects of secondary flows [43], [44], [45], [46]. The absence of the effects of secondary flow impacts the shape of the characteristic near surge, influencing the simulated mechanism of surge inception which is critically important for modelling surge onset.

High-fidelity one-dimensional models are the most physically consistent models available for surge prediction since the wave-action dynamics in the system are modeled with partial differential equations (PDEs) derived from first principles, but these models still employ empirical loss correlations to compensate for secondary flow effects. For example, a vaneless centrifugal compressor was modeled in [47], by employing the one-dimensional Euler equations in each component of the compressor and relating the component states at the boundaries using Riemann invariants (Method of Characteristics) and point losses. Even though the model achieves accurate prediction of the surge behavior, the one-dimensional framework is significantly complex and requires calibration of numerous loss correlations. Furthermore, the implicit relationship of states at the boundaries creates a computationally intensive model that would be nearly impossible to simplify to a controls-oriented model capable of running in real-time on embedded hardware.

Alternatively, Galindo et al. [48] propose a compression circuit model where the compressor is considered as a simple boundary condition (with mass conservation, artificial pressure dynamics based on the steady-state characteristic curve, and energy conservation defined via the efficiency) within a compressor circuit governed by the 1-D Euler equations. The scheme for the wave action model, however, is also computationally intensive, and the compressor model is based on a cubic approximation of the characteristic curve.

In this context, the development of an accurate, predictive model for the conditions that lead the compressor into unstable behavior is a necessary step towards the design of estimation methods and control algorithms for surge prevention, ultimately leading to the ability to operate the compressor in an extended range and improving the transient response of the turbocharger. To achieve this goal, the work presented in this thesis concentrated on two different aspects of the problem: collection and analysis of experimental data and the development of 1-D physics-based compressor system model. This necessity brought together the University of Genoa and the Ohio State University. An internal combustion engine component test bench is located at the University of Genoa, which is specifically designed to test automotive turbochargers. The

8

expertise coming from many years of testing at the University of Genoa provided knowledge on the experimental side of the project. The Center for Automotive Research (CAR) at the Ohio State University provided foundational models and modeling knowledge to develop the compressor system model. The work was organized in three stages: during the first year, a thorough experimental investigation was designed and conducted; during the second year, the experimental data collected was used to develop a compressor model; during the third year, a second experimental investigation was conducted and the results were used to calibrate and validate the model as well as analyzed some parameters that affected the transition into surge.

The first experimental investigation was designed to increase knowledge of the phenomena that lead to surge on a small automotive turbocharger compressor. The aim was to investigate the effect of the compressor outlet circuit on the transition into surge, so the system was designed to be modular in both length and volume. The compressor outlet circuit consisted of a modular pipe leading to a plenum of modular volume. The sizes of both circuit and volume were based on research that identified the range of volume and length typical of applications on internal combustion engine. Temperatures and pressures were measured in different points along the system, while the average mass flow rate was measured in one station on both the compressor and turbine circuits. The tests were conducted on different circuit configurations and at different compressor corrected rotational speeds. For each of these combinations, both stable and transient conditions were measured. The stable measurements were taken in operating conditions extending from choking conditions to the last stable point before surge. Transients were measured from the last stable point to a deep surge condition. Instantaneous pressure signals were collected in all conditions to compare frequency components in stable points closer and farther away from the surge line.

The data analysis provided insight to develop a control-oriented one-dimensional compressor model. The work started with the calculation of the compressor steady-state characteristic in a simplified version: the only compressor losses considered were friction losses in the impeller and the diffuser. The model derives from a mean streamline analysis, where the conservation equation of mass momentum and energy are applied to the inducer, impeller and diffuser components. In a second moment, different loss correlations were implemented in both the compressor and diffuser equations and a sensitivity analysis was conducted to evaluate the effect of the different loss correlation on the shape and positions of the compressor characteristic. Based on the results of the sensitivity analysis, the compressor steady state characteristic was calibrated in the stable region to verify the ability of the model to capture steady-state behavior.

The calculation of the steady-state characteristic was then extended to the unstable region with positive mass flow rate. The jet and wake two zone model in the impeller and diffuser was adopted and the limitations of the model were highlighted. The phenomena that occur when the mass flow rate approaches zero can't be capture with the jet and wake model. For this reason, the model was adapted, and some additional loss correlations were implemented. These loss correlations take into account the effect of a jet and wake flow distribution in the vaneless diffuser.

Once the steady-state characteristic was calibrated, the development proceeded with the implementation of the steady-state characteristic in a dynamic model of the compressor and the pipe system. The equations that govern the dynamics of the compressor were identified and

9

implemented in a one-dimensional distributed-parameter model of the pipe system, volume and throttle. The model represents the experimental set-up built for the tests conducted at the University of Genoa.

Following the development of the model, a new set of tests was designed. Minor modifications were implemented in the experimental lay-out used for the first experimental investigation. This lay-out was modified to allow the calibration and validation of the dynamic model and a better comparison between the modeling and experimental results. Additional measurements were also taken: hot film anemometers were inserted upstream and downstream of the compressor to measure the instantaneous local mass flow rate and identify the filling and emptying phenomenon in the compressor; since the position of the throttle valve, located after the plenum in the compressor outlet circuit is the input to the compressor model, it was also measured in both steady and transient conditions.

The data collected during the second experimental investigation was analyzed to identify behavior that occurs during deep surge cycles and during transients from stable to unstable operation. The same data was also used to calibrate and validate the compressor model, which was then run for many different simulations to identify the loss terms and behavior that occur during stable operating conditions just before the transition into unstable behavior.

Chapter 0 describes the University of Genoa's test bench capabilities and properties in detail. First the test bench fluid system is described, and then the description of the measurement and acquisition system follows. Chapter 3 describes, in detail, the experimental set-up of the first experimental investigation and second experimental investigation. The second part of the chapter describes test procedures for the first and second experimental investigation. Chapter 4 describes the calculations for the steady-state characteristic and the dynamic model equations. Finally, Chapter 5 discusses the results of the first and second experimental investigation and the modeling results of calibration and validation. The results conclude with the simulations performed to identify the loss terms that cause a transition into surge.

2 University of Genoa Testing Facility

The experimental investigations described in this thesis utilized the internal combustion engine components test bench in the Department of Mechanical, Energy, Management and Transportation Engineering (DIME) of the University of Genoa, Italy. This chapter describes the characteristics and capabilities of the test bench, measurement system and acquisition system.

The test bench's open loop configuration allows an independent analysis of the compressor and the turbine in both steady and unsteady conditions. To test the compressor, the power into the system is controlled by regulating the airflow upstream of the turbine, as the turbine acts as a controlled power source into the system. To test the turbine, the compressor acts as a controlled load on the system by regulating the pressures at the compressor inlet and outlet. An electrical heater and three screw compressors control the operating conditions at the turbine inlet. Combined the screw compressors can provide 0.65 kg of air per second to a maximum pressure of 8 bar and temperature of 600 °C. The ability to reach these conditions allows the test bench to replicate engine exhaust gas conditions. The test bench's pulse generators allow the system to reproduce the pressure oscillations seen when opening and closing the intake and exhaust valves in an engine with varying degrees of accuracy. The pulse generators can be placed at either the compressor outlet or the turbine inlet, depending on the test being conducted.

The sensors installed in the test bench measure mass flow rate, static pressure, total temperature, rotational speed and valve position. The measurement system collects the time average of all parameters for measurements during steady state conditions and the instantaneous values during transient or unsteady conditions. The lab operator can control testing parameters and collect data using the control room's pneumatic, electronic, and digital interfaces with the test bench.

2.1 Test Bench Description

The test bench, shown in Fig. 2.1 can be divided in the following systems: the Compression Unit, the Working Fluid Circuit, the Auxiliary Fluid Conditioning System and the Control System. The Compression Unit supplies the required air flow rate and pressure for different sizes of turbochargers. The Working Fluid Circuit provides treated air at set conditions to the compressor and turbine using an air filter, drier, and heater. The air filter and drier pretreat the air to prevent damage to the measuring equipment and turbocharger components. The heater regulates the turbine inlet temperature to avoid ice formation on blades and guarantee test repeatability. The Auxiliary Fluid Conditioning System provides oil and coolant to the turbocharger and motor head, if the motor head is present. The Control System allows the operators to visualize and collect relevant test parameters and command behaviors from the other systems remotely.

11
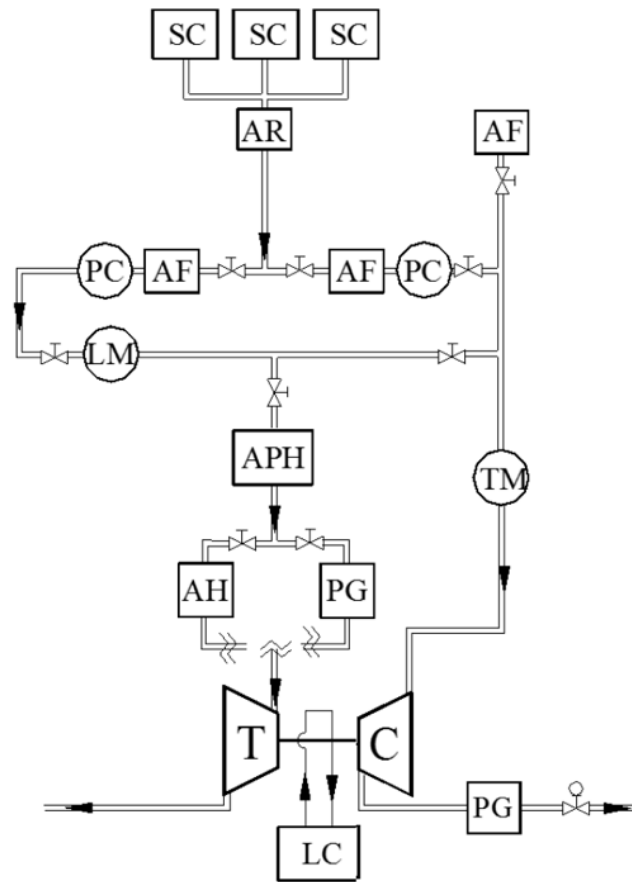
AF	Air Filter	LM	Laminar Flow Meter
AH	Air Heater	PC	Pressure Control
APH	Air Pre-Heater	PG	Pulse Generator
AR	Air Reservoir	SC	Screw Compressor
C	Compressor	T	Turbine
LC	Lubricating Circuit	TM	Thermal Mass Flow Meter

Fig. 2.1 – Schematic Representation of the University of Genoa Test Bench [49]

2.1.1   Compression Unit

Located outside the test cell, the compression unit provides the pressure and air flow into the turbocharger. The three screw compressors (two KAESER model CSD 122 and one DEMAG) are located outside the testing room and operate in parallel, producing a total mass flow rate of 0.65 kg/s. The two KAESER compressors can produce the required mass flow rate for most test conditions by working in parallel: one compressor works continuously, while the second one is active during demand peaks. The compressors switch roles after several hours to guarantee similar utilization in both machines. The DEMAG compressor acts as a redundancy to support the two KAESER compressors.

The KASER compressors operate using a 380 V and 50 Hz frequency three phase supply, requiring a maximum power of 75kW each. Each compressor can provide a maximum air mass flow rate of 0.22 kg/s, considering an ambient temperature of 30 °C and a maximum pressure of 8 bar gauge [50]. Ambient air flows through the filter (1) and expansion valve (2) to reach the screw compressors (3). The expansion valve regulates the pressures at each machine's inlet and avoids high mass flow rate oscillations during fast flow rate transients. Because the working fluid is a mixture of lubricating oil and air, it is necessary to insert an air oil separator (5) at the compressor outlets. After the separation of the oil and air mixture, the cooler (6) chills the fluid to a temperature of 5 to 10 °C higher than ambient. The various components that make up a KAESER screw compressor are shown in Appendix A, Test Bench Details.

2.1.2 Working Fluid Circuit

The air feeding line begins downstream of the compression unit and provides air to both the compressor and turbine in an open circuit configuration. The circuit can be divided in the following five sublines: the common feeding line, the turbine feeding line, the compressor feeding line, the turbine outlet line and the compressor outlet line. The circuit is shown in Fig. 2.2 and Fig. 2.3 on page 13 and 14; Tab. A.1, located in Appendix A, Test Bench Details, provides the legend for these figures.
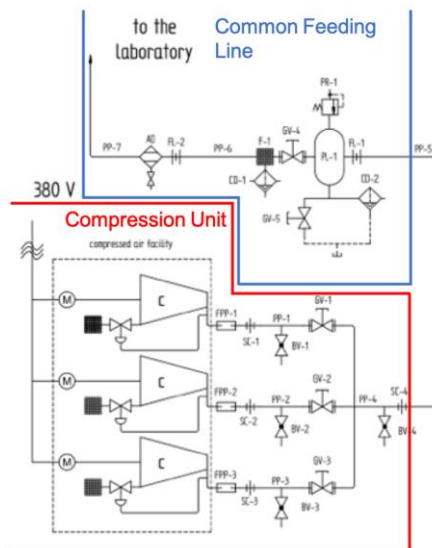
Fig. 2.2 – Working Fluid Circuit External to the Lab
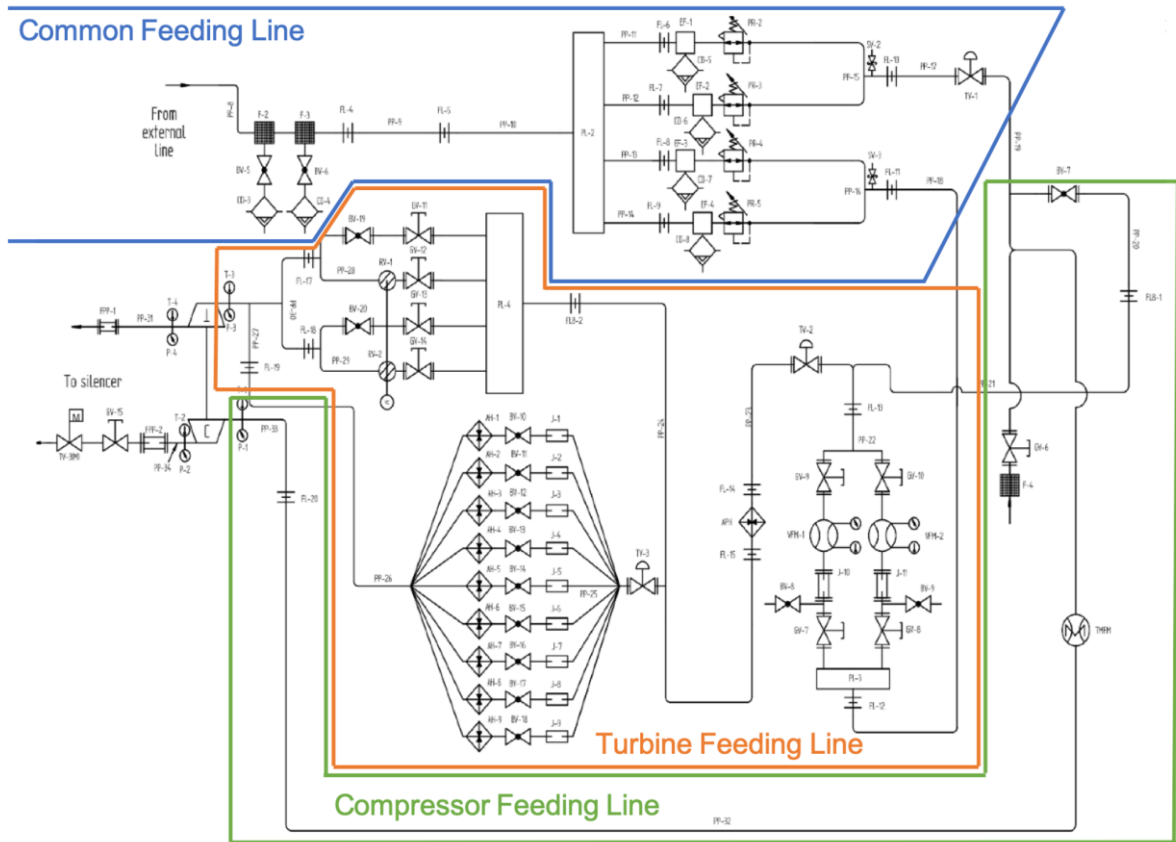
Fig. 2.3 – Working Fluid Circuit Internal to the Lab

2.1.2.1 Common Feeding Line

The air provided by the compression unit is stored in an air reservoir, indicated by PL-1 in Fig. 2.4. The air reservoir has a capacity of 4 m^3 and a security valve (PR-1 in Fig. 2.4) which activates if the reservoir pressure exceeds 8 bar. The purpose of this component is to reduce air oscillations generated by transient or unsteady turbocharger operation and compensate for the different mass flow rates between the compression unit and turbocharger. At the reservoir outlet, the air crosses a purifying and treatment system. The first component is a filter (F-1 in Fig. 2.4) and the second is an air dryer (AD in Fig. 2.4). The dryer unit contains one air to air and one air to glycol mixture heat exchanger, which remove condensation to avoid damage in critical downstream equipment.

14
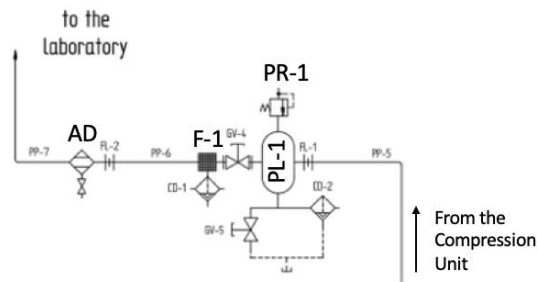
Fig. 2.4 – External Common Feeding Line, Segment from Fig. 2.2

The air then enters the lab and two Zander filters complete the air treatment, indicated as F-2 and F-3 in Fig. 2.5. The Zander filters have a cut-off diameter of 1 μm and of 0.01 μm to allow a maximum oil concentration of 0.001 mg/m^3 [51]. A distributor (PL-2 in Fig. 2.5) regulates the amount of treated air provided to the two parallel lines that independently feed the compressor and turbine. Each feeding line contains two pneumatically powered pressure reducers arranged in parallel (PR-2, PR-3, PR-4 and PR-5 in Fig. 2.5). Two relief valves activate in case of a malfunction of the pressure reducers to avoid damage to the turbocharger or measurement equipment. An additional safety device interrupts air flow to the turbocharger if the lubricating system has failed.
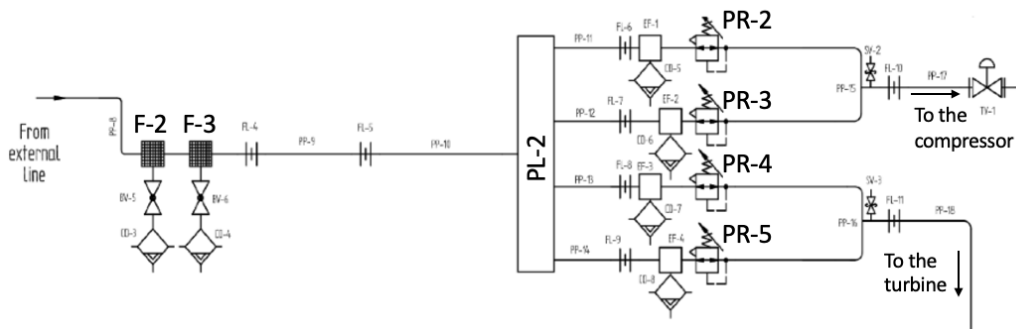
Fig. 2.5 – Internal Common Feeding Line, Segment from Fig. 2.3

2.1.2.2 Turbine Feeding Line

Downstream of the common feeding line, the turbine feeding line includes a pressure control station, another air reservoir (PL-3 in Fig. 2.6 on page 16) and two parallel air flow rate measuring systems (VFM-1 and VFM-2 in Fig. 2.6). The air flow rate measuring systems are laminar flow meters which measure a maximum air flow rate of 100 l/s and 200 l/s and can be used in three different configurations: for low mass flow rates the 100 l/s sensor is used, for high mass flow rate the 200 l/s sensor is used, for mass flow rates that exceed 200 l/s both measuring systems are used in parallel [52]. To select a configuration, the stop valves (GV-7, GV-8, GV-9 and GV-10 in Fig. 2.6) are either opened or closed.
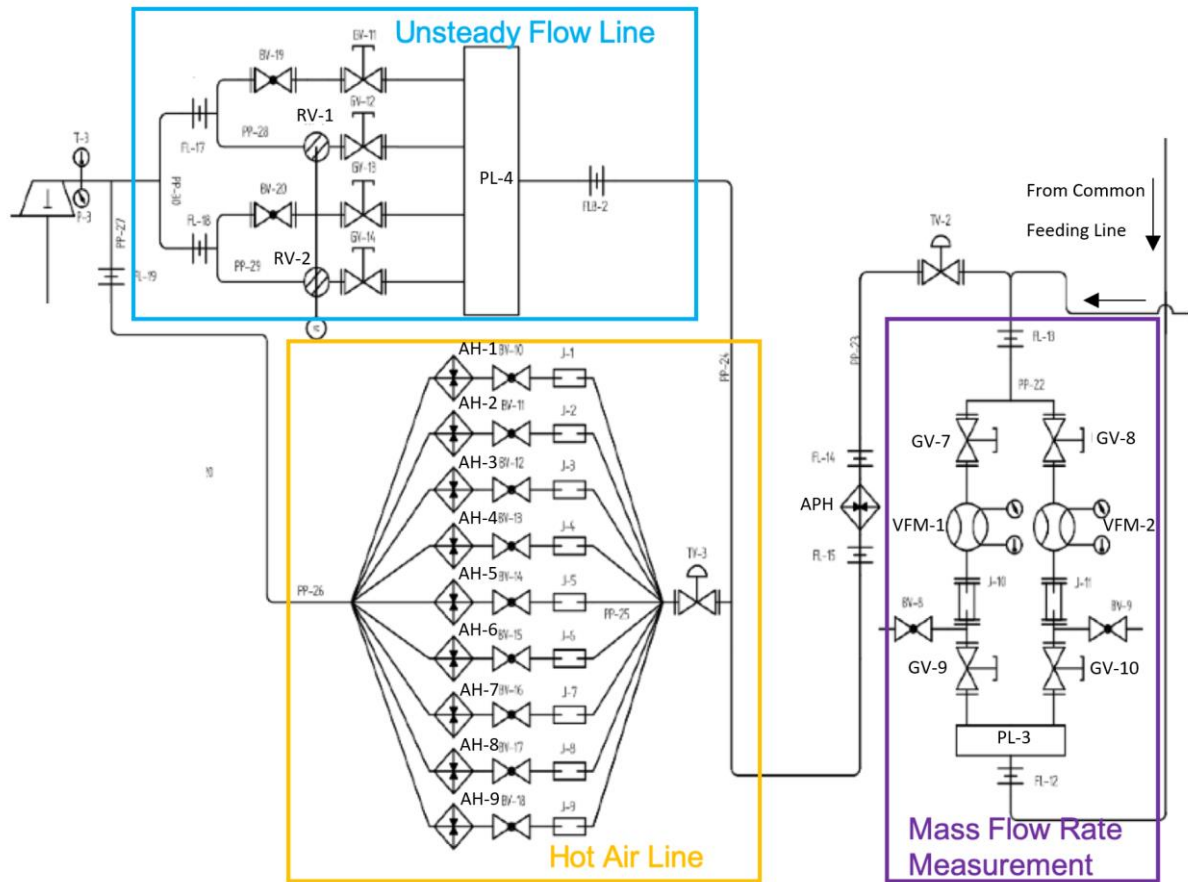
Fig. 2.6 – Turbine Feeding Line, Segment from Fig. 2.3

Immediately downstream of the Mass Flow Rate Measurement segment, the turbine feeding line contains an electric air preheater (APH in Fig. 2.6). This device is used to avoid ice formation in the turbine outlet pipe if a high expansion ratio is required. The maximum heating power is 54 kW and can preheat the air to 110 °C at the maximum air flow rate. The temperature can reach higher values at lower air flow rates but is limited to 120 °C for lab safety. Further downstream of the air preheater there are two parallel branches allowing two types of testing: the first branch contains a pulse generator system and is used for unsteady flow tests (Unsteady Flow Line in Fig. 2.6), the second branch contains an electric heater used for high turbine inlet temperature tests (Hot Air Line in Fig. 2.6). When performing unsteady flow tests the air preheater is used to increase the turbine inlet temperature.

A vessel (PL-4 in Fig. 2.6) with a capacity of 0.06 m^3 is the first component in the unsteady flow line. The vessel feeds four lines: two with the pulse generator systems (RV-1 and RV-2 in Fig. 2.6) and two that are simple pipes. The lines with the pulse generator systems determine the frequency of the oscillations in the flow while the other two lines regulate the steady component of the flow which will affect the oscillation amplitude once the two flows mix. For most tests only one pair of pulse generator and steady line are needed but having two of these sets of lines provides the capability to test double entry machines. The pulse generator system

16

consists of a rotary shutter valve, shown in Fig. 2.7. The valve has two parts: a hollow cylindrical stator and a rotor with a diametrical slot. An electric motor controls the pulse frequency.

Fig. 2.7 – Rotating Valve Used in the Pulse Generator System

The hot air line is used when performing high temperature steady flow tests. The heater increases the thermal power to 324 kW and is composed of nine Sylvania SureHeat MAX F074735 heating elements (AH-1 to AH-9 in Fig. 2.6 and shown in Fig. 2.8) [53].
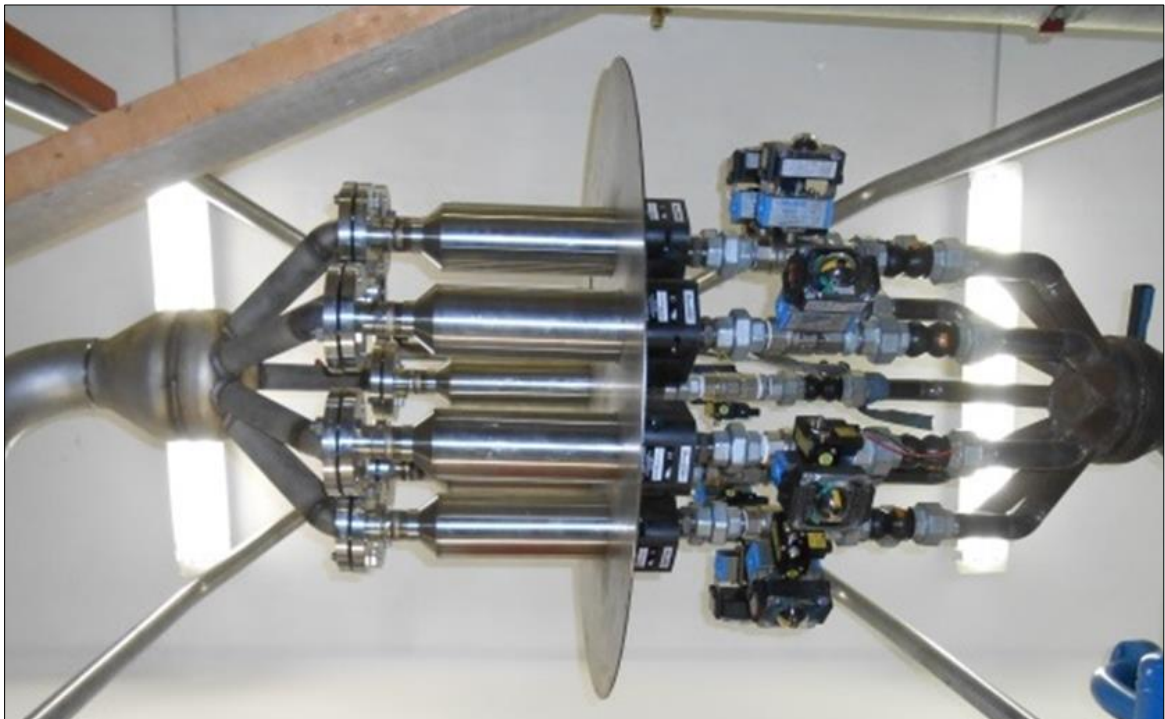
Fig. 2.8 – Electrical Heaters Used in the Hot Air Line

Each heating element has an electro-pneumatic valve that allows a specific number of elements to be used, BV-10 to BV-18 in Fig. 2.6 and shown in detail in Appendix A, Test Bench Details. The number of heating elements used depends on the mass flow rate required by the turbine: if too many heating elements are used, the heat produced will not be absorbed by the air and may damage the heaters; if too few heating elements are used, the desired temperature may not be reached.

17

2.1.2.3 Compressor Feeding Line

As shown in Fig. 2.9 on page 18, two separate lines can be used to feed air to the compressor: the filter compressor feeding line sucks air from the test lab through a filter (F-6 in Fig. 2.9), while the controlled pressure feeding line is connected to the common feeding line and provides pressurized air to the compressor. Valves TV-1 and GV-6 shown in Fig. 2.9 allow the operator to select the line used to feed the compressor. A ventilator is activated when the compressor is not fed through the common feeding line to compensate for the air the compressor is removing from the room. When the compressor is connected to the common feeding line, the mass flow rates to the compressor and to the turbine can be regulated with valves TV-1 and BV-7 shown in Fig. 2.9. Downstream of the valves GV-6 and TV-1, the two lines merge and pass through a mass flow rate sensor (THMF in Fig. 2.9) before entering the compressor.
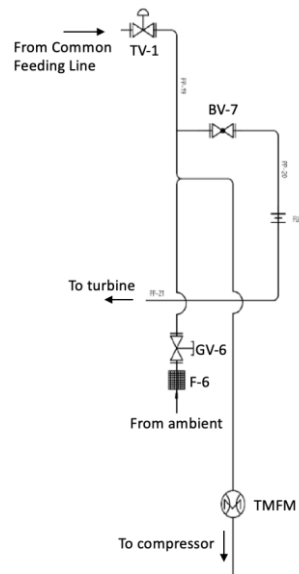
Fig. 2.9 – Compressor Feeding Line, Segment from Fig. 2.3

2.1.2.4 Turbine Outlet Line

The exhaust air from the turbine is discharged outside the lab. The air exits the lab and enters a silencer to avoid excessive noise during unsteady flow investigations, as shown in Fig. 2.10.
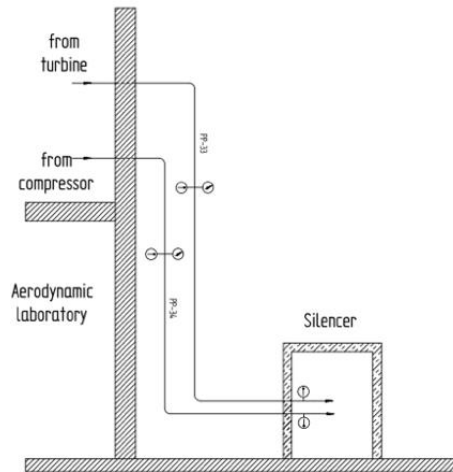
Fig. 2.10 – Turbine and Compressor External Outlet Line

2.1.2.5 Compressor Outlet Line

The first part of the pipe at the compressor outlet contains the measurement equipment while the second contains a motorized throttle valve; this consists of a UNITECH TF series DN 65 butterfly valve motorized by a VALPES ER35.X0B.G00 model actuator [54], [55]. The butterfly valve, shown in Fig. 2.11, regulates the compressor operating point and the power absorbed by changing the circuit external characteristic. After crossing the butterfly valve, the air is sent to the silencer discussed in Section 2.1.2.4, Turbine Outlet Line.
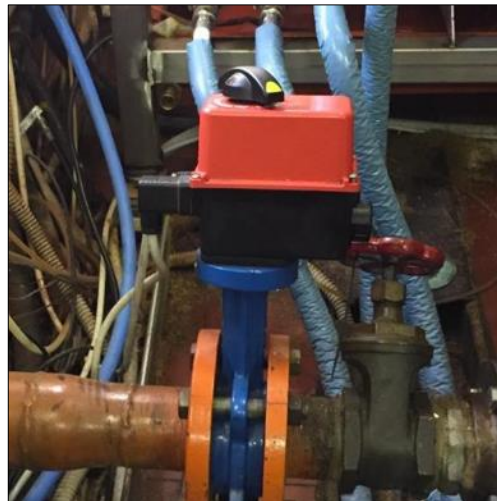
Fig. 2.11 – Motorized Throttle Valve

2.1.3 Auxiliary Fluid Conditioning System

The Auxiliary Fluid Conditioning system is responsible for the lubrication and cooling of the turbocharger and cylinder head. The system consists of three lines: a lubrication line cycling oil, a coolant line cycling a water-glycol mixture, and a common water line used for cooling of the

19

other two lines. The system is shown in Fig. 2.12 on page 20. The lubrication line stores oil in the reservoir, S1, and uses a 5kW resistance and the plate heat exchanger, SC1, to control the oil temperature. Oil is pumped from the reservoir to the heat exchanger, PR1, and from the reservoir to the turbocharger and cylinder head, P1. The lubrication line uses a gravity fed return where used oil is collected in a reservoir at the lowest point of the system, this oil is then pumped back into the main reservoir, S2 and P2. The coolant line is designed similarly to the lubrication line, a water-glycol mixture is stored in a reservoir, S3, and the coolant temperature is controlled by a resistance in the heat exchanger, SC3. Pumps P3 and PR3 circulate the coolant through the turbocharger and heat exchanger. The common water line stores chilled water in a reservoir, S4, feed by the public water supply. If either the oil or coolant is being cooled the water is fed into one, or both, of the plate heat exchangers.
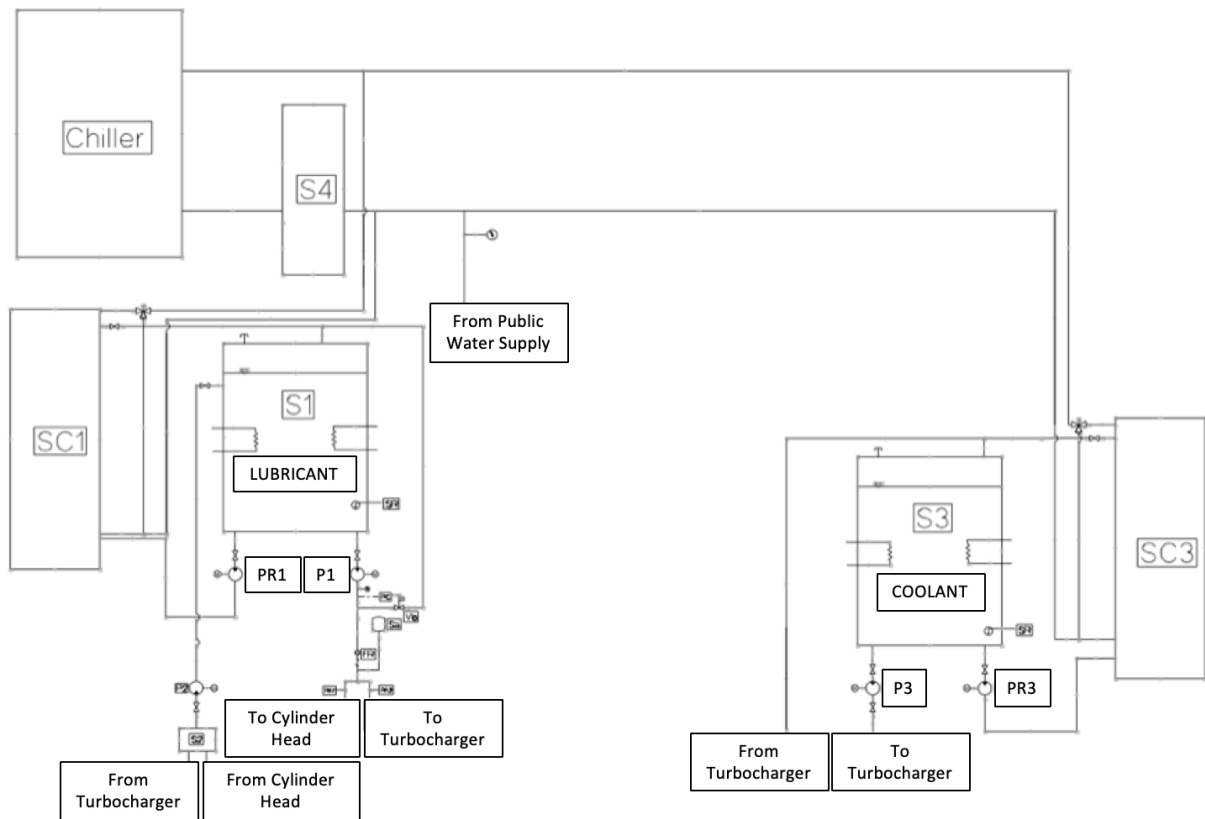
Fig. 2.12 – Auxiliary Fluid Conditioning System

2.1.4 Control System

The control room provides the test operator with a safe work station, separated from the temperatures, pressures, and failure risks of the test cell. With a large window into the test cell, the control room's console provides the test operator with the pneumatic and electrical command signals for the system, several initial feedback interfaces, and circuit calibration equipment. The control console's command interface includes: manual valve controls for the compressor and turbine inlet pressures, a closed-loop temperature control system for the Auxiliary Fluid System, open-loop system to power the compressor outlet butterfly valve, a

touchscreen console for closed-loop control of the electric air heaters, the test cell ventilation power button and fan speed control, the air dryer power and trigger buttons, and the compression unit power activation switches. The control console's feedback interface includes: pressure gauges from the turbine and compressor inlets, the compressor outlet butterfly valve position, signals from the LabVIEW digital data acquisition system, feedback from the display for the electric air heaters, current temperatures in the Auxiliary Fluid System, and oil pressures. These interfaces are labeled in Fig. 2.13. The LabVIEW digital data acquisition system uses one computer for high sample rate measurements and another system for time-averaged measurements; Section A.2, Measuring Equipment Details discusses the two LabVIEW interfaces and their digital data acquisition in detail. Six manometers are located behind the control console and are used to calibrate the circuit's pressure transducers discussed in Section 2.2.3, Pressure Measurements.
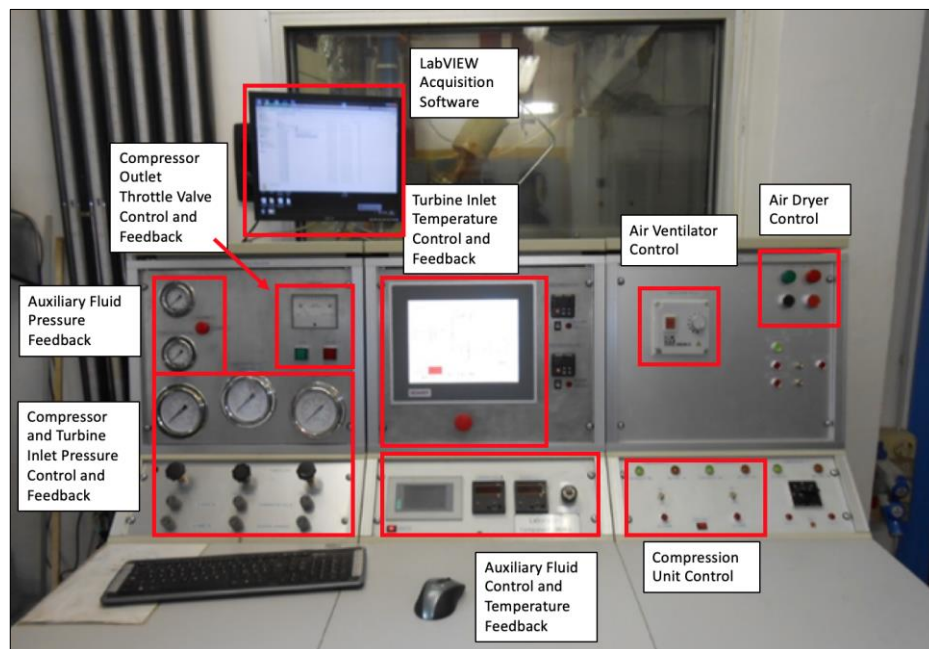
Fig. 2.13 – Control Console

2.2 Measurement Equipment

Sensors were placed in the test cell to measure the ambient conditions and in specific position along the turbine, compressor and auxiliary fluid circuits. This section describes the location the measuring stations and the instrumentation used for different types of measurements: temperature, pressure, frequency, flow rate, vibration and acoustic measurements.

2.2.1 Measuring Stations

The DIME Internal Combustion Engine component test bench utilizes six primary measurement station to monitor the test bench's gas dynamics. Stations 1, 2, and 6 are located along the compressor circuit while Stations 3, 4, and 5 are located along the turbine circuit, shown in Fig. 2.14 on page 23. Stations T, C and PG instrument the turbine casing, compressor casing and the pulse generator. Station Ambient is present in the middle of the test cell.

21

- Station 1 is at the compressor intake,
- Station 2 is at the compressor discharge,
- Station 3 is at the turbine intake,
- Station 4 is at the turbine discharge,
- Station 5 is at the turbine flow rate meter,
- Station 6 is at the compressor flow rate meter,
- Station T is on the turbine casing,
- Station C is on the compressor casing,
- Station LC is along the lubricant fluid circuit,
- Station PG is at the pulse generator,
- Station Ambient measures ambient conditions in the test cell.
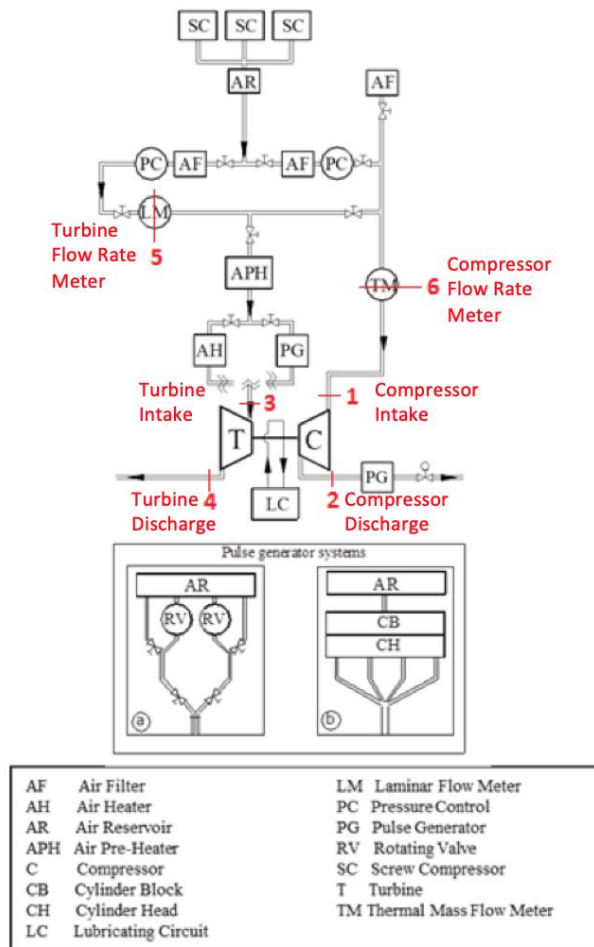
Fig. 2.14 – Location of the Six Measuring Stations in the Test Bench, Adapted from [56]

Each measurement station has a set of ports allowing specific measurement equipment to be inserted into the circuit. The type of measurement equipment used at each measurement station is dependent on its location in the working fluid circuit. The specific capabilities of each measuring station are given in Tab. 2.1.

Port Capability	Station 1	Station 2	Station 3	Station 4	Station 5	Station 6	Station T	Station C	Station LC	Station PG	Station Ambient
Three Resistance Thermometers - Time and Space-Averaged Total Temperature	x	x									
One Resistance Thermometer - Time-Averaged Total Temperature	o[1]	o[1]							x[2]		x
Three Thermocouples - Time and Space-Averaged Total Temperature			x	x							
One Pressure Transducer on Pressure Ring - Time and Space-Averaged Static Pressure	x	x	x	x							
Instantaneous Pressure Measurement - Local Instantaneous Static Pressure	o	o	o	o							
Two Laminar Flow Meters - Turbine Average Mass Flow Rate					x						
Thermal Mass Flow Meter - Compressor Average Mass Flow Rate						x					
One Hot-Wire Anemometer - Local Instantaneous Mass Flow Rate	o	o	o	o							
Lobe Displacement Meter - Average Lubricant Mass Flow Rate									x		
Eddy Current Pick-Up Sensor - Average and Instantaneous Rotational Speed								x			
Inductive Pick-Up - Rotational Frequency										o	
Accelerometer - Vibration	o	o	o	o			o	o	o		
Microphone - Acoustic Measurement							o	o	o		o
(x: essential, o: optional)											
[1]There is the option to install one sensor when the pipe has a small diameter. [2]Both the inlet and outlet of the bearing system have resistance thermometers.											

Tab. 2.1 – Description of Measurements and Sensors in Each Measuring Station

2.2.2 Temperature Measurements

The DIME test bench uses both resistance thermometers and high-temperature thermocouples to monitor the thermal state in several key locations of the working fluid circuit. The resistance thermometers are made of platinum and are type Pt100, with a precision of 0.15 °C ± 0.2 % of the value read on the instrument [57]. The thermometer functions based on the principle that a

24

variation in temperature generates a variation of the conductive material's resistivity. These sensors are inserted into the circuit perpendicular to the air flow and deep in the pipe to guarantee that the measurement is not influenced by the pipe temperature.

The turbine feeding line can have significantly higher temperatures than the compressor feeding line and requires high-temperature, k-type, thermocouples. The thermocouples are made of Chromel and Alumel and have a precision of ± 1.5 °C [58]. These thermocouples function based on the Seebeck effect: two conductive resistances made of different materials are connected at both ends and a potential difference is generated proportional to the temperature difference between the joined ends. An example of the resistance thermometer and the thermocouple are shown in Appendix A, Measuring Equipment Details.

2.2.3 Pressure Measurements

Two different type of pressure sensors are described in this section: the first are regular pressure sensors, used for the pressure measurements along turbine and compressor circuits; the second is a differential pressure sensor, used to measure the pressure drop in the laminar flow meters described in section 2.2.5, Flow Rate Measurements.

2.2.3.1 Average and Instantaneous Pressure Sensors

Twenty-three different pressure sensors are available for tests in the lab. This large assortment of sensors allows for a broad spectrum of testing and each sensor can be utilized at a different measurement station to uniquely tailor the data acquisition strategy to the tests being conducted. The characteristics for each sensor are listed in Tab. 2.2. Sensors 7.01 to 7.05 are Gems Sensors 2600 series strain-gage transducers. Each requires an amplification circuit and has a precision of 0.15% of the full scale [59]. Pressure transducer 7.06 to 7.13 are Sensing & Inspection Technologies pre-amplified piezo-resistive sensors with output voltage proportional to the pressure and a precision of 0.1% of the full scale [60]. Sensors 7.01 to 7.13 have a low frequency response and are used for average value pressure measurements during steady flow tests.

Code	Manufacturer	Range	Temperature Range	Accuracy
7.01 to 7.03	Gems Sensors	0÷2.5 bar VG	-54÷120 °C	±0.15% f.s.
7.04 and 7.05	Gems Sensors	0÷4 bar VG	-54÷123 °C	±0.15% f.s.
7.06 and 7.07	Sensing & Inspection Technologies	0÷2.5 bar VG	-20÷80 °C	±0.1% f.s.
7.08 and 7.09	Sensing & Inspection Technologies	0÷4 bar VG	-20÷80 °C	±0.1% f.s.
7.10 to 7.13	Sensing & Inspection Technologies	0÷0.35 bar VG	-20÷80 °C	±0.1% f.s.
7.14 to 7.20	Kulite Semiconductor	0÷4.48 bar G	25÷232 °C	±0.1% f.s.
7.21	Kulite Semiconductor	0÷2 bar A	20÷120 °C	±0.1% f.s.
7.22 and 7.23	Kulite Semiconductor	0÷1.7 bar A	-40÷177 °C	±0.1% f.s.

Tab. 2.2 – Pressure Transducers [59], [60], [61], [62], [63]

The Kulite semiconductor pressure transducers, 7.14 to 7.23, are piezo-resistive pressure transducers characterized by a wide measuring frequency range. These transducers measure pressure with a high frequency response and are used to measure time-variant signals. The transducers are often used in pulsating flow tests and surge detection. It is important to underline that these pressure sensors are accurate up to an operating temperature of 232 °C; meaning that they can operate reliably in the high temperatures, seen at the compressor outlet. At the turbine inlet, temperatures during high temperature tests can be higher than 232 °C so Kulite semiconductors pressure transducers cannot be used. They are all characterized by a precision of ±0.1 % of the full scale [61], [62], [63]. Additional information on sensors 7.14 to 7.20 can be found in Appendix A, Measuring Equipment Details.

2.2.3.2 ABB ASK-800 Differential Pressure Transducer

The ABB ASK-800 differential pressure transducer measures the pressure drop in the laminar flow meters used in Measuring Station 5. This sensor is capable of pressure differences up to 60 mbar, which is more than necessary to measure pressure losses in the laminar flow meter [64]. The output is a current signal proportional to the pressure drop.

2.2.3.3 Pressure Sensor Calibration

The pressure sensors were calibrated by correlating the sensor's output voltage and the pressure at the calibration station with one of the six manometers located in the control room. The relation between pressure and voltage was programmed into a calibration program that validated the relation by comparing it against calibration results obtained in previous tests.

2.2.4 Frequency Measurements

The turbocharger and pulse generator are two components of the test bench whose rotational speed is critical to the behavior of the system. A PICOTURN BM-V6 inductive tachometer is used to measure the speed of the compressor impeller and an inductive encoder is used to measure the frequency of the pulse generator's valve.

2.2.4.1 PICOTURN BM-V6 Turbocharger Tachometer

A PICOTURN BM-V6 inductive tachometer measures the turbocharger's rotational frequency. This sensor can measure very high speeds and provide the instantaneous value with high precision (0.5% of the full scale [65]). PICOTURN's BM-V6 is composed of a dedicated signal conditioner and an eddy current pickup sensor, shown in Fig. 2.15. The eddy current pickup sensor faces the compressor impeller and records inductance changes caused by blades passing. The signal conditioner converts the pickup sensor's pulse signal into the turbocharger rotational speed using the number of compressor blades.

Fig. 2.15 – PICOTURN BM-V6 system [65]

2.2.4.2 Pulse Generator Valve Inductive Encoders

Inductive pickups are used to measure the rotational frequency of the rotating valves' of the pulse generator. These pickups are composed of coils wrapped around a permanent magnet that face a ferromagnetic phonic wheel. The phonic wheel is connected to the valve shaft and the teeth movement varies the electromagnetic field which is measured by the inductive pickup and correlated to the valve's rotational frequency.

2.2.5 Flow Rate Measurements

Two laminar flow meters, one thermal mass flow meter and two hot film anemometers measure air mass flow rate in different measurement stations along the circuit. A lobe displacement meter measures the lubricant mass flow rate.

2.2.5.1 Cussons Technology Laminar Flow Meters

The two laminar flow meters, Cussons Technology P7205 and P7209, measure the air mass flow rate in the turbine intake circuit. The P7205 sensor can measure values up to 100 l/s, while the P7209 can measure values up to 200 l/s [52]. They can be used simultaneously if the flow rate requested by the turbine is higher than 200 l/s.

Fig. 2.16 – Laminar Flow Meters, P7205 (left) and P7209 (right)

An internal matrix straightens the flow to guarantee laminar flow conditions. A differential pressure sensor estimates the flow rate from the pressure loss, see Fig. 2.17 for a cross section of the device. When the flow is laminar, the pressure drop across the instrument is proportional

27

to the average volumetric flow rate. Equation (2.1) provides the relation between the flow's speed and the volumetric flow rate:

$$Q = C \cdot \Delta p \cdot FT \tag{2.1}$$

where:

- Q is the volumetric flow rate,
- C is the slope of calibration line,
- Δp is the pressure drop,
- FT is the corrective coefficient that take into account viscosity variations with temperature.

Temperature and pressure measurements downstream the sensor allow the calculation of the density, which is multiplied to the volumetric flow rate to obtain the mass flow rate.
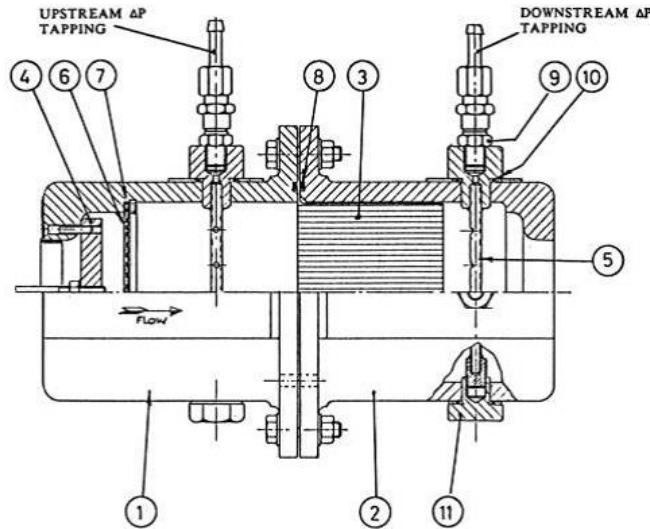
Fig. 2.17 – Laminar Flow Meter

2.2.5.2 ABB Thermal Mass Flow Meter

An ABB Sensyflow FTM500-IG thermal mass flow meter, shown in Fig. 2.18, measures the average compressor mass flow rate. This sensor is denoted as TMFM in the compressor feeding line, see Fig. 2.9 on page 18. This sensor is less invasive than the laminar flow meter because it does not occupy the whole area of the pipe; the only intrusive part is the sensor and its support. Since the accuracy of the measurement increases when the flow is fully developed, a flow rectifier (Zanker plate) was placed upstream the sensor. The sensor probe is made of platinum elements which allows a higher reliability and mechanical resistance than a hot film anemometer but reduces the sensor frequency response. For this reason, the thermal mass flow meter is only used for steady flow measurements. This device can measure an air flow rate up to 3200 kg/hr and is characterized by an error of ±0.9 % of the measured value plus ±0.5 % of the full scale

28

[66]. An image of the ABB Sensyflow sensor is provided in Appendix A, Measuring Equipment Details.

Fig. 2.18 – ABB Sensyflow FTM500-IG Installed on Testing Line

2.2.5.3 Flomec Lobe Displacement Meter

The Flomec OM006A lobe displacement meter used in the Lubrication Circuit uses the Hall Effect to measure the lubricant flow rate. The full scale of the sensor is 100 l/hr and its accuracy is ±1 % of the full scale [67].

2.2.5.4 Dantec Dynamics Hot Film Anemometers

Several Dantec Dynamics hot film anemometers are used to measure instantaneous air flow rates. The sensor Dantec Dynamics model 55R04 is made of nickel which provides a valuable compromise on diameter while providing good mechanical resistance and maintaining a high frequency response [68]. This device requires a Dantec Dynamics Mini CTA 54T30 conditioner, shown with the anemometer in Fig. 2.19, to maintain the anemometer's film at a constant temperature [69]. The anemometer's film is an electric resistance and dissipates heat according to the Joule Effect while exchanging heat with the fluid. Because the current required to maintain a constant film temperature is proportional to the thermal power exchanged with the fluid and this exchange is proportional to the flow's speed, the conditioner can estimate the volumetric flow rate at the measuring station.
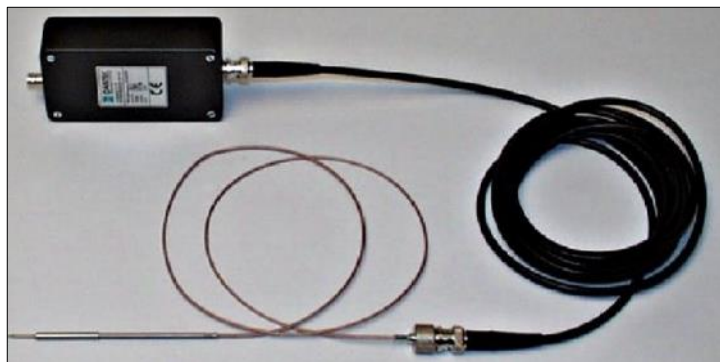
Fig. 2.19 – Hot Film Anemometer and Conditioner

29

The anemometers were positioned in the center of the pipe with the sensor probe perpendicular to the oncoming flow. The sensors were kept in the same position for both tests and calibration, but the pipe containing the measuring station was connected to the hot air turbine line during calibration. This set-up allowed calibration at a broader range of temperatures. The temperature ranges were determined for each anemometer based on the results of the first experimental investigation: the calibration temperature values for the anemometer at the compressor inlet were set to 20, 25, 30, 35 and 40 °C, while the temperature values for the compressor outlet were set to 20, 50, 75 and 100 °C. The measured data was fit with a bivariate polynomial which was 3rd order with respect to voltage and 2nd order with respect to temperature this function is shown in Equation (2.2).

$$Mc(T,V) = p_{00} + p_{10} \cdot T + p_{01} \cdot V + p_{20} \cdot T^2 + p_{11} \cdot T \cdot V + p_{02} \cdot V^2 + p_{21} \cdot T^2 \cdot V + p_{12} \cdot T \cdot V^2 + p_{03} \cdot V^3 \tag{2.2}$$

The calibrated coefficients are listed in Tab. 2.3 and the calibrated maps are shown in Fig. 2.20 and Fig. 2.21. The R-square value associated to the fittings are 0.9997 for the anemometer at the compressor inlet and 0.9986 for the anemometer at the compressor outlet.

Coefficients	Compressor Inlet	Compressor Outlet
p00	- 1.259	- 0.228
p10	+ 0.0216	+ 0.002463
p01	+ 1.53	+ 0.215
p20	- 0.00006834	- 0.000009549
p11	- 0.01884	- 0.001724
p02	- 0.639	- 0.06704
p21	+ 0.00003578	+ 0.00000467
p12	+ 0.004192	+ 0.0002721
p03	+ 0.09487	+ 0.007608

Tab. 2.3 – Calibration Coefficients
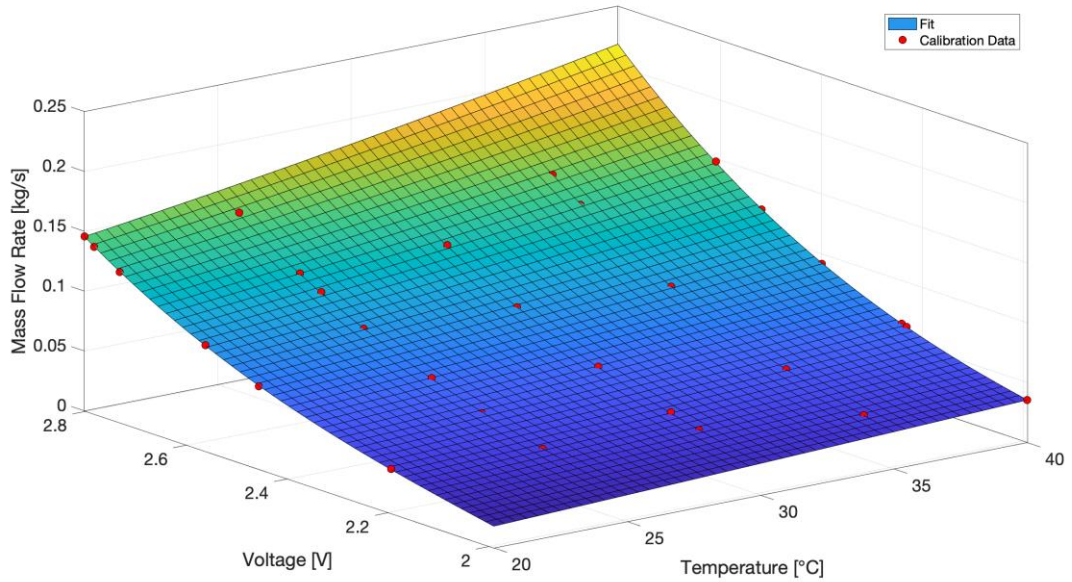
Fig. 2.20 – Compressor Inlet Anemometer Calibration
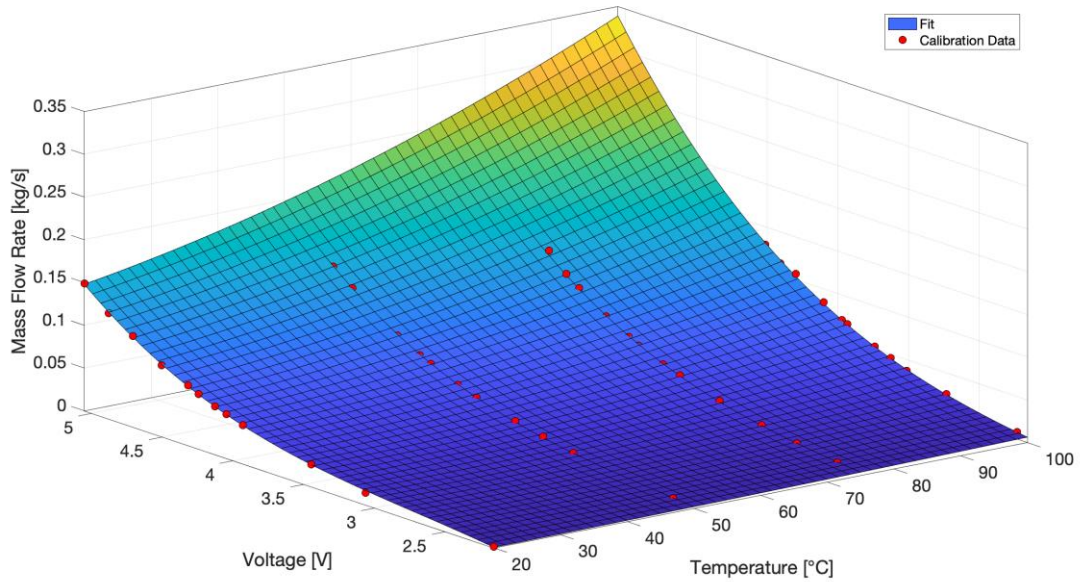
Fig. 2.21 – Compressor Outlet Anemometer Calibration

2.2.6   Vibration Measurements

The experimental investigation used two types of accelerometers as each captured a different frequency range. The accelerometers were installed on pipes or turbocharger casing with a two-

component adhesive which guaranteed adhesion at both high and low temperatures. The PCB model 352C33 accelerometer is a larger accelerometer which measures low frequency vibrations (2.5 to 10000 Hz) and was installed on the pipes at the compressor inlet and outlet [70]. The other accelerometer, a Brüel & Kjær type 4393, can capture high frequency vibrations (higher than 10 kHz) and were installed on the compressor casing to measure vibration caused by the machine's rotation [71]. The machine's rotation generates vibrations characterized by a frequency equal to the rotating frequency times the number of blades (blade passing frequency). For the tested compressor, the blade passing frequency resulted higher than 10 kHz for the higher speed values. The characteristics of both accelerometers are shown in Tab. 2.4. Images of the accelerometers are provided in Appendix A, Measuring Equipment Details.

	PCB Model 352C33	**Brüel & Kjær type 4393**
Sensitivity	10.2 ($\pm$10%) mV/(m/s²)	0.316 ($\pm$2%) pC/(m/s^2)
Frequency Range	2.5 to 10000 ($\pm$5%) Hz	0.1 to 27000 ($\pm$10%) Hz
Resonance Frequency	>50 kHz	55 kHz
Weight	5.8 g	2.4 g
Reference	[70]	[71]

Tab. 2.4 – Accelerometer Characteristics

2.2.7 Acoustic Measurements

Two different microphones were used during the experimental activity; a G.R.A.S. 40AE 1/2" pre-polarized free-field was located near the compressor casing, and a pre-amplified G.R.A.S. 26CA 1/2" CCP standard was located at the pipe inlet by the filter inlet section. The microphone was moved at the inlet of the inlet pipe, when the open inlet configuration was adopted. The microphones' characteristics are given in Tab. 2.5. Images of the microphones are provided in section A.2, Measuring Equipment Details.

	G.R.A.S. 40AE 1/2"	**G.R.A.S. 26CA 1/2" CCP**
Frequency Range	3.15 to 20000	2.5 to 200000 Hz
Noise	-	1.8 μV
Sensitivity	50 mV/Pa	-0.30 dB
Dynamic range	15 to 148 dB(A)	-
Reference	[72]	[73]

Tab. 2.5 – Microphones Characteristics

2.3 Acquisition System

All transducers electrical lines connect to a rack in testing room. Here, the different signals connect to selected devices to be converted from analog to digital and then recorded by the acquisition system. The acquisition system is segregated into an instantaneous and a time-averaged structure, shown in Fig. 2.22. In this structure, all signals used for time-averaged measurements transmit to an Agilent data acquisition unit and are recorded by PC1; in parallel, all signals used for instantaneous measurements transmit to one of two National instruments PCI acquisition cards and are recorded by PC2.
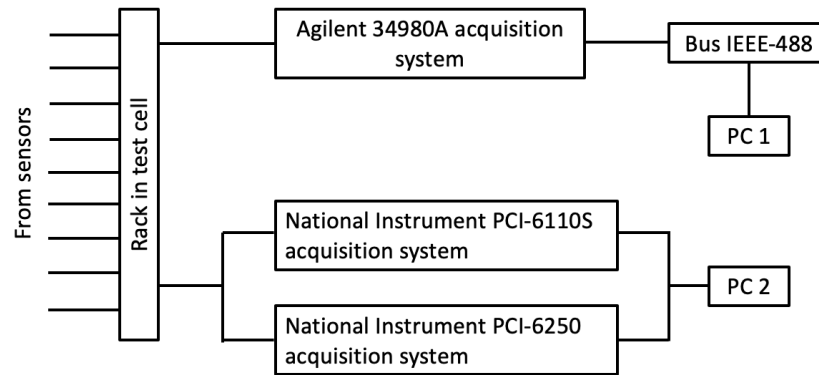
Fig. 2.22 – Data Acquisition Structure

The signal management rack simplifies the connection of different sensors to the two acquisition systems and reduces the complexity of electrical connections between to the acquisition systems. This solution also allows different components to be centralized and connects the test cell to the control room with a reduced number of electric cables. The main components in the rack include the:

- junction box which connects the power supply and acquisition circuits to the Agilent A34980A,

- terminal board which connects the sensors to the high sampling frequency National Instruments acquisition systems, and

- stabilized 24V DC power supply.

Given the need to connect different types of sensors, the terminals in the junction box have been reorganized to directly connect the sensors used during tests. The rack has a capacity of:

- 12 BNC connections,

- 14 thermocouple connections,

- 12 current connections, characterized by a three-cable plug,

- 96 additional three cable plugs used for alternative sensors.

The Agilent A34980A acquisition system collects, handles and post-processes all time-averaged data [74]. The Agilent system can collect signals through a total of 132 channels, of which, 12

are specifically dedicated to current measurements and communicates with the computer PC1 through an ethernet connection. On PC1 LabVIEW TURBO program allows the test operator to set test parameters, visualize and import variables, and start and end the data acquisition from one centralized console; the front panel of this program is shown in Fig. 2.23. A picture of the acquisition system and a detailed description of the program TURBO is provided in section A.2, Measuring Equipment Details.

The two dedicated National Instruments acquisition systems, NI PCI-6110S and NI PCI-6250, collect dynamic measurements and are located in PC2. The PCI-6110S system can collect measurements in 4 channels with a resolution of 12 bits and a sampling frequency up to 5 MHz for each channel [75]. The PCI-6250 can collect data on 16 channels with a resolution of 16 bits and a sampling frequency up to 1.25 MHz for a single channel acquisition and up to 1 MHz for a multiple channel acquisition [76]). A LabVIEW software on PC2 allows the test operator to set the number of channels, the sampling frequency and the acquisition length for all instantaneous signals. PC2 also synchronizes the acquisition of sensors connected to the two different NI PCI acquisition systems.
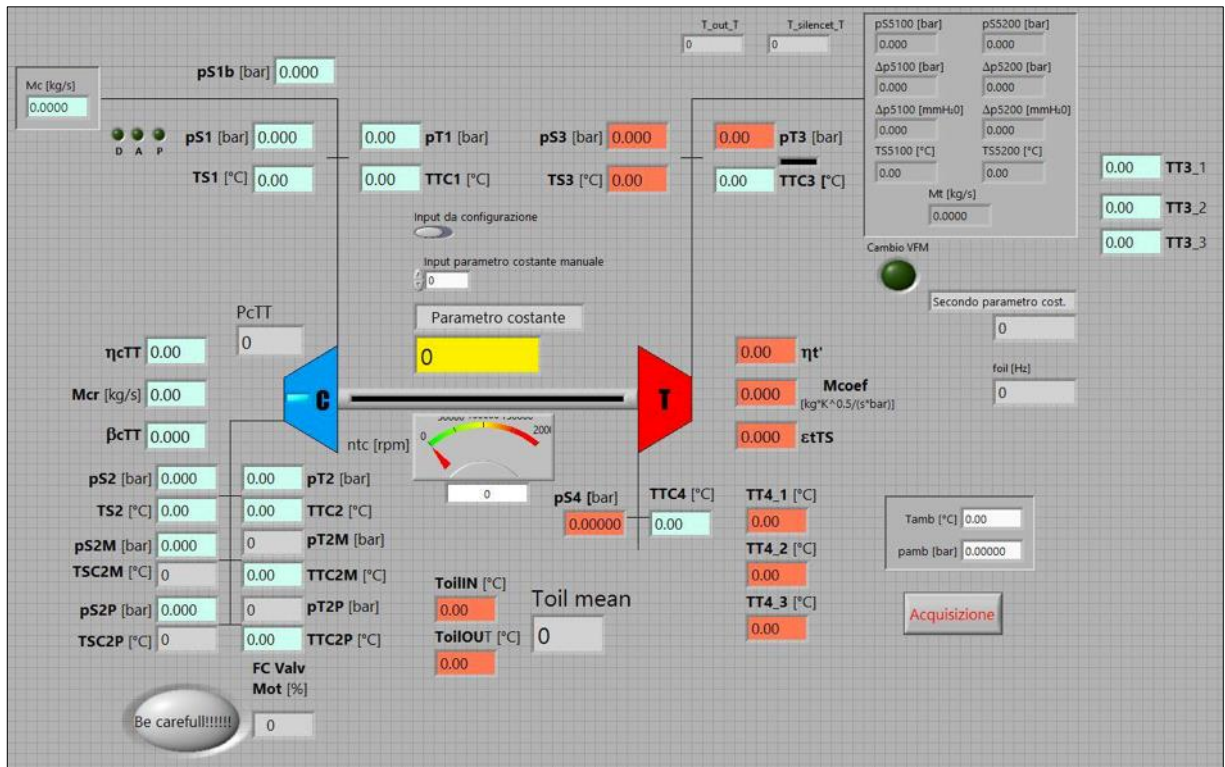
Fig. 2.23 – TURBO.vi Front Panel

34

3   Experimental Investigation

As mentioned in the introduction, the aim of this work is to understand the physical phenomena that lead to a transition from stable to unstable operation in automotive turbocharger compressors and to develop a physics-based control-oriented model to predict and avoid surge. The experimental tests conducted for this purpose are divide into two sets. The first obtained information on the physics behind the compressor behavior. The information collected during this set of tests was used to develop a 1-D physics-based compressor model. Since the model required validation over an extended range of operating conditions, the second experimental investigation collected data to validate the model and extend the knowledge on centrifugal compressor surge behavior. This chapter contains a description of the turbocharger characteristics, followed by the test set-up, measuring stations, test procedures and operating conditions, and finally the techniques used to identify surge. The test set-up and procedures subchapters describe the first set of experimental tests and the modifications introduced in the second set of experimental tests.

3.1   Turbocharger's Geometric Characteristics

The turbocharger used for the test is an IHI model RHF3. An IHI model RHF3 turbocharger is a small turbocharger that can reach high speed (up to 220000 rpm). This turbocharger is used on 4-cylinder gasoline engines with a displacement of 1.4 liters [60]. A disassembled view of the turbocharger is shown in Fig. 3.1. The disassembled view shows the shaft coupled to the compressor and turbine impellers, the oil casing and the compressor and turbine casings. The turbocharger's waste-gate valve is left completely closed for the testing conducted in this thesis.
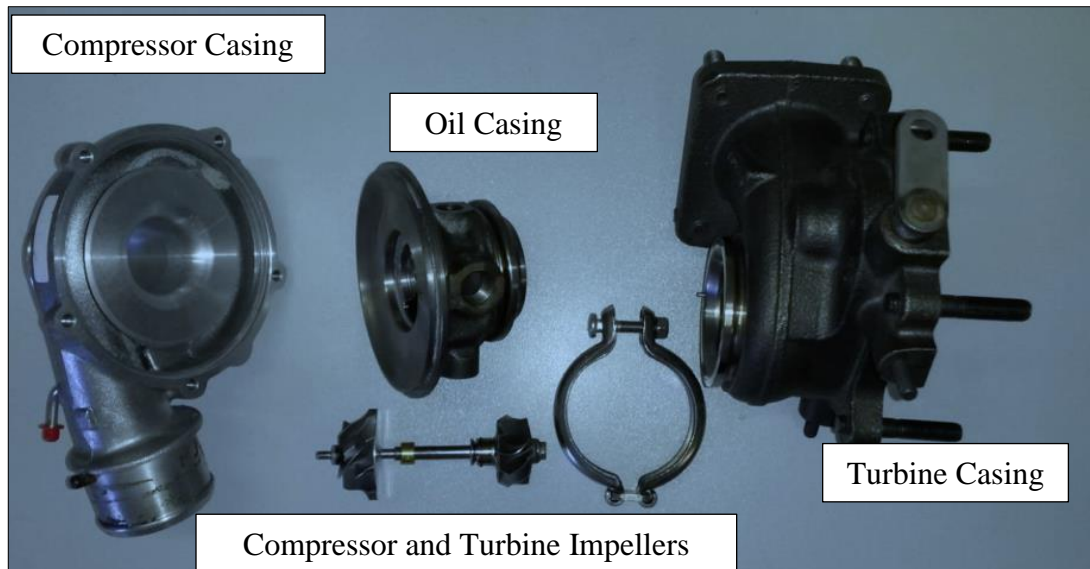
Fig. 3.1 – Disassembled IHI RHF3 turbocharger

3.1.1   Compressor Impeller and Casing

The compressor impeller, shown in Fig. 3.2, is made of aluminum alloys, which make the wheel very light, highly workable and cheaper compared to other alloys such as Titanium [60]. The diffuser is vaneless and has constant height channels.
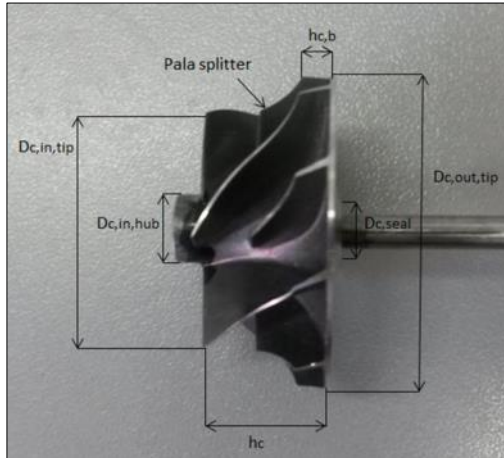
Fig. 3.2 – Compressor Impeller

The number of blades, indicated with z_c, is the sum of the splitter and regular blades. The blade number includes splitter blades (visible in Fig. 3.2), which have the function of guiding the flux and reducing the slip phenomenon. It is important to add splitter blades to reduce the size of the vortexes generated from the slip phenomenon as these vortexes deflect the flux's direction and increase in size when the channel size increases. The main characteristics of both the wheel and the casing are listed in Tab. 3.1.

Parameter	Value	Description
$(A/R)_c$	16.62 mm	Surface to radius ratio of the volute
2a	0.029 m	Major axis of elliptical section equivalent to volute's outlet section
2b	0.026 m	Major axis of elliptical section equivalent to volute's outlet section
$D_{c,diff}$	0.0764 m	Diffuser diameter
$D_{c,in,hub}$	0.009 m	Hub diameter at the rotor inlet
$D_{c,in,tip}$	0.0314 m	Diameter at the tip of the blade at the rotor inlet
$D_{c,out,tip}$	0.04 m	Diameter at the tip of the blade at the rotor outlet
$D_{c,pipe,out}$	0.033 m	Outlet pipe diameter
$D_{c,pipe,in}$	0.0443 m	Outlet pipe diameter
$D_{c,seal}$	0.00735 m	Seal diameter
h_c	0.0155 m	Total height of the rotor
$h_{b,c}$	0.00395 m	Blade height at the rotor outlet
m_c	0.015 kg	Impeller mass
m_{dl}	0.0005 kg	Clamping nut of rotor mass
$R_{c,vol}$	36 mm	Volute azimuthal radius
s	0.5 mm	Distance between rotor back-plate and casing
z_c	10	Blade number
β_{1blade}	37.3 °	Impeller inlet blade angle
β_{2blade}	54 °	Impeller outlet blade angle
ρ_{alu}	2700 kg/m^3	Alufont density, impeller's material

Tab. 3.1 – Compressor Geometric Characteristics

3.1.2 Bearing Unit

The turbocharger bearing unit contains one thrust bearing on the compressor side and two semi-floating journal bearings located on both the compressor and turbine side. Tab. 3.2 reports all bearing's geometric characteristics, where the values of R_{re}, R_{ri}, b_j, b_e, D_{hole}, C_i, C_e and m_{jb} are the same for both journal bearings.

Parameter	Value	Description
b_e	0.00515	Floating ring external axial length
b_i	0.0045 m	Floating ring internal axial length
C_e	0.00011	External radial clearance
C_i	0.00001 m	Internal radial clearance
D_{hole}	0.001505 m	Diameter of each hole of floating ring
$D_{tb,min}$	0.0068 m	Thrust bearing internal diameter
$D_{tb,max}$	0.01242 m	Thrust bearing external diameter
l_{tb}	0.00186	Distance between opposite pads
m_{jb}	0.001 kg	Floating ring mass
N_0	3	Pad number of each thrust bearing
R_{case}	0.0051 m	Bearing casing radius
R_{ri}	0.00313 m	Journal bearing floating ring internal radius
R_{re}	0.00499 m	Journal bearing floating ring external radius
R_s	0.00312 m	Shaft radius
s	0.0018 m	Width between ring and each side of axial bearing
t_i	0.000282 m	Pad height at the lubricant inlet
t_o	0.000312 m	Pad height at the lubricant outlet
γ	1.351 rad	Pad opening angle

Tab. 3.2 – Bearing Unit Geometric Characteristics

3.1.3   Turbine Impeller and Casing

The turbine impeller, shown in Fig. 3.3, is made of Inconel 718 to resist to the high temperatures of the engine exhaust gases. Turbine characteristics are listed below in Tab. 3.3, where the values of turbine impeller, shaft and turbine clamping nut masses have been measured together as these components can't be disassembled.
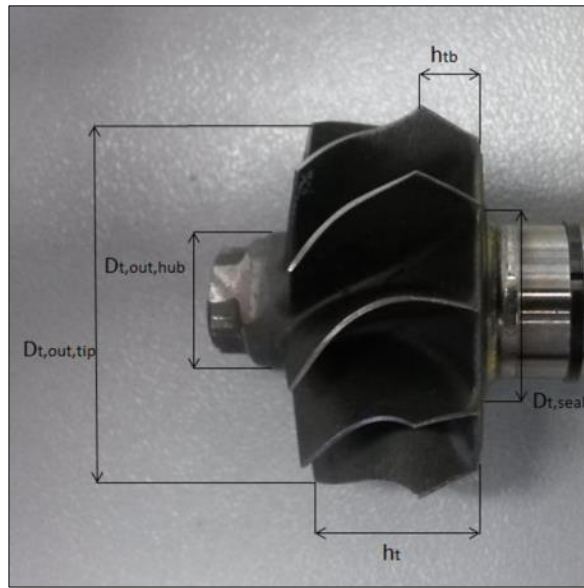
Fig. 3.3 – Turbine Impeller

Parameter	Value	Description
ρ_{inco}	7920 kg/m3	Inconel density, impeller material
$(A/R)_t$	10.5 mm	Surface to radius ratio of the volute
$D_{t,out,hub}$	0.0114 m	Hub diameter at the impeller outlet
$D_{t,pipe,in}$	0.046 m	Intake pipe diameter
$D_{t,pipe,out}$	0.054 m	Outlet pipe diameter
$D_{t,in,tip}$	0.033 m	Diameter at blade tip at the turbine inlet
$D_{t,out,tip}$	0.0284 m	Diameter at blade tip at the turbine outlet
$D_{t,scallop}$	0.02395 m	Scallop diameter
$D_{t,seal}$	0.01265 m	Seal diameter
h_t	0.0129 m	Total impeller height
h_{tb}	0.0044 m	Inlet blade height
m_{tot}	0.055 kg	Mass of the turbine clamping nut and shaft
$R_{t,vol}$	27.6 mm	Volute azimuthal radius

Tab. 3.3 – Turbine Geometric Characteristics

3.2 Experimental Set-Up

The experimental set-up for the first experimental investigation was designed to identify surge precursors and to study the effects of the compressor outlet circuit on the transitions to unstable

39

behavior as described in detail in following subsection. The aim of the second experimental investigation was to collect data to validate the model. This required modifying some features of the set-up. The modification introduced in the second experimental investigation are described in the second subsection.

3.2.1 First Experimental Investigation

Surge is a global phenomenon because it is caused by the pressure differences between the compressor outlet and different points along the circuit surrounding the compressor. To fully study this phenomenon, the experimental layout was designed to allow the analysis of the effects that the entire system has on the transition into surge operation. The design objective was to create a modular compressor outlet circuit that allowed the test operator to easily change the length and volume of the circuit. A schematic of the experimental layout is shown in Fig. 3.4.
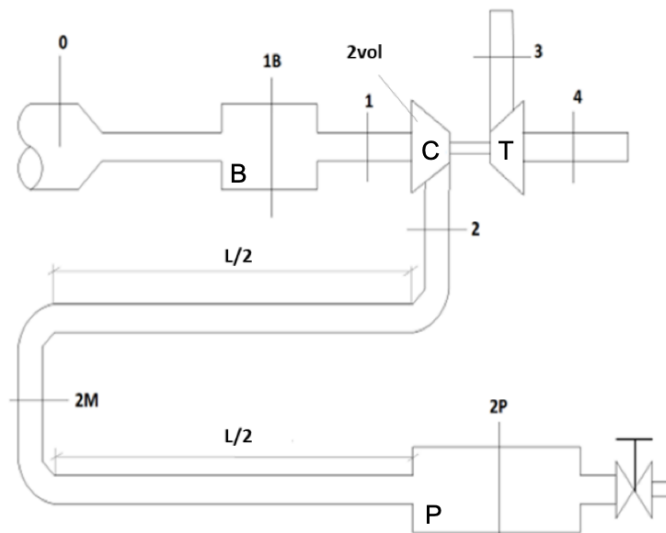
Fig. 3.4 – Schematic Representation of the Experimental Layout

The designed compressor feeding line connects to the controlled pressure compressor feeding line of the test bench. This configuration allows the test operator to maintain the compressor inlet pressure equal to the test cell ambient pressure. A 2-liter plenum is upstream of the compressor, denoted by a "B" in Fig. 3.4. This plenum damps the oscillations generated by surge and allows a more accurate measurement of the average mass flow rate entering the experimental compressor feeding line, measured at Station 0 in Fig. 3.4; a steady flow increases the accuracy of the mass flow rate measurement. The pipe located downstream of the plenum and upstream of the compressor is 44 mm in diameter and 700 mm in length. This pipe was designed to include measuring equipment at 150 mm from the compressor inlet, referred to as Station 1. This specific distance between the measuring station and the compressor prevents interference between the invasive sensors and the compressor. A detailed view of the inlet pipe is shown in Fig. 3.5.

40
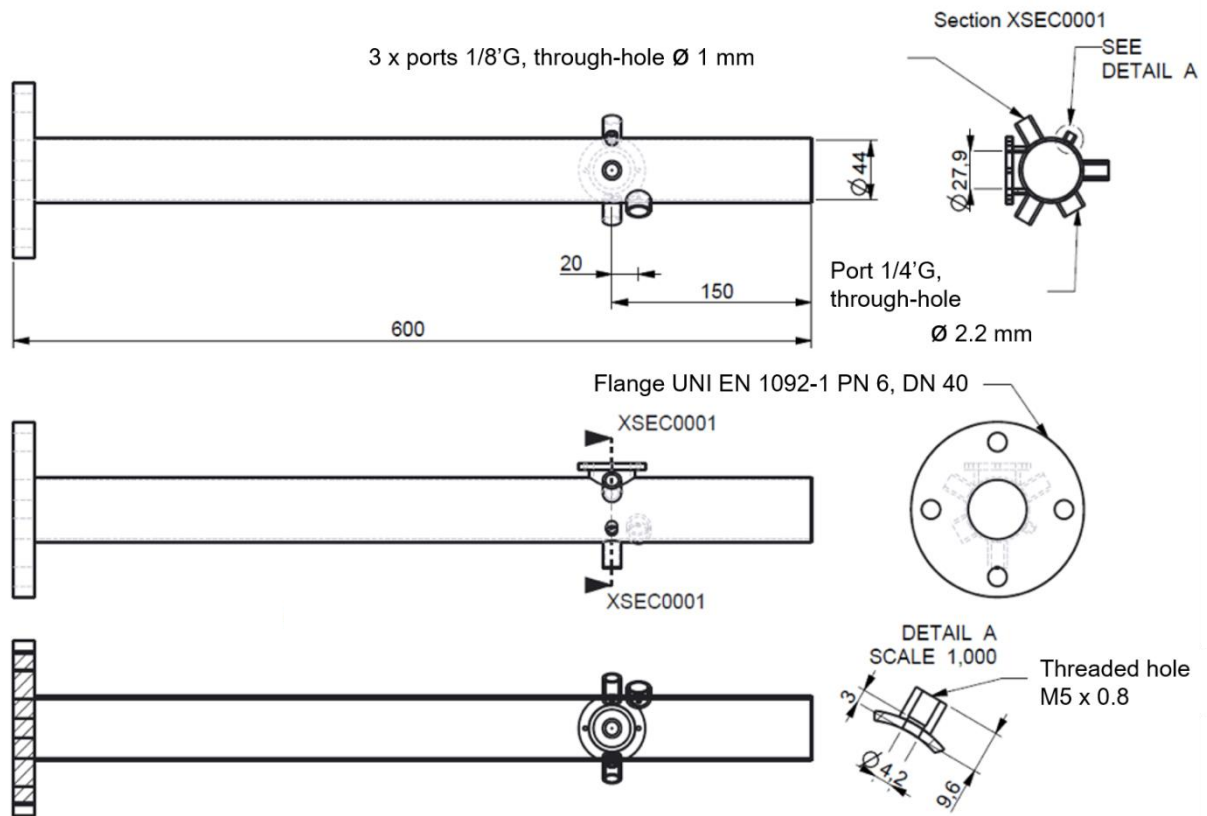
Fig. 3.5 – Compressor Inlet Pipe

Measuring Station 2 is downstream the compressor and was designed following the same criteria as the compressor inlet measuring station. The modular component of the compressor outlet circuit is located downstream of Station 2. The modular circuit consists of a variable length U-shaped pipe that feeds a plenum with a modular volume. The modular components of the pipe and the plenum are connected by flanges which allow the test operator to easily change the circuit characteristics, as shown in Fig. 3.6 on page 42. The modular part of the pipe has two segments and an additional measuring station between the two segments. The total length of the pipe system is the sum of the length of the modular pipe and the length of the 1.6 m fixed U-shape component, this component included the measuring station 2M. The compressor outlet pipe has an inlet diameter of 36.6 mm (volume per unit length equal to 1.052 liters) and the modular component was designed to add up to 4.5 m in steps of 0.5 meters. This choice allows a variation of the outlet circuit total length between 1.6 m (length of the fixed pipe) and 6.1 m. The modular plenum, denoted by a "P" in Fig. 3.4, is made up of different components with a constant diameter of 160.3 mm. The plenum's volume varies between 2 and 14 liters in steps of 1 liter. The smallest plenum segment has a volume of 2 liters and a width of 100 mm, which is the minimum width to provide space for the installation of all sensor taps.

Fig. 3.6 – Experimental Layout

3.2.2 Second Experimental Investigation

To accurately characterize the model, it was necessary to design a compressor inlet circuit that could suck air from the environment to eliminate the impact of the compressor feeding line. Two different inlet circuit configurations were used in combination with the modular compressor outlet circuit discussed previously. The first connected to the test bench filter compressor feeding line, which sucks air from the environment and through a filter. The second consists of a 70 cm pipe that sucks air from the environment. The first configuration consists of a long inlet pipe with a diameter of 105.3 mm and a length of 6 m that connects the filter to the compressor inlet pipe. This set up corresponds to the set up in Fig. 3.4 with the difference that the plenum located at the inlet was removed. This configuration allows the use of the mass flow rate sensor for the measurement of the average mass flow rate in the compressor and is referred to as the "filter configuration". The second configuration only uses the compressor inlet pipe, shown in Fig. 3.5, which feeds directly from the environment through a finely meshed metal grid, as shown in Fig. 3.7. This is referred to as the "open inlet configuration". The grid traps particles to avoid dust entering the compressor. The test cell ambient conditions were monitored during tests to provide constant boundary conditions for the model.
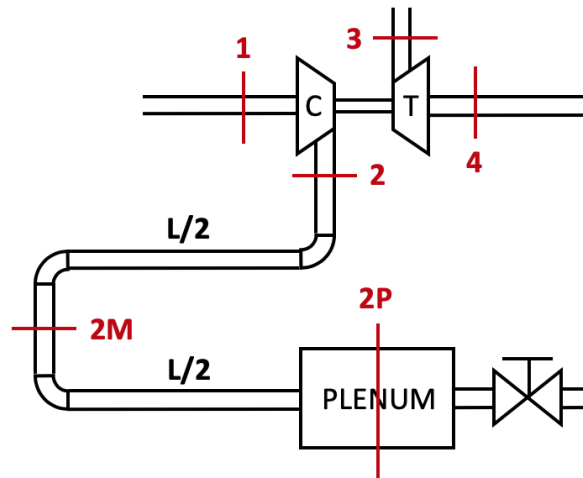
Fig. 3.7 – Modified Layout for Second Experimental Investigation

3.3 Measuring Stations

The measuring stations used were different for the first and second experimental investigations. All the measurements collected during the tests are listed in Tab. 3.4 and Tab. 3.5. In the table, the names of the measuring stations refer to the nomenclature introduced in Fig. 3.4 and Fig. 3.7. Some differences between the first and second experimental investigation are bolded in the table. In the following sections, each measuring station is described in more detail.

43

Location	Description
0C	Compressor mean mass flow rate
1B	**Static pressure in the inlet plenum**
	Mean total temperature in the inlet plenum
1	Static pressure at the compressor inlet
	Mean total temperature at the compressor inlet
	Radial vibration at compressor inlet
2vol	Static pressure in the compressor volute
Casing	Turbocharger rotational speed
	Radial vibration of compressor casing
	Tangential vibration of compressor casing
	Axial vibration of compressor casing
	Acoustic pressure at compressor casing
2	Static pressure at the compressor outlet
	Mean total temperature at the compressor outlet
	Radial vibration at compressor outlet
2M	Static pressure in the compressor outlet pipe
	Mean total temperature in the compressor outlet pipe
2P	Static pressure in the outlet plenum
	Mean total temperature in the outlet plenum
0T	Turbine mean mass flow rate
3	Mean static pressure at the turbine inlet
	Mean total temperature at the turbine inlet
4	Mean static pressure at the turbine outlet
	Mean total temperature at the turbine outlet

Tab. 3.4 – Measurements Taken During the First Experimental Investigation

Location	Description
F	**Acoustic pressure at filter entrance**
0C	Compressor mean mass flow rate
1	Static pressure at the compressor inlet
	Mean total temperature at the compressor inlet
	Mass flow rate at compressor inlet
	Radial vibration at compressor inlet
2vol	Static pressure in the compressor volute
Casing	Turbocharger rotational speed
	Radial vibration of compressor casing
	Tangential vibration of compressor casing
	Axial vibration of compressor casing
	Acoustic pressure at compressor casing
2	Static pressure at the compressor outlet
	Mean total temperature at the compressor outlet
	Mass flow rate at compressor outlet
	Radial vibration at compressor outlet
2M	Static pressure in the compressor outlet pipe
	Mean total temperature in the compressor outlet pipe
2P	Static pressure in the outlet plenum
	Mean total temperature in the outlet plenum
0T	Turbine mean mass flow rate
3	Mean static pressure at the turbine inlet
	Mean total temperature at the turbine inlet
4	**Static pressure at the turbine outlet**
	Mean total temperature at the turbine outlet

Tab. 3.5 – Measurements Taken During the Second Experimental Investigation

3.3.1   Compressor Inlet Circuit Measuring Stations

During the first experimental investigation, one instantaneous pressure sensor (7.23), one average pressure sensor (7.13) and one resistance thermometer were installed in at Measuring Station 1B in plenum "B", located upstream of the compressor inlet. The average pressure in the plenum was measured by connecting a pressure sensor to three pressure taps located 120° apart around the circumference of the plenum. The measured pressure was the average of the pressure at these three pressure taps. The instantaneous pressure sensor was installed flush with the inner wall of the plenum, allowing a fast response to pressure variations. The temperature sensor was located 10 mm after the pressure sensors to avoid the flow disturbances caused by the temperature sensor impacting the pressure measurement.

Fig. 3.8 – Measuring Station 1B (Plenum "B")

One average pressure sensor (7.12), one instantaneous pressure sensor (7.22) and one resistance thermometer were placed in Measuring Station 1, as shown in Fig. 3.9. A hot film anemometer was inserted in Measuring Station 1 to measure the instantaneous local mass flow rate. The anemometer was positioned perpendicular to the flow and in the center of the pipe. The accelerometer PCB Model 352C33 was attached on the section of pipe between this station and the compressor inlet to measure the radial component of the vibration.
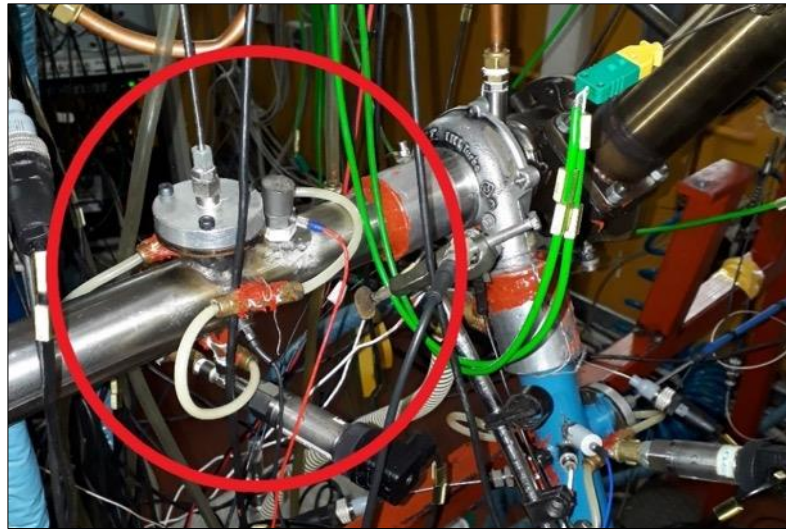
Fig. 3.9 – Measuring Station 1 (Compressor Inlet)

3.3.2 Compressor Casing and Outlet Circuit Measuring Stations

The compressor casing was instrumented with pressure, rotational speed and vibration sensors. The instantaneous pressure sensor 7.15 measures the instantaneous pressure at the compressor diffuser outlet. The PICOTURN BM-V6 measures the turbocharger rotational speed. Finally, three Brüel & Kjær type 4393 accelerometers were attached to the compressor casing to measure acceleration in three directions as shown in Fig. 3.10.
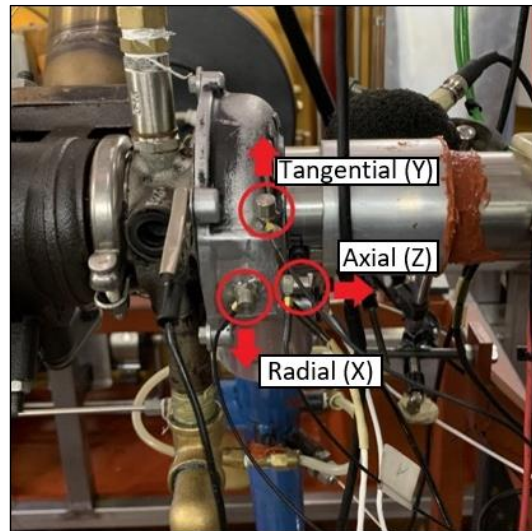
Fig. 3.10 – Acceleration Installation on Compressor Casing

The outlet circuit included three measuring sections. The Measuring Station 2 is 100 mm downstream the compressor and utilized the same instrumentation set-up as Measuring Station 1. The average pressure sensor in Measuring Station 2 is 7.06, while the instantaneous pressure sensor in Measuring Station 2 is 7.16. The two following measuring stations are Measuring Station 2M and Measuring Station 2P. Measuring Station 2M is located half way between the

compressor and the plenum and shown in Fig. 3.11. Average pressure sensor 7.03 and instantaneous pressure sensor 7.18 were placed in Measuring Station 2M. Measuring Station 2P is located in plenum "P" and shown in Fig. 3.12. Average pressure sensor 7.02 and instantaneous pressure sensor 7.20 were placed in Measuring Station 2M. Both Measuring Station 2M and Measuring Station 2P have the same instrumentation set-up as Measuring Station 1B.
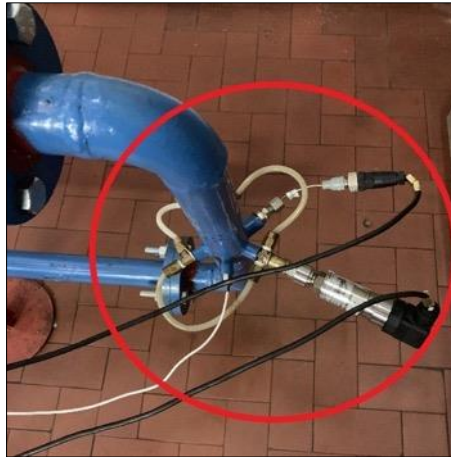
Fig. 3.11 – Measuring Station 2M

Fig. 3.12 – Measuring Station 2P

3.3.3   Turbine Inlet Circuit Measuring Station

Measuring Station 3 is instrumented with a pressure sensor and three thermocouples, shown in Fig. 3.13. The pressure sensor 7.08 is located at the top of a pressure ring to measure the average pressure. Three k-type thermocouples provided a more accurate measure the temperature than if only one had been used.
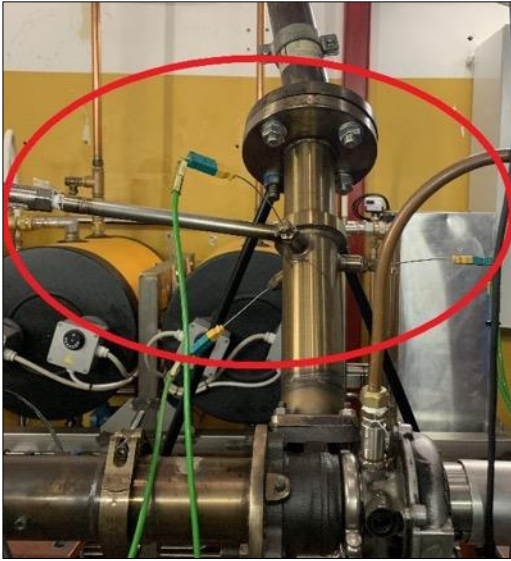
Fig. 3.13 – Measuring Station 3 (Turbine Inlet)

3.3.4 Turbine Outlet Circuit Measuring Station

The Measuring Station 4 is used the same instrumentation set-up as Measuring Station 3. However, resistance thermometers were used instead of thermocouples because the temperature is lower and resistance thermometers are more accurate. In the second experimental investigation, one Kulite sensor 7.23 measured the instantaneous pressure value at the turbine outlet. This sensor was installed to determine if the speed oscillations generated during surge propagated to the flow at the turbine outlet.

3.4 Testing Procedures and Operating Conditions

The testing procedures and operating conditions identified for the first experimental and second experimental investigation are explained in this section. The experiments were designed with the purpose of quantifying compressor behavior in steady-state, transient and surge conditions with the aim of informing and validating the development of a physics-based model. The first experimental investigation was performed prior to any model development and had the primary goal of aggregating a set of information to guide construction of the model. The second experiment was conducted as continued development of the model and analysis of the results of the first experiment identified crucial parameters that had not been measured. The experimental configurations differ to collect a higher set of data and test additional transient conditions, but the steady state operating conditions remained the same.

3.4.1 First Experimental Investigation

The purpose of the first experimental investigation was to collect data to better understand the phenomena that lead to unstable behavior in the compressor. The plenum volume, the circuit length, the turbocharger corrected rotational speed and the compressor operating point were varied during test. Different circuit configurations were tested to analyze their effects on the

49

transition to surge conditions. Tests were conducted on eight different circuit configurations. These tests correspond to total plenum volumes of 8 and 12 liters and 0, 0.5, 2.5 and 4 modular lengths. The circuit geometric characteristics are shown in Tab. 3.6.

Circuit #	Controlled Circuit Characteristics		Resulting Circuit Characteristics		
	Plenum Volume [l]	Modular Length [m]	Total Length [m]	Pipe Volume [l]	Circuit Total Volume [l]
1	8	0	1.6	1.68	9.68
2	8	0.5	2.1	2.21	10.21
3	8	2.5	4.1	4.31	12.31
4	8	4.5	6.1	6.42	14.42
5	12	0	1.6	1.68	13.68
6	12	0.5	2.1	2.21	14.21
7	12	2.5	4.1	4.31	16.31
8	12	4.5	6.1	6.42	18.42

Tab. 3.6 – Compressor Outlet Circuit Characteristics (First Experimental Investigation)

The turbine inlet temperature and the lubricating oil inlet temperature were controlled during every test. The turbine inlet temperature was kept above 50°C to avoid freezing temperature and ice formation inside the machine after expansion. The oil temperature was maintained at 80°C to minimize the heat exchange between the turbine and the oil casing. The turbine waste-gate valve was closed for the whole duration of the investigations. The sampling frequency for pressure and vibration measurements was 100 kHz while the turbocharger rotational speed was sampled at 1 MHz.

Two sets of runs were conducted: first, five steady state operating conditions were measured, then, a transient run was conducted. For the steady state runs five stable operating conditions were tested. These six runs were tested at five different values of corrected rotational speed and the eight circuit configurations. The corrected rotational speeds used were: 59000, 89000, 118000, 140000 and 162000 rpm. The first steady state point, Run 1, was collected with compressor outlet valve completely open. The next three points, Runs 2 to 4, were collected after closing the motorized valve and concentrating these points close to the surge limit. The fifth steady state point, Run 5, corresponded to the last stable point. The last stable point was found using an iterative process by slowly closing the compressor outlet valve until the compressor entered surge. In each iteration, the initial operating point was brought closer and close to surge until attempting to close the valve would immediately cause the compressor to enter surge. This final operating point is defined as the last stable point. The acquisition of the steady state points lasted 2 second to collect both instantaneous and average measurements.

The acquisition of transient run, Run 6, started from the compressor's last stable point. From the last stable point, the valve was closed to move the compressor operating conditions into surge. The instantaneous measurements during transient tests were collected for 4 seconds and

the average values were taken in the stable condition (last stable point) before the valve was closed.

3.4.2 Second Experimental Investigation

The purpose of the second experimental investigation was to collect data to validate the compressor model. After the development of the model discussed in Chapter 4, it was observed that the instantaneous values of mass flow rate at the compressor inlet and outlet were needed in addition to the measurements collected in the First Experimental Investigation. In addition, the throttle position had only been collected only in steady state conditions but not during transient measurement, this data needed to be collected provide an input to the model. Six different circuit configurations were analyzed during the second set of tests, the combinations are shown in Tab. 3.7.

Circuit #	Controlled Circuit Characteristics		Resulting Circuit Characteristics		
	Plenum Volume [l]	Modular Length [m]	Total Length [m]	Pipe Volume [l]	Circuit Total Volume [l]
1	2	0	1.6	1.68	3.68
2	2	2	3.6	3.79	5.79
3	2	4	5.6	5.89	7.89
4	6	0	1.6	1.68	7.68
5	6	2	3.6	3.79	9.79
6	6	4	5.6	5.89	11.89

Tab. 3.7 – Compressor Outlet Circuit Characteristics (Second Experimental Investigation)

The procedure for the second experiment firs collected data during 5 stable points (runs 1 to 5) steady state operating conditions for a given circuit configuration and corrected rotational speed. The same corrected rotational speeds were used as in the first experiment. All runs from 1 to 8 are performed connecting the designed compressor feeding line to the filter compressor feeding line. Next, the unstable and transient runs were conducted:

-   Run 6, deep surge: After measuring the last stable point, the valve is closed further to move the compressor into surge. When surge oscillations stabilize, the acquisition is started, and the deep surge behavior is recorded. The compressor outlet valve position is constant during acquisition, but compressor speed oscillates.

-   Run 7, speed transient: After moving the compressor back to the last stable point, the compressor speed is lowered to a value that determines the compressor's complete stable behavior. The acquisition is started, and the compressor outlet valve position is fixed, the turbocharger speed is then increased until deep surge occurs. After keeping the compressor in surge conditions for five seconds the speed is reduced to move the operating point out of instability and back to the stable region. This test is conducted with the filter configuration described in chapter 3.2.2, Second Experimental Investigation.

- Run 8, valve transient: Starting from the last stable point, the acquisition is started and, after a 5 second delay, the compressor outlet valve is closed, and the compressor moves into surge. After five seconds in deep surge, the valve is opened, and acquisition is ended after exiting surge operating conditions. This test is conducted with the filter configuration.

- Runs 9 and 10 follow the same procedure as Runs 7 and 8 but change the compressor inlet circuit to the open inlet configuration.

The total number of runs is 10 runs per compressor corrected rotational speed and circuit configuration; this corresponds to 50 runs per configuration and 300 total runs. The acquisition of Runs 1 to 6 last 17 seconds while the Runs 7 to 10, vary from run to run. The sampling frequency was 102.4 kHz for all signals including compressor speed; the high frequency components of the signals were not necessary for model validation as the model does not capture these higher-order dynamics.

3.5 Surge Identification Techniques

Different techniques exist to identify surge behavior in the compressor. The first consists of recording noise emitted by the compressor system during surge. Noise frequencies and amplitudes change dramatically when transitioning from stable to unstable operating conditions. This technique can be used if a microphone with real-time data display is present in the test room.

Surge identification can also use the compressor inlet temperature, which can be measured by positioning a resistance thermometer at the impeller inlet, see Fig. 3.14 for an example. During deep surge, the flow reversal causes an increase in the compressor inlet temperature, caused by the hot compressed flow crossing the compressor toward the inlet. The increase in temperature is not well defined and is dependent on operating conditions, but this behavior appears only in deep surge conditions.
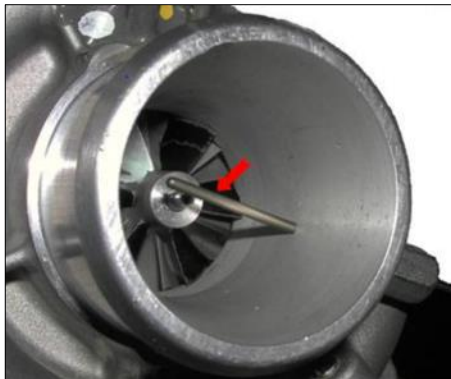
Fig. 3.14 – Resistance Thermometer installed in the Compressor Casing at the Impeller Inlet

A third technique is to monitor the pressure at the compressor outlet and its Fourier transform to identify the presence of the typical low frequency surge oscillations shown in Fig. 3.15. This method offers a more robust solution than the first or second technique, using a sensor with a

faster response than a thermometer and is less sensitive to environmental noise than a microphone. This technique was used for identifying surge during the experimental tests.
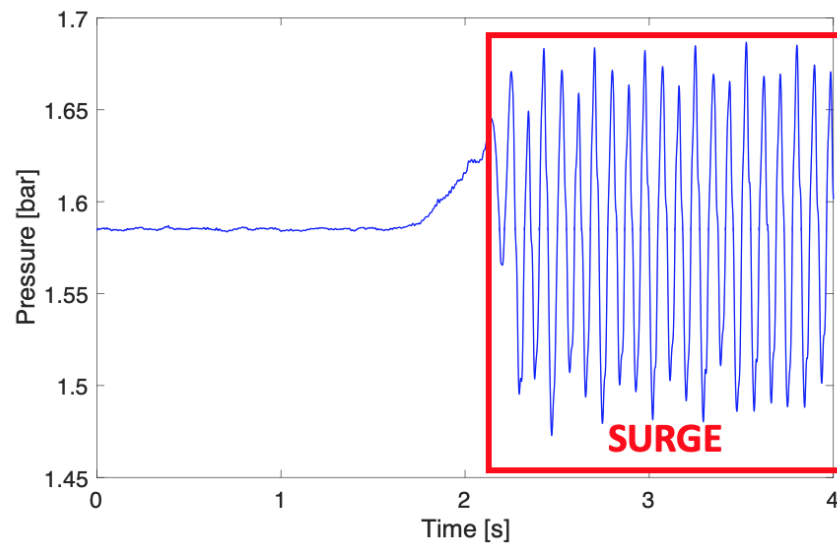
Fig. 3.15 – Compressor Outlet Pressure Signal

4 Model Description

The first experimental investigation provided data and insight necessary to develop a one-dimensional physics-based distributed-parameter model of the compressor and surrounding. This model was designed to predict the compressor's behavior during stable, transient and unstable operating conditions, allowing a deeper analysis of the physical phenomena that lead to a transition from stable to unstable operation. The model discussed in this work was developed in two stages. In the first stage, a compressor model was developed to calculate the compressor steady-state characteristic, simulating stable compressor behavior. In the second stage, a compressor dynamic model was developed using the steady-state model as a foundation; this dynamic model included one-dimensional pipe equations to simulate stable, unstable, and transient behavior of the compressor and surrounding system.

4.1 Steady-State Characteristic Model

The modeled compressor is a centrifugal compressor with a vaneless diffuser and is used in the turbocharger IHI RHF3. The turbocharger's geometric characteristics are discussed in section 3.1, Turbocharger's Geometric Characteristics. The steady-state characteristic model requires the compressor geometric characteristics, the pressure at the compressor inlet, temperature at the compressor inlet and the mass flow rate. The model simulates the compressor's inducer (0-1 in Fig. 4.1), impeller (1-2 in Fig. 4.1) and diffuser (2-3 in Fig. 4.1). The steady-state characteristic of the compressor was calculated by applying the conservation of mass, momentum and energy equations to each component of the compressor. The calculation was performed in three steps: first, the ideal conditions at the specific component outlet were calculated assuming an isentropic transformation; second, those ideal conditions were used to evaluate the losses through the compressor; third, the calculation was repeated including the estimated losses to calculate the real outlet conditions.
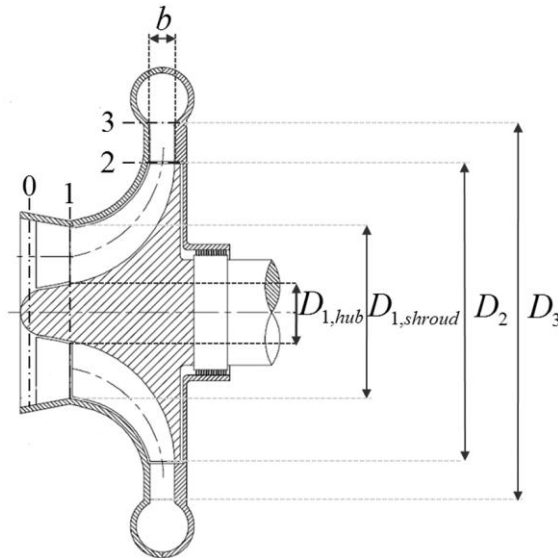
Fig. 4.1 – Compressor Schematic Representation

The inducer is modeled using the convergent nozzle mass flow rate equation (4.1). The reference conditions are the total temperature and pressure at the compressor inlet and are denoted with a subscript zero. The absence of an inlet-guide vane (IGV) at the compressor inlet allowed the losses in the inducer to be neglected and the discharge coefficient was assumed to equal one. When the IGV is present, the discharge coefficient must be correlated to position of the IGV blades.

$$\dot{m} = C_d \Omega_1 \frac{p_{t0}}{\sqrt{RT_0}} \left(\frac{p_1}{p_0}\right)^{\frac{1}{\gamma}} \sqrt{\frac{2\gamma}{\gamma-1} \cdot \left[1 - \left(\frac{p_1}{p_{t0}}\right)^{\frac{\gamma-1}{\gamma}}\right]} \tag{4.1}$$

Where:

- C_d is the discharge coefficient
- Ω is the area of the section
- p and p_t are the static and total pressure
- T is the temperature
- R and γ are the gas constant and the ratio of specific heats

The impeller is modeled using the three conservation equations and two additional equations. The conservation of energy equation in the impeller contains the Euler work, derived by the momentum conservation equation. The two additional equations are required to solve the system of equations and obtain the impeller outlet conditions. One is the adiabatic transformation equation, which relates inlet and outlet conditions. This transformation is implemented to reduce the computational intensity required by a polytropic transformation. The other is the speed triangle relation, which takes into account the slip phenomenon shown in Fig. 4.2. This system of equations is shown in equation (4.2).
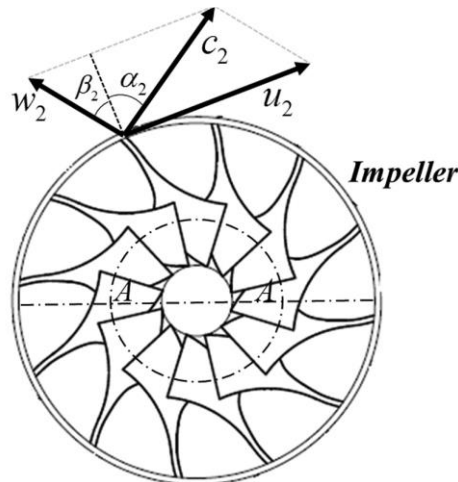
Fig. 4.2 – Impeller Speed Triangles

55

$$\begin{cases} \dot{m} = \rho_2 \Omega_2 c_{r2} \\ c_p(T_{t2} - T_{t1}) = \Delta h_{Euler} - \Delta h_{imp,losses} \\ \Delta h_{Euler} = u_2 c_{\theta 2} - u_1 c_{\theta 1} \\ \rho_2 \cdot T_2^{\frac{1}{1-\gamma}} = \rho_1 \cdot T_1^{\frac{1}{1-\gamma}} \\ \sigma = 1 - \dfrac{c'_{\theta 2} - c_{\theta 2}}{u_2} \end{cases} \tag{4.2}$$

Where:

- $\dot{m}$ is the mass flow rate

- σ is the slip factor

- ρ is the density

- Ω is the area of the section

- p and p_t are the static and total pressure

- T and T_t are the static and total temperature

- c_θ, c_r and u are tangential and radial absolute speeds and the tangential speed of the rotor

- c'_θ is the ideal absolute tangential speed

- Δh_{Euler} and $\Delta h_{imp,losses}$ are the Euler work and the impeller losses

- γ and c_p are the ratio of specific heats and the specific heat at constant pressure. The specific heat at constant pressure is maintained constant in each transformation and it is calculated for each component using the temperature at the component inlet.

The diffuser is modeled using four equations, the three conservation equations and one additional constraint. This additional equation, listed second in the system of equations (4.3), defines the thermodynamic transformation through the diffuser assuming adiabatic conditions. Once the parameters at the diffuser outlet are calculated, the ratio between the total pressure at the diffuser outlet and the inlet pressure provides the compressor total-to-total pressure ratio.

$$\begin{cases} \dot{m} = \rho_3 \Omega_3 c_{r3} \\ \rho_3 T_3^{\frac{1}{1-\gamma}} = \rho_2 T_2^{\frac{1}{1-\gamma}} \\ c_p(T_{t3} - T_{T2}) = -\Delta h_{diff,losses} \\ D_3 c_{\theta 3} = D_2 c_{\theta 2} \end{cases} \tag{4.3}$$

Where:

- $\dot{m}$ is the mass flow rate

- ρ is the density

- Ω and D are the area and diameter of the section

- p and p_t are the static and total pressure
- T and T_t are the static and total temperature
- c_θ and c_r are tangential and radial absolute speeds
- $\Delta h_{diff,losses}$ are the Euler work and the impeller losses
- γ and c_p are the ratio of specific heats and the specific heat at constant pressure. The specific heat at constant pressure is maintained constant in each transformation and it is calculated for each component using the temperature at the component inlet.

The following description of the model contains a detailed analysis of the impeller and diffuser losses, the results of the calibration of the model in the stable region and the analysis of a two-zone compressor model used to extend the calculation of the steady-state characteristic to the unstable region.

4.1.1 Impeller and Diffuser Loss Analysis

A sensitivity analysis was preformed to assess the impact of a variety of different loss correlations on the compressor characteristic. Identifying which loss terms, the compressor characteristic was not sensitive to allowed those to be strategically neglected, reducing the calibration effort and model complexity. This sensitivity analysis focuses on highlighting the impact of several loss models proposed in literature on the shape and position of the compressor characteristic curve. Existing research has identified calculations for incidence, blade loading and disc friction losses [44], [77], [78]. Therefore, these three loss terms do not require calibration. Incidence losses are due to the difference between the blade angle and the relative flow angle at the impeller inlet. Equations (4.4) and (4.5) provides the incidence losses correlation. Without an IGV, the relative flow angle is equal to the blade angle only at design conditions. These conditions are rarely met when the turbocharger is installed on an internal combustion engine. During off-design conditions incidence losses are present and need to be evaluated.

$$\Delta h_{inc} = 0.4 \frac{(\Delta w)^2}{2} \tag{4.4}$$

$$\Delta w = w_{1b} - w_1 \tag{4.5}$$

Where w_1 and w_{1b} are the relative speed and the relative speed calculated using the blade angle, as shown in Fig. 4.3.
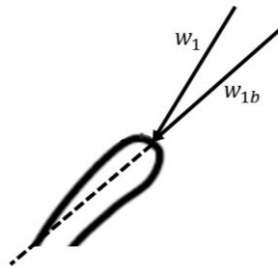
Fig. 4.3 – Incidence Losses at Impeller Inlet

Blade loading losses account for the effect of the pressure gradient on each side of the impeller blade. The pressure gradient decreases the work transferred to the fluid. Blade loading losses are calculated with Equations (4.6) and (4.7).

$$\Delta h_{bld} = 0.05 D_f^2 u_2^2 \tag{4.6}$$

$$D_f = 1 - \frac{w_2}{w_1}\left(\frac{0.75\Delta h_{Euler}/u_2^2}{(\frac{w_1}{w_2})\left[\left(\frac{Z}{\pi}\right)\left(1 - \frac{D_{1t}}{D_2}\right) + 2\frac{D_{1t}}{D_2}\right]}\right) \tag{4.7}$$

Where:

- w and u are the relative flow speed and the tangential speed of the rotor

- Δh_{Euler} is the Euler work

- D_t and D are the tip diameter and diameter of the section

- Z is the number of blades (including splitter blades)

Disc friction losses are caused by the air friction in the small gap between the impeller and the compressor casing. Equations (4.8) and (4.9) calculate disc friction.

$$\Delta h_{df} = f_{df}\frac{\frac{\rho_1 + \rho_2}{2}r_2^2 u_2^3}{4\dot{m}} \tag{4.8}$$

$$\begin{cases} f_{df} = \dfrac{2.67}{Re_{df}^{0.5}} & \text{when } Re_{df} = \dfrac{u_2 r_2}{\nu_2} < 3\times 10^5 \\[3mm] f_{df} = \dfrac{0.0622}{Re_{df}^{0.2}} & \text{when } Re_{df} = \dfrac{u_2 r_2}{\nu_2} \geq 3\times 10^5 \end{cases} \tag{4.9}$$

Where:

- u is the tangential speed of the rotor

- ρ is the density

- r is the radius of the section

- ν is the viscosity of the fluid

The effects of incidence, blade loading, and disc friction losses are shown in Fig. 4.4. In this figure, the ideal steady-state characteristic is compared to the steady state calculation obtained with the addition of each loss and finally the aggregate of all three losses at five values of compressor corrected rotational speed. Fig. 4.4 shows the very low impact of disc friction losses on the steady state characteristic, which consists of a small shift of the curve to a lower value of total-to-total pressure ratio, β_{TT}, and was neglected to reduce calculation and software complexity. Blade loading losses also shift the curve to a lower value of pressure ratio not strongly dependent on mass flow rate. Incidence losses decrease the value of the steady characteristic with a significant magnitude at low mass flow rates, but the magnitude of these losses diminishes as mass flow rate increases. As defined in equation (4.4), incidence losses are

directly correlated to the relative flow speed and, therefore, inversely correlated to mass flow rate.
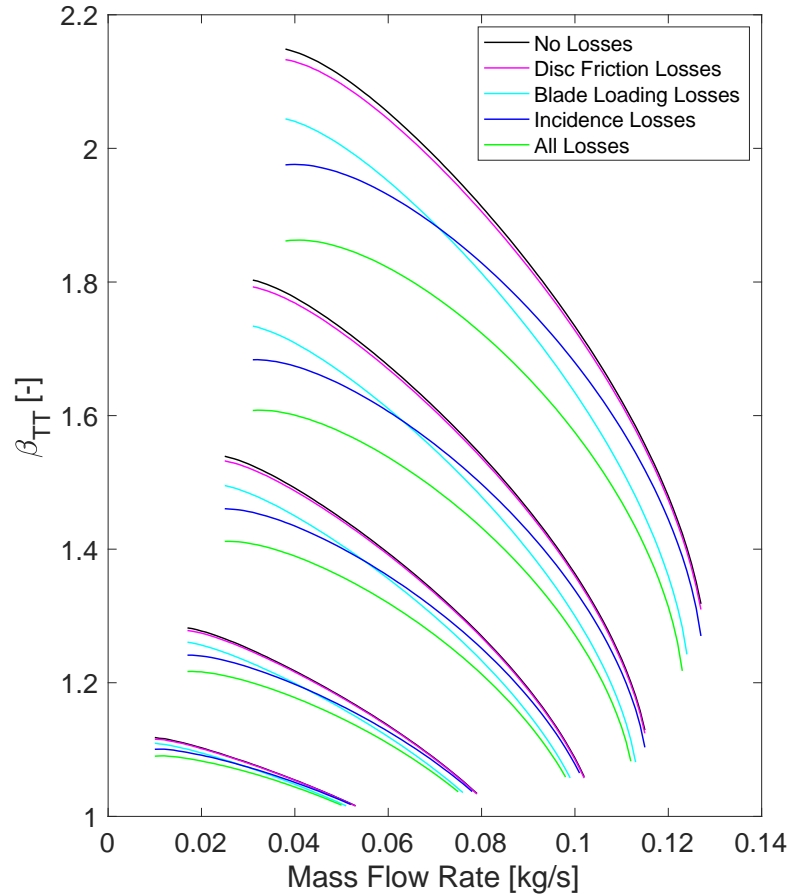
Fig. 4.4 – Effect of Blade Loading, Incidence and Disc Friction Losses on the Steady-State Characteristic

Prior research has identified loss equations for impeller friction, diffuser friction, leakage, clearance, mixing, and recirculation losses. However, these equations each contain calibration parameters that must be tuned against experimental data [44], [79]. Analysis of the steady-state characteristic's sensitivity to each loss was conducted including the incidence and blade loading losses.

The friction losses in the impeller and the diffuser approximate the viscous dissipation that occurs as the flow goes through the respective component [79]. Equations (4.10) and (4.11) defines the impeller friction losses and equation (4.12) defines the diffuser friction losses. The parameters k_{if} and k_{df} represent the friction coefficients in the impeller and diffuser, each parameter is unitless and can have values between zero and one.

$$\Delta h_{if} = 2k_{if} \frac{L_b}{D_{hyd}} \overline{W}^2 \tag{4.10}$$

$$\overline{W} = \frac{c_1 + c_2 + 3w_1 + 3w_2}{2} \tag{4.11}$$

$$\Delta h_{df} = k_{fd} \left(\frac{D_2}{D_3 - D_2}\right)\left(\frac{1}{\alpha_2}\right)\frac{\left(\frac{c_2 + c_{3id}}{2}\right)^2}{2} \tag{4.12}$$

Where:

- k_{if} and k_{fd} are the impeller and diffuser friction coefficients

- L_b, D_{hyd} and D are the length of the fluids path in the impeller, the hydraulic equivalent diameter and the diameter

- c_{id}, c and w are the ideal and real absolute speed and the relative speed

- α is the angle of the absolute speed

The effect of the impeller and diffuser friction losses on the model outputs are shown in Fig. 4.5 and Fig. 4.6. The impeller friction losses decrease the total-to-total pressure, β_{TT}, with a higher magnitude impact at larger mass flow rates and higher corrected rotation speeds. This relationship is caused by an increase in speed of the fluid being related to an increase in friction. The diffuser friction losses have a significant impact at low mass flow rates and the impact increases with corrected rotational speed. Because the diffuser is vaneless, at low mass flow rates the fluid has a greater tangential component in its velocity causing the fluid to have a longer path to exit the diffuser. This longer path increases the total friction losses in the diffuser.
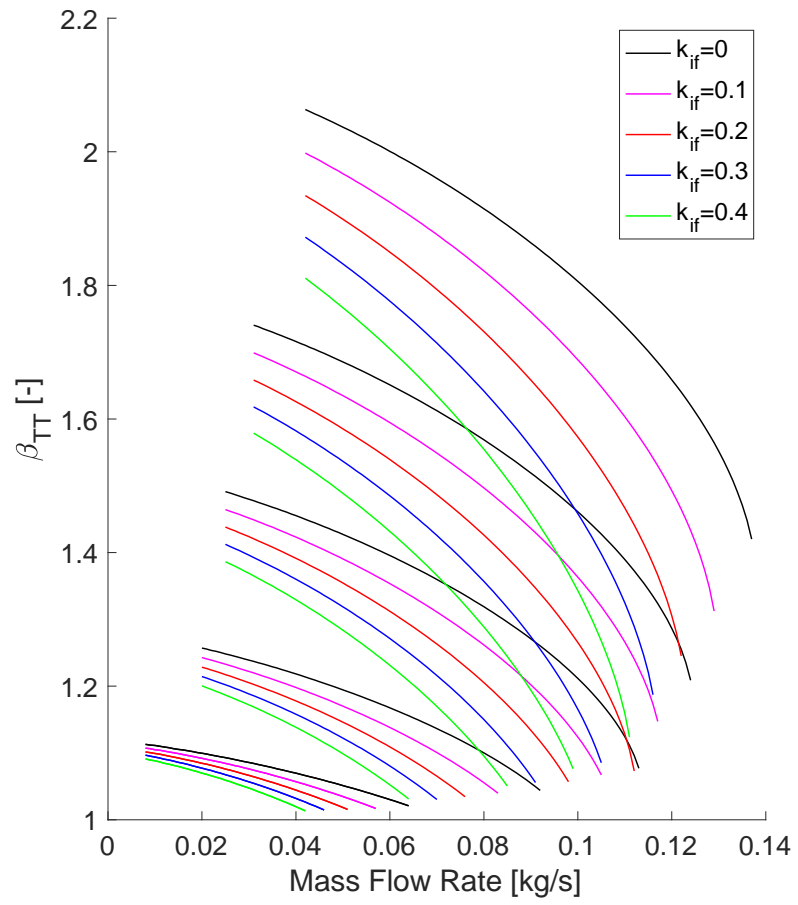
Fig. 4.5 – Effect of Impeller Friction Losses on the Steady State Characteristic
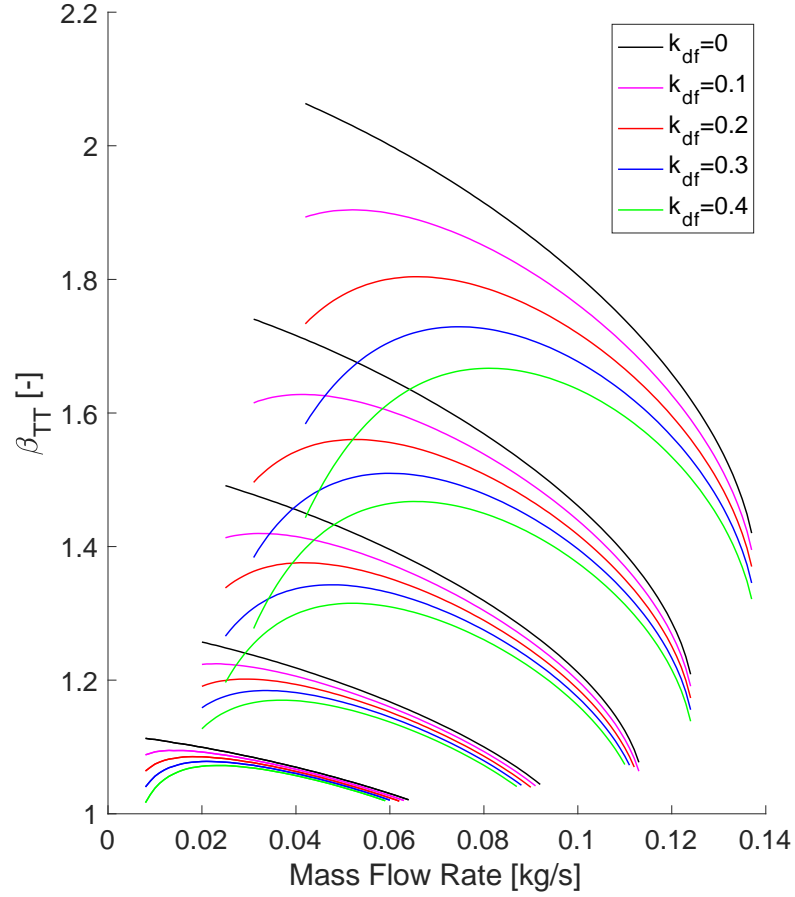
Fig. 4.6 – Effect of Diffuser Friction Losses on the Steady-State Characteristic

Leakage and clearance losses are an aggregated loss defining the impact of the clearance region [44], [79]. The clearance region is a small gap between the impeller and compressor case as a result of the dimensional clearance implemented to prevent interference of the case and blades. Leakage losses approximate the flow that leaks through the compressor seals to areas of lower pressure [44]. The leakage losses are defined in Equations (4.13), (4.14), (4.15) and (4.16). Clearance losses approximate the low energy flow in the impeller gap region between the impeller blades and case and the fluid that exits one blade channel, flows through this region and enters another blade channel [79]. The clearance losses are defined by Equations (4.17).

$$\Delta h_{lk} = \frac{\dot{m}_{cl} u_{cl} u_2}{2\dot{m}} \tag{4.13}$$

$$\dot{m}_{cl} = \rho_2 Z \varepsilon L_\theta u_{cl} \tag{4.14}$$

$$u_{cl} = 0.816 \sqrt{\left(\frac{2\Delta p_{cl}}{\rho_2}\right)} \tag{4.15}$$

$$\Delta p_{cl} = \frac{\dot{m}(r_2 c_{\theta 2} - r_1 c_{\theta 1})}{Z\left(\frac{r_1 + r_2}{2}\right)\left(\frac{\rho_1 + \rho_2}{2}\right)L_\theta} \tag{4.16}$$

$$\Delta h_{cl} = 0.6 c_{\theta 2}\frac{\varepsilon}{b_2}\left\{c_1 c_{\theta 2}\frac{4\pi}{b_2 Z}\left[\frac{r_{1t}^2 - r_{1h}^2}{(r_2 - r_{1t})(1 + \frac{\rho_2}{\rho_1})}\right]\right\}^{0.5} \tag{4.17}$$

Where:

- $\dot{m}$ is the mass flow rate
- ρ is the density
- L_θ, r_t, r_h and r are the length of the blade, the tip and hub radius and the radius
- Z is number of blades (including splitter blades)
- c_θ and u are tangential and flow absolute speeds and the rotor tangential speed
- ε and b are the clearance and the diffuser height

The geometrical parameter ε represents the clearance in the leakage and clearance loss equations, the clearance is measured in meters and can have a value greater than zero, though this clearance in a turbocharger is typically on the order of 10^{-5} meters. Although a geometrical parameter, it is very difficult to measure and is typically treated as a tunable parameter. The effect of the clearance parameter on the model outputs is shown in Fig. 4.7. Leakage and clearance losses increase with corrected rotational speed but are not impacted by mass flow rate. The effect of corrected rotational speed corresponds to increased flow in the clearance space when more momentum is imparted to the fluid orthogonal to the direction of the blade channel. The leakage and clearance losses increase linearly with clearance length as defined in equations (4.13) and (4.17). The magnitude of the leakage and clearance losses result in a small total-to-total pressure decrease and were neglected.
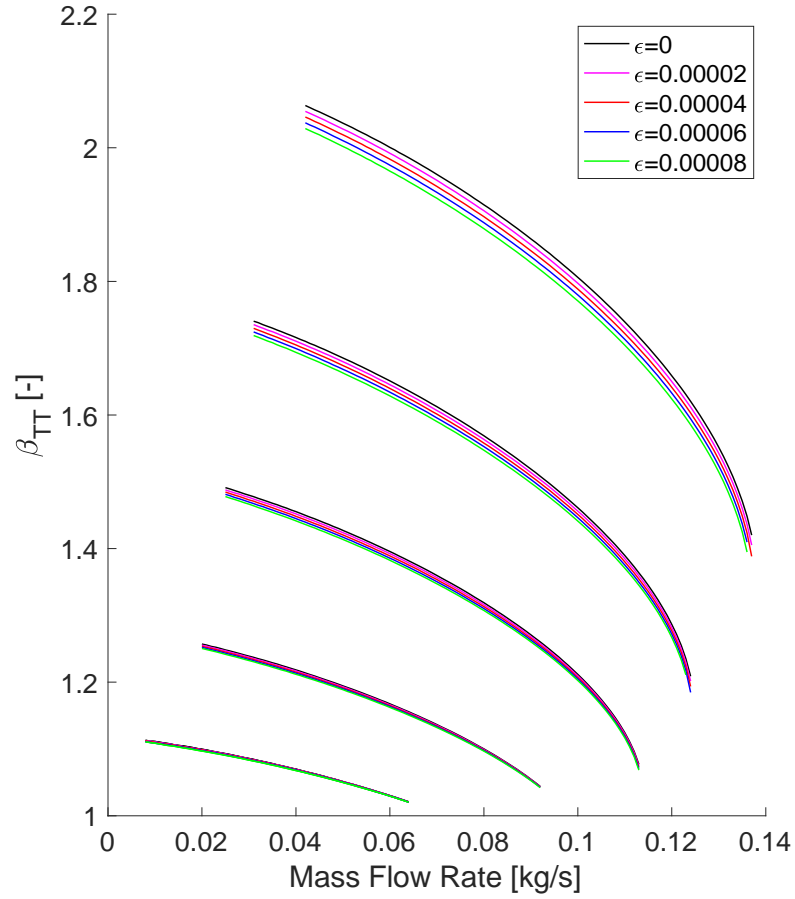
Fig. 4.7 – Effect of Clearance and Leakage Losses on the Steady State Characteristic

The mixing losses approximate the energy dissipation that occurs in impeller wake. These losses are defined by Equation (4.18). The calibration parameter ε_{wake} represents the ratio of the areas of the wake to jet regions in the impeller blade channel [80].

$$\Delta h_{mix} = \frac{1}{1 + tan^2\alpha_2}\left(\frac{1 - \varepsilon_{wake} - b^*}{1 - \varepsilon_{wake}}\right)^2 \frac{c_2^2}{2} \tag{4.18}$$

Where:

- b^* is the ratio between the diffuser height and the height of the blades at the impeller outlet

- c and α are the absolute speed and the absolute speed angle

- ε_{wake} is the ratio between the wake area and the jet area

The mixing losses resulted in a total-to-total pressure decrease that increased in magnitude for higher mass flow rates, this is caused by an increase in the amount of flow in the wake where mixing occurs, this is shown in Fig. 4.8. The magnitude of the pressure decrease is comparable

64

for all compressor speeds, this is because the mixing loss equations are not strongly dependent on the compressor speed. This behavior is not consistent with the behavior of the fluid in the compressor; lower compressor speeds experience larger wake ratios and larger mixing losses. This inconsistency was later addressed with the implementation of a two-zone jet-wake model which replaced these losses.
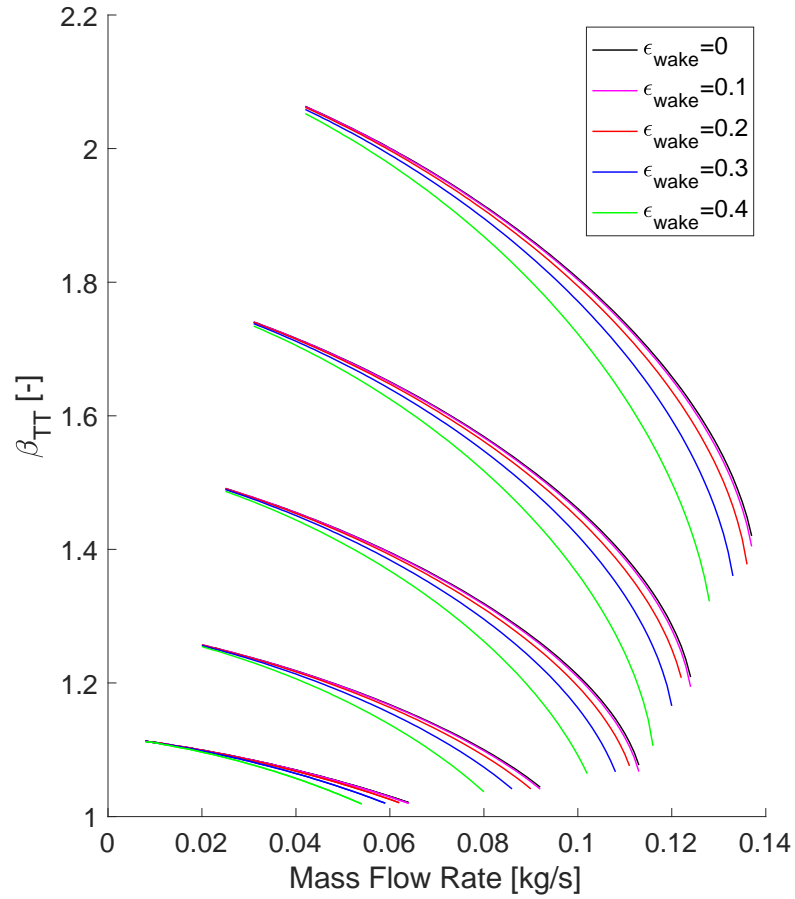
Fig. 4.8 – Effect of Mixing Losses on the Steady State Characteristic

The recirculation losses approximate the flow energy lost due to the reversed flow in the diffuser, which reenters the impeller [43]. The recirculation losses are defined by Equation (4.19) where D_f is the same diffusion coefficient used in the blade loading loss calculation and the parameter k_{recirc} is the recirculation calibration coefficient. The recirculation loss calibration parameter can have a value between zero and one and is unitless.

$$\Delta h_{rc} = k_{recirc} sinh(3.5\alpha_2^3)D_f^2 u_2^2 \qquad (4.19)$$

Where:

- D_f is the diffusion factor calculated in Equation (4.6)
- u and α are the tangential speed of the rotor and the absolute flow speed angle
- k_{recirc} is the recirculation coefficient loss

The recirculation losses result in a dramatic total-to-total pressure decrease for low mass-flow rates, but the magnitude of this impact asymptotically tends towards zero as mass-flow rate increases, this behavior is shown in Fig. 4.9. This behavior is caused by the adverse pressure gradient that drives the recirculation flow being a low flow phenomenon. The magnitude of the total-to-total pressure drop increases with compressor speed. This is because less momentum is imparted to the flow tangential to the direction of the adverse gradient causing more flow to be recirculated. The recirculation losses also create a valuable change to the shape of the iso-speed curve, having a more aggressive concave slope into the surge region.
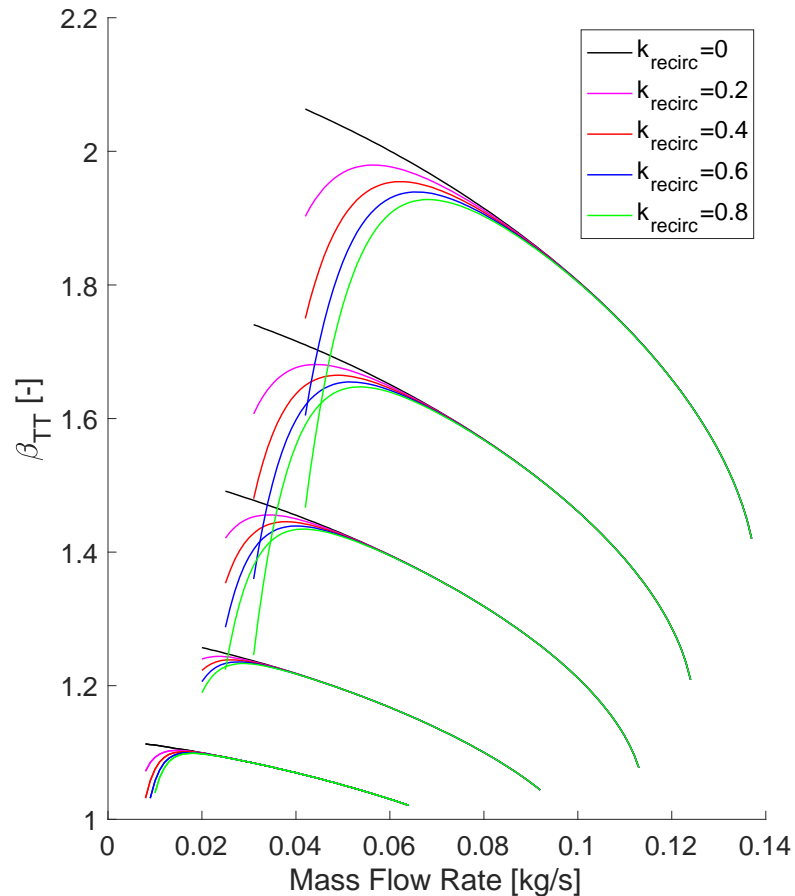
Fig. 4.9 – Effect of Recirculation Losses on the Steady State Characteristic

4.1.2 Calibration Results in the Stable Operating Region

The results of the sensibility analysis were taken into account during the calibration procedure. The calibration of the model in the stable region was performed to prove the model's ability to match experimental data with high accuracy. The calibration of the loss equations presented in the previous section used a procedure based on the reduction of the RMS error between the experimental data and the model results. This iterative process required the manual optimization of the four calibrated values utilizing the unique impacts each parameter had on the shape of the iso-speed curve and knowledge of realistic orders of magnitude for the different types of losses. The final calibration parameters are listed in Tab. 4.1.

Parameter	Final Value	Relevant Losses
k_{if}	0.201	Impeller Friction Losses
k_{df}	0.0227	Diffuser Friction Losses
ε_{wake}	0.313	Mixing Losses
k_{recirc}	0.0558	Recirculation Losses

Tab. 4.1 – Calibration Parameters Used for the Stable Region

These calibration parameters produced the modeled steady-state characteristic shown in Fig. 4.10. In this figure, the lines denote the modeled steady-state characteristic at five corrected rotational speeds and the dots of the same color represent the comparable experimental data collected during the second experimental investigation.
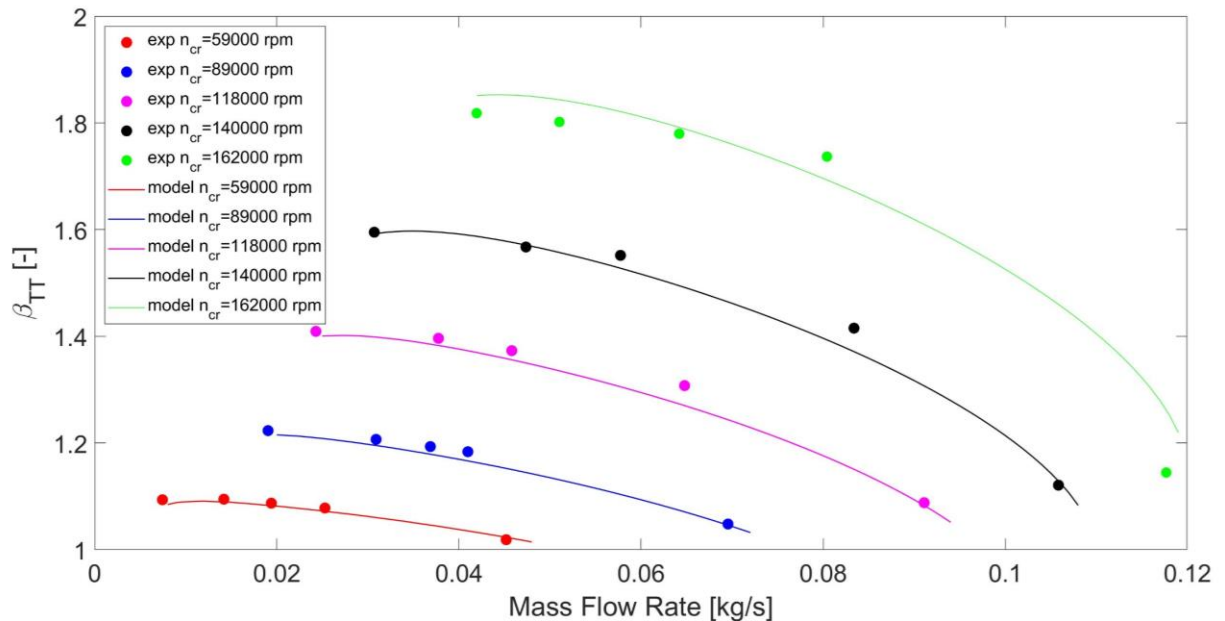
Fig. 4.10 – Steady-State Characteristic for the Stable Operating Region

The RMS error and the average percentage error for each corrected Rotational speed is shown in Tab. 4.2. These results show that the final calibration provided low RMS and percentage error, validating the calibration procedure for the steady state characteristic. Tab. 4.2 also shows that the error increases with the turbocharger rotational speed, highlighting an opportunity in future work to improve the model accuracy with additional optimization of loss terms that are affected by speed, such as friction losses. However, this level of accuracy is acceptable for the validation and discussion of the model presented in this work.

Corrected Rotational Speed [rpm]	59000	89000	118000	140000	162000
Error RMS	0.00701	0.0118	0.0200	0.0228	0.061
Average Percentage Error [%]	0.596	0.887	1.26	1.16	3.50

Tab. 4.2 – Error Between Model and Experimental Data

4.1.3 Jet and Wake Theory for the Extension of the Model to the Unstable Region

As previously identified during the discussion of mixing losses, the mixing loss equations incorporated from literature did not fully represent the dependency of the loss on corrected rotational speed. In low mass flow rate conditions, the flow through the impeller is significantly affected by boundary layer separation phenomena due to the higher incidence angles. Instead of approximating this occurrence with a mixing formulation, this occurrence can be captured by dividing the flow into two regions to better account for the different behavior of the separated region. For this reason, Dubitsky and Japikse's two-zone jet and wake model was incorporated into the compressor model [81].

The boundary layer separation that occurs in centrifugal compressors at low flow rate conditions is a three-dimensional phenomenon. One of the first experimental investigations into this mechanism, conducted by Eckardt, showed how flow develops in the impeller channel and how the speed distribution changes along the height of the channel [36]. Two regions form in the impeller channel due to the pressure difference between pressure and suction side and propagate to the diffuser, making development of models and correlation in both impeller and diffuser necessary.

Several different models have been developed attempting to capture the behavior observed from a two-zone representation. In this representation, the flow area and velocity distribution across the channel is modeled as a superposition of a jet region and a wake region. Dubitsky and Japikse's simplified two-zone jet and wake model of the impeller was based on conservation equations applied to the two regions [81]. A subsequent adaptation proposed by Dean and Senoo was a series of ordinary differential equations to represent the flow in a vaneless diffuser and how the two regions change along the radial direction [37]. In both representations, it was assumed that flow is steady, and the two regions do not to mix. During the development of an advanced vaneless diffuser model, Dubitsky and Japikse removed the no-mixing assumption and introduced a mass flow rate mixing term in the continuity equations [81]. This study was used as reference to modify the diffuser equations.

The calculation process for the impeller equations is minimally modified by duplicating the equations for the jet and wake regions, following the schematic representation in Fig. 4.11. Most

of the assumptions made for the impeller equations are taken from [81], the others are consistent with the assumptions made for the development of the one zone model:

- The static pressure in jet and wake regions are equal. In each region, parameters are constant along the tangential direction ($\frac{\partial}{\partial \theta} = 0$).

- Slip affects jet flow, while wake flow follows the blade.

- Both the jet and wake region have adiabatic transformations. This implies same static temperature and density for the two zones.

- Blade loading and incidence losses are considered in both the jet and wake equations. Friction is only inserted in the wake equations
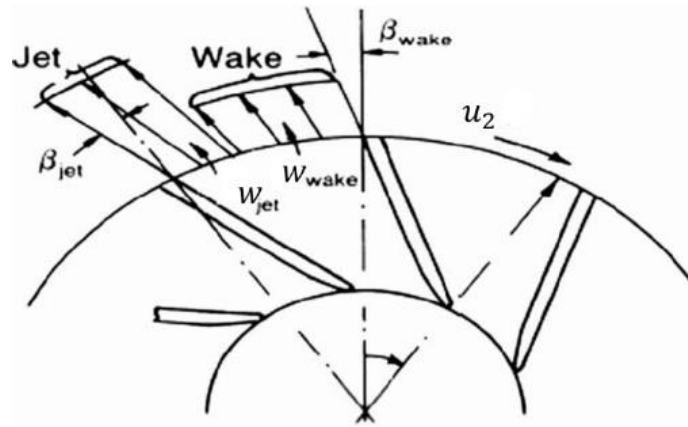
Fig. 4.11 – Jet and Wake Flow Distribution [37]

Based on these assumptions the equations (4.20) defined the jet and wake regions where $i = j, w$, corresponding to jet and wake.

$$\begin{cases} \dot{m}_\iota = \rho_2 \Omega_{2,i} c_{r2,i} \\ c_p \left(T_{t2,i} - T_{t1} \right) = W_{id,i} - \Delta h_{losses,i} \\ W_{id,i} = u_2 c_{\theta 2,i} - u_1 c_{\theta 1} \\ \rho_2 \cdot T_2^{\frac{1}{1-\gamma}} = \rho_1 \cdot T_1^{\frac{1}{1-\gamma}} \end{cases} \qquad (4.20)$$

Where:

- $\dot{m}$ is the mass flow rate

- ρ is the density

- Ω is the area of the section

- p and p_t are the static and total pressure

- T and T_t are the static and total temperature

- c_θ, c_r and u are tangential and radial absolute speeds and the tangential speed of the rotor

69

- W_{id} and Δh_{losses} are the ideal work and the impeller losses

- γ and c_p are the ratio of specific heats and the specific heat at constant pressure

The closing equations correlate radial to tangential speed and are different for the two zones. For the jet zone, the closing equations correspond to the slip equations. While for the wake zone, the closing equations correspond to the speed triangle relations given in Equations (4.21) and (4.22).

$$\sigma = 1 - \frac{c'_{\theta 2,j} - c_{\theta 2,j}}{u_2} \tag{4.21}$$

$$c_{2,w}{}^2 = c_{2r,w}^2 + c_{2\theta,w}^2 \tag{4.22}$$

Where:

- σ is the slip factor

- c_θ, c_r and c'_θ are tangential and radial absolute speeds and ideal absolute tangential speed

- W_{id} and Δh_{losses} are the ideal work and the impeller losses

- γ and c_p are the ratio of specific heats and the specific heat at constant pressure

The jet and wake model introduces two additional parameters: the wake width to total flow area width and the ratio of wake mass flow rate to total mass flow rate. The wake width is an output of the system of equations. The ratio of mass flow rates must be determined prior to solving the system of equations; in this analysis it is considered constant and set to 0.2 [82].

The jet and wake model was implemented to analyze the effect of the development of a loss region on the steady-state characteristic moving towards unstable operating conditions. The model was tested at the five values of corrected rotational speed analyzed during the experimental campaign for values of mass flow rate between 0.001 kg/s and 0.15 kg/s with a step of 0.001 kg/s. The results of this test are shown in Fig. 4.12.
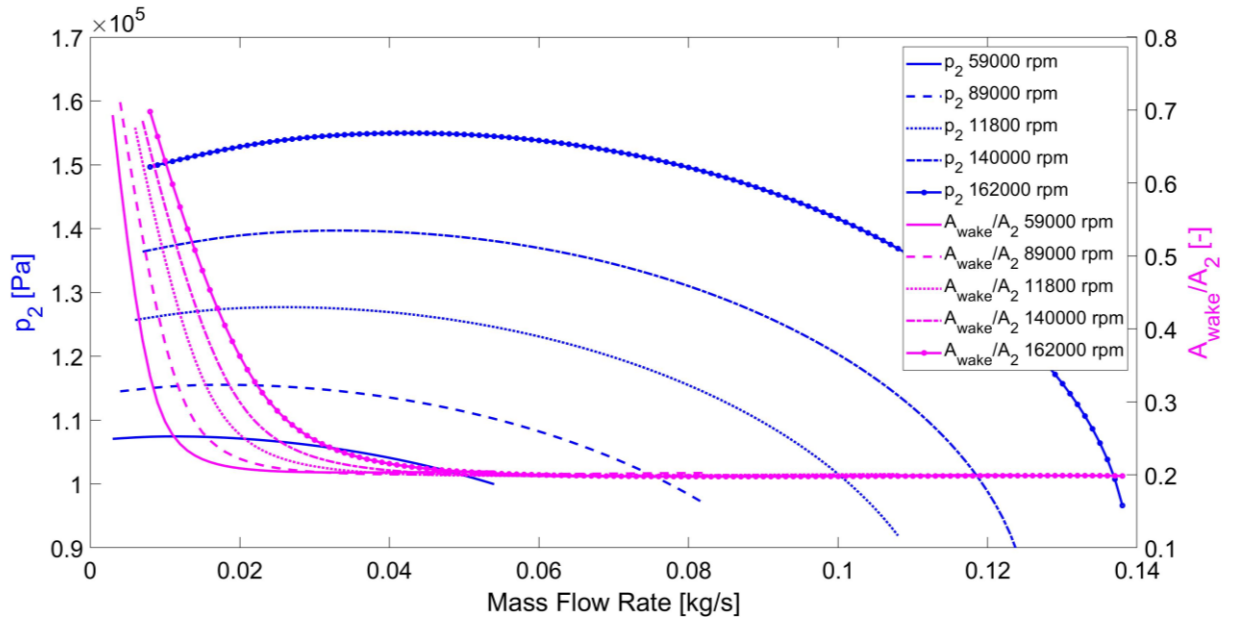
Fig. 4.12 – Jet and Wake Static Pressure and Area Ratio

Fig. 4.12 shows the trend of area ratio across different values of mass flow rate for five different corrected rotational speeds. For low mass flow rates this parameter increases exponentially. This behavior is consistent with the drop in the compressor load, which coincides with a growth of the wake region of the jet and wake model. This trend corresponds to a decrease in the pressure, which is caused when the losses increase, and the wake region widens.
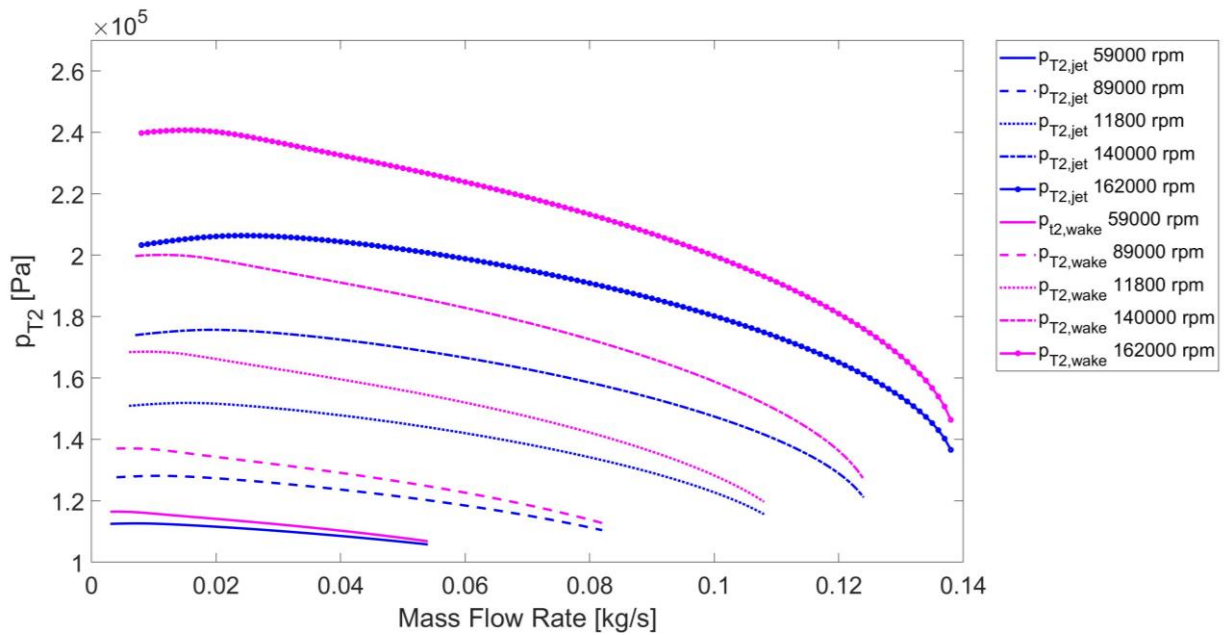
Fig. 4.13 – Total Pressure at the Impeller Outlet for the Jet and Wake Region

71

At this point in the model development, the trend of the modeled total pressure did not correspond to the experimental data found in literature, as shown in Fig. 4.13. An experimental investigation conducted by Marelli [56], shows that the total to total pressure ratio decreases drastically when moving across the surge line from the stable to the unstable region. In Fig. 4.13, the total pressure in both regions increases as the mass flow rate approaches zeros; following a different trend from the one showed in [56]. This is due to the correlation between the radial and tangential components of the speed. The radial component, responsible for the mass transfer between the inlet and outlet of the compressor, decreases to zero as mass flow rate decreases, this is shown in Fig. 4.14. As the mass flow rate approaches zero, the jet speed will tend to $\sigma \cdot u_2$ and the wake tangential speed will tend to u_2, see Fig. 4.15. This is based on the assumption that the wake region follows the blade.
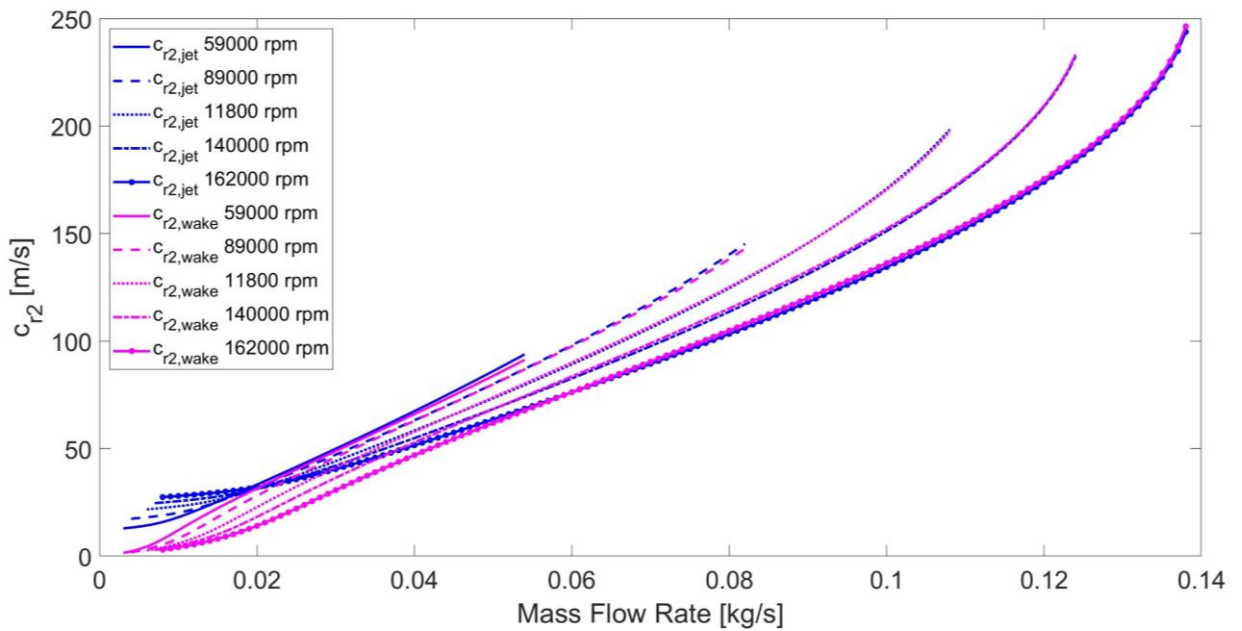
Fig. 4.14 – Absolute Radial Flow Speed for the Jet and Wake Region
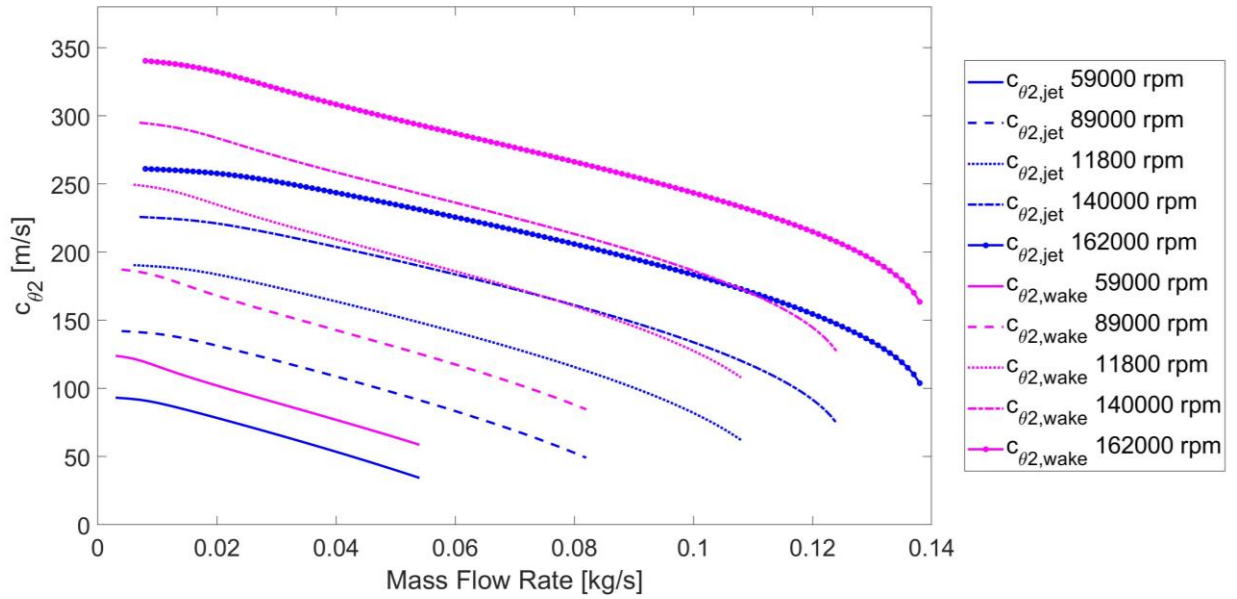
Fig. 4.15 – Absolute Tangential Flow Speed for the Jet and Wake Region

This behavior is because the equations used are not applicable when the compressor works in unstable conditions or close to zero flow conditions. Instead, it is possible to model the drop in the compressor characteristic curve by varying the loss coefficients in the diffuser. The additional losses in the diffuser equations were taken from [37], and are based on modeling the propagation and development of the jet and wake zones in the diffuser.

Given that the shear stress due to the presence of two different speed values is proportional to the difference between the two relative speeds at the impeller outlet, Equation (4.23) was added as an energy loss term in the diffuser equations. The diffuser friction losses were modified using Equation (4.24):

$$\Delta h_{shear} = k_{shear} \cdot \frac{(w_{jet} - w_{wake}) \cdot c_{jet,avr}}{2} \tag{4.23}$$

$$\Delta h_{df} = k_{df} \cdot \frac{1}{2} \frac{(c_{2,jet} + c_{3is})^2}{2} \tag{4.24}$$

Where:

- k_{shear} and k_{df} are the shear loss coefficient and the diffuser friction coefficient
- w and c are the absolute and relative speeds
- c_{avr} and c_{is} are the average and isentropic absolute speeds

The jet and wake model implemented for the impeller is computationally intensive because the system of equations does not have an explicit solution. To obtain a model that could run in real time, the average jet speed and the difference between the two relative speeds was mapped using an offline model and implemented into the real-time model of the compressor. The compressor

map shown in Fig. 4.16 was obtained by recalibrating the model using the terms in equations (4.23) and (4.24) The calibration values used to generate this map are given in Tab. 4.3.
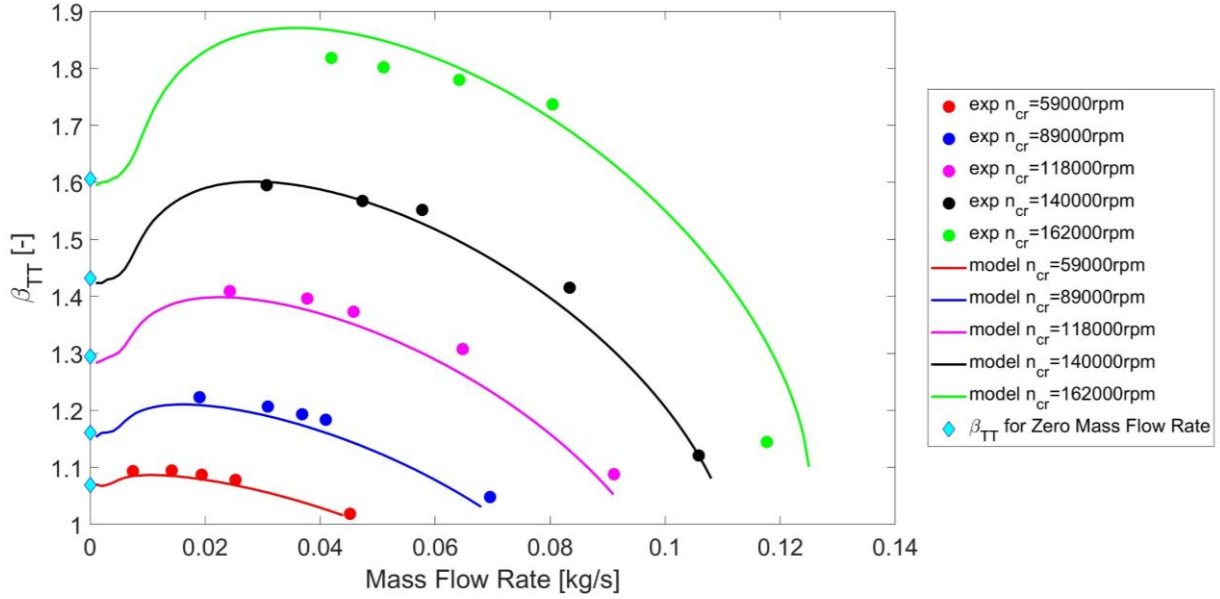
Fig. 4.16 – Steady State Characteristic in Stable and Unstable Operating Conditions

Parameter	Value	Loss that Uses Parameter
k_{if}	0.0351	Impeller Friction Losses
k_{df}	0.0356	Diffuser Friction Losses
ε_{wake}	0.476	Mixing Losses
k_{recirc}	0.00150	Recirculation Losses
k_{shear}	0.435	Shear Losses

Tab. 4.3 – Calibration Results for the Jet and Wake Model

Fig. 4.16 shows that the model is able to simulate compressor in the unstable region while also accurately simulate the pressure ratio at zero mass flow rate. This pressure ratio was compared to values calculated with Equation (4.25) taken from the paper by Marelli [56].

$$\beta_{TT}(\dot{m} = 0) = \left[1 + \frac{\gamma - 1}{2\gamma RT_0} \cdot \left(\frac{\pi}{30} n_{cr}\right)^2 \left(r_{out}^2 - r_{in,avg}^2\right)\right]^{\frac{\gamma}{\gamma - 1}} \tag{4.25}$$

Where:

- $\dot{m}$ is the mass flow rate

- r is the radius of the section

- n_{cr} is the compressor corrected rotational speed

- T is the temperature

- R and γ are the gas constant and the ratio of specific heats

The challenges found in the modeling of the speed at the impeller outlet affected the loss calibration process. When mass flow rate approaches zero, the recirculation loss increases exponentially due to dependence of this term on the flow direction (α_2), which becomes extremely tangential. The same challenge is present in the diffuser friction losses and justifies the change to instead use Equation (4.24).

In summary, both the correlations for energy losses and the angular momentum loss terms must be implemented in a simplified one-dimensional model in order to accurately calculate the trend of the tangential speed when mass flow rate approaches zero.

The steady-state characteristic cannot be calculated using the same equations for both positive and negative mass flow rate, given that the fluid dynamics change drastically when the flow crosses the compressor in the opposite direction than the design direction. For the simulation of deep surge conditions, the steady state characteristic was extended to the negative mass flow rate region of the compressor map using a polynomial curve. The extension is represented by a third order polynomial curve characterized by a minimum pressure ratio for a zero mass flow rate (corresponding to the value calculated by Equation (4.25)) and the maximum corresponding to the maximum calculated by the steady-state model.

4.2 Dynamic Model

The dynamic model describe in this chapter is an adaptation of the distributed parameter model developed by Stockar in [83], [84] and [85]. The model developed by Stockar was adapted to the experimental set-up and the equations for the compressor and plenum were developed and integrated into the model of the pipe system surrounding the compressor and plenum. Stockar's one-dimensional physics-based model for compressible flows is based and the conservation equations of mass (4.26), momentum (4.27) and energy (4.28) and is referred to as an infinitesimal section of the system, Fig. 4.17.

$$\frac{\partial(\rho A)}{\partial t} + \frac{\partial(\rho u A)}{\partial x} = 0 \tag{4.26}$$

$$\frac{\partial(\rho u A)}{\partial t} + \frac{\partial(p A + \rho u^2 A)}{\partial x} + \rho G A = 0 \tag{4.27}$$

$$\frac{\partial(\rho e_0 A)}{\partial t} + \frac{\partial(\rho u h_0 A)}{\partial x} - \rho \dot{q} = 0 \tag{4.28}$$

Where $\rho = \rho(x, t)$, $u = u(x, t)$, $p = p(x, t)$, $e_0 = e_0(x, t)$ and $h = h_0(x, t)$ are respectively local flow density, velocity, pressure, stagnation internal energy and stagnation enthalpy.
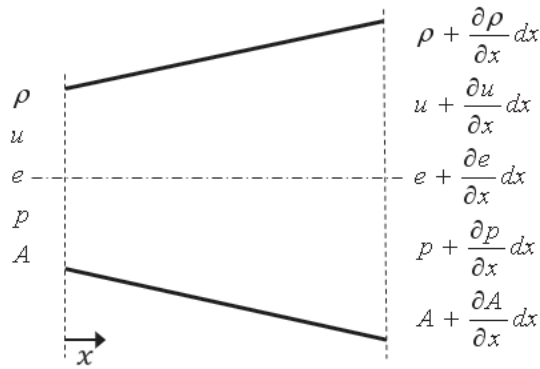
Fig. 4.17 – Schematic of the 1D Control Volume [83]

The simplification of the conservation of mass, energy and three-dimensional momentum and thermodynamic state equation for the fluid is possible by introducing three assumptions.

- the working fluid is considered as a non-reacting ideal gas

- the control volume has fixed walls (no work is exchanged between the walls and the fluid)

- the transformations are irreversible and non-adiabatic due to friction and heat transfer between the fluid and the walls.

The friction and heat loss terms represented by G, the friction force per unit area and the $\dot{q}$, the rate of heat exchange per unit mass, are calculated using Equations (4.29) and (4.30).

$$G(x,t) = \frac{1}{2}|u(x,t)| \cdot u(x,t)f\frac{4}{D} \tag{4.29}$$

Where f is the Moody friction factor and D is the hydraulic diameter relative to the cross section. Equation (4.29) takes into account the possible flow reversal.

$$\dot{q}(x,t) = -\frac{4h_c}{\rho D}(T(x,t) - T_w) \tag{4.30}$$

Where h_c is the convective heat transfer coefficient and T_w is the temperature of the pipe wall. The radiation and conductive heat transfer can be neglected since the tested temperature values are low and the flow is moving. Equations (4.26), (4.27) and (4.28) were manipulated using equations for the mass flow rate, internal energy, enthalpy and the ideal gas law, listed in Equations (4.31), (4.32), (4.33) and (4.34).

$$\dot{m} = \rho Au \tag{4.31}$$

$$e_0 = e + \frac{u^2}{2} = c_v T + \frac{u^2}{2} \tag{4.32}$$

$$p = \rho RT \tag{4.33}$$

$$h_0 = e_0 + \frac{p}{\rho} \tag{4.34}$$

76

The result of the manipulation is shown in matrix form in Equation (4.35).

$$A\frac{\partial W(x,t)}{\partial t} + \frac{\partial F(W)}{\partial x} + B(W) = 0 \tag{4.35}$$

Where W represent the state matrix, F the flux matrix and B the source matrix; these matrices are defined in Equations (4.36), (4.37) and (4.38).

$$W(x,t) = \begin{bmatrix} \rho \\ \dot{m} \\ \rho e_0 \end{bmatrix} \tag{4.36}$$

$$F(W) = \begin{bmatrix} \dot{m} \\ (\gamma - 1)A^2\rho e_0 - \dfrac{\gamma - 3}{2}\dfrac{\dot{m}^2}{\rho} \\ \gamma \cdot \dfrac{\dot{m}}{\rho} \cdot \rho e_0 + \dfrac{\gamma - 1}{2A^2} \cdot \dfrac{\dot{m}^3}{\rho^2} \end{bmatrix} \tag{4.37}$$

$$B(W) = \begin{bmatrix} 0 \\ \dfrac{|\dot{m}|\dot{m}}{\rho} f \sqrt{\dfrac{\pi}{A}} \\ -2h_c\sqrt{\pi A}\left[T_w - \dfrac{\gamma - 1}{R}\left(e_0 - \dfrac{\dot{m}^2}{2\rho^2 A^2}\right)\right] \end{bmatrix} \tag{4.38}$$

The computational domain chosen for the solution of the partial differential equations is shown in Fig. 4.18. The domain consists of a staggered grid; a scheme that can capture and propagate the signal along the whole computational domain.
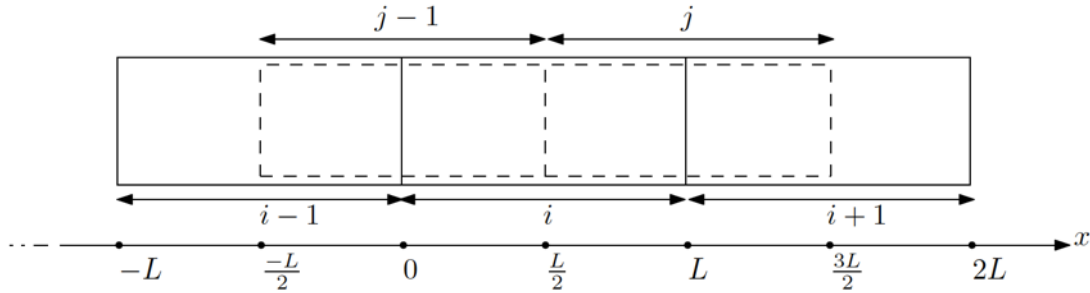
Fig. 4.18 – Schematic Representation of a Staggered Grid [83]

The conservation of mass and conservation of energy equations are applied to the control volume i, while the three-dimensional conservation of momentum equation is applied to the staggered control volume j. Equations (4.36) are then integrated over a constant area control volume. Equation (4.39) is obtained by applying the divergence system to the second term of Equations (4.36).

77

$$\int_{cell} \left[A \frac{\partial W(x,t)}{\partial t} \right] dx + \int_{cell} \left[A \frac{\partial F(W)}{\partial x} \right] dx + \int_{cell} B(W) dx$$

$$= 0 \rightarrow \int_{cell} \left[A \frac{\partial W(x,t)}{\partial t} \right] dx + F(W)|_{bounds} + \int_{cell} B(W) dx = 0$$

(4.39)

Equation (4.39) was converted into an ordinary differential equation by projecting it onto the spatial basis functions shown in Equation (4.40):

$$W(x,t) = \begin{bmatrix} \sum_k \alpha_k(t) \cdot \varphi_k(x) \\ \sum_k \beta_k(t) \cdot \chi_k(x) \\ \sum_k \delta_k(t) \cdot \psi_{k(x)} \end{bmatrix} = \begin{bmatrix} \vec{\alpha}(t) \cdot \vec{\varphi}(x) \\ \vec{\beta}(t) \cdot \vec{\chi}(x) \\ \vec{\delta}(t) \cdot \vec{\psi}(x) \end{bmatrix}$$

(4.40)

Equations (4.41), (4.42) and (4.43) were obtained considering a polynomial basis function $(\vec{\varphi}(x), \vec{\chi}(x), \vec{\psi}(x) = x^{k-1})$ and assuming the states of the system constant inside the control volume (k=1), described in Equation (4.44), (4.45) and (4.46).

$$AL \frac{d\rho_i^*(t)}{dt} = \dot{m}_{j-1}(t) - \dot{m}_j(t)$$

(4.41)

$$AL \frac{d\dot{m}_j^*(t)}{dt} = (\gamma - 1)A^2 \rho_i^*(t)(\rho e_0)_i^*(t) - (\gamma - 1)A^2 \rho_{i+1}^*(t)(\rho e_0)_{i+1}^*(t)$$
$$+ \frac{\gamma - 3}{2} \frac{\dot{m}_j^{*2}(t)}{\rho_{i+1}^*(t)} - \frac{\gamma - 3}{2} \frac{\dot{m}_{j-1}^{*~2}(t)}{\rho_i^*(t)}$$

(4.42)

$$AL \frac{d(\rho e_0)_i^*(t)}{dt} = \gamma \dot{m}_j^*(t)(\rho e_0)_i^*(t) - \gamma \dot{m}_{j-1}^*(t)(\rho e_0)_{i-1}^*(t)$$
$$+ \frac{1 - \gamma}{2A^2} \frac{\dot{m}_j^{*3}(t)}{\rho_i^{*2}(t)} - \frac{1 - \gamma}{2A^2} \frac{\dot{m}_{j-1}^{*~3}(t)}{\rho_{i-1}^{*~2}(t)}$$

(4.43)

Where the states with asterisks represent the constant value over the control volume. The complete derivation of the equations is described in [86].

$$\rho_i^*(t) = \alpha_1(t) \cdot \frac{1}{V} \int_0^L [A \cdot \varphi_1(x)] dx = \alpha_{1,i}(t)$$

(4.44)

$$\dot{m}_j^*(t) = \beta_1(t) \cdot \frac{1}{V} \int_{0.5L}^{1.5L} [A \cdot \chi_1(x)] dx = \beta_{1,j}(t)$$

(4.45)

$$(\rho e_0)_i^*(t) = \delta_1(t) \cdot \frac{1}{V} \int_0^L [A \cdot \psi_1(x)] dx = \delta_{1,i}(t)$$

(4.46)

The complexity of the experimental set-up that had to be modeled required a variety of different model components. In each of these components, certain equations had to be modified to

represent the behavior associated to the respective component. These components with unique models include open end pipes, the compressor, the plenum and the valve.

4.2.1 Open-End Pipe

For open-end pipes, see Fig. 4.19, two different transformations were applied depending on the direction of the fluid.
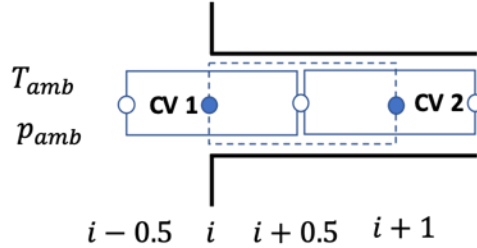
Fig. 4.19 – Open End Pipe Schematic Representation

For pipe inflow, the transformation is considered isentropic. The modification to the model consisted of substituting the momentum equation with Equation (4.47) and calculating mass flow rate, temperature and density with Equations (4.48), (4.49), and (4.50).

$$\dot{m}_2 = \frac{Ap_{t1}}{\sqrt{RT_{t1}}} \sqrt{\frac{2}{\gamma - 1}} \sqrt{\left(\frac{p_2}{p_{t1}}\right)^{\frac{2}{\gamma}} - \left(\frac{p_2}{p_{t1}}\right)^{\frac{\gamma+1}{\gamma}}} \tag{4.47}$$

$$\rho_1 A u_1 = \rho_2 A u_2 \tag{4.48}$$

$$\rho_2 = \rho_{t1} \left(\frac{p_2}{p_{t1}}\right)^{\frac{1}{\gamma}} \tag{4.49}$$

$$T_2 = \frac{p_2}{\rho_2 R} \tag{4.50}$$

Where:

- $\dot{m}$ is the mass flow rate
- ρ and ρ_t are the density and total density
- A is the area of the section
- p and p_t are the static and total pressure
- T and T_t are the static and total temperature
- u is the flow speed
- γ and R are the ratio of specific heats and the gas constant

For pipe outflow, the transformation occurs at constant pressure. The energy equation is written as the equality between stagnation enthalpies in 2 and 3, Equation (4.51). By combining the

mass conservation equation, the ideal gas law and the assumption of an isobaric transformation density, the speed and temperature can be calculated, see Equations (4.52), (4.53) and (4.54).

$$h_{t2} = h_{t3} \Rightarrow c_p T_2 + \frac{u_2^2}{2} = c_p T_3 + \frac{u_3^2}{2} \tag{4.51}$$

$$p_2 = p_1 \tag{4.52}$$

$$\rho_2 = \frac{p_2}{T_2 R} = \frac{p_1}{T_2 R} \tag{4.53}$$

$$\rho_3 A u_3 = \rho_2 A u_2 \Rightarrow u_2 = \frac{\dot{m}_2}{\rho_2 A} = \frac{\dot{m}_3}{\rho_2 A} = \frac{\dot{m}_2}{p_1 A} R T_2 \tag{4.54}$$

Where:

- $\dot{m}$ is the mass flow rate

- ρ is the density

- A is the area of the section

- p and T is the static pressure and temperature

- h_t is the total enthalpy

- u is the flow speed

- γ and c_p are the ratio of specific heats and the specific heat at constant pressure

For the open-end pipe located at the outlet of the pipe system, the same approach was followed with the only difference being the opposite sign of the mass flow rate. The equations remained the same in all other terms.

4.2.2 Compressor

The compressor was modeled as two different control volumes. The density and energy states of the two control volumes correspond to the compressor inlet and outlet conditions. The mass flow rate evolving through the compressor is represented by the mass flow rate state of the control volume in the staggered grid, as shown in Fig. 4.20.
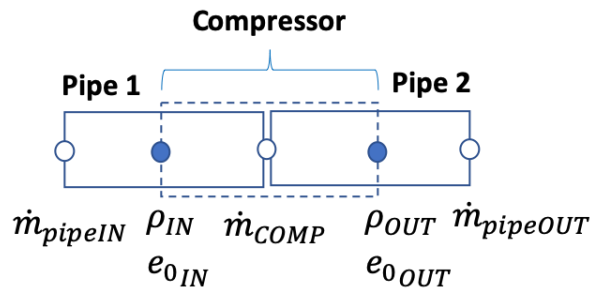
Fig. 4.20 – Compressor Schematic Representation

The mass conservation equation structure was not modified, see Equations (4.55) and (4.56). The length of each control volume is a function of the characteristic length of the compressor and does not correspond to a physical dimension.

$$\frac{dA_{IN} \cdot \rho_{IN}}{dt} = \frac{F_{density}^{IN} - F_{density}^{OUT}}{L_1} = \frac{\dot{m}_{pipeIN} - \dot{m}_{COMP}}{L_1} \tag{4.55}$$

$$\frac{dA_{OUT}\rho_{OUT}}{dt} = \frac{F_{density}^{IN} - F_{density}^{OUT}}{L_2} = \frac{\dot{m}_{COMP} - \dot{m}_{pipeOUT}}{L_2} \tag{4.56}$$

Where:

- $\dot{m}$ is the mass flow rate

- A and L are the area of the section the length of the control volume

- p_u and p_d are the upstream and downstream pressure

- ρ and F are the density and the flux

The momentum equation for the compressor is substituted with equation taken from Gravdahl's work [42], where the compressor characteristic pressure p_{char} was calculated with the steady state compressor model, described in chapter 4.1, Steady-State Characteristic Model.

$$\frac{d\dot{m}_{COMP}}{dt} = \frac{A_{IN}}{L_c}(p_{char} - p_{out}) \tag{4.57}$$

Where L_c is the characteristic length of the compressor. To account for the energy increase during the compression, the energy conservation equation in the second control volume was modified, see Equation (4.58).

$$\frac{d\rho_{OUT} \cdot A_{out} \cdot e_{0_{OUT}}}{dt} = \frac{F_{energy}^{in} - F_{energy}^{out} + \Delta F_{energy,comp}}{L_c} = \frac{F_{energy}^{char} - F_{energy}^{out}}{L_c} \tag{4.58}$$

Where the flux terms are defined by Equations (4.59) and (4.60), which derive from the general form expressed in Equation (4.37).

$$F_{energy}^{out} = \gamma \dot{m}_{2.5} e_{0,2.5} + \frac{(1-\gamma)\dot{m}_{2.5}^3}{\rho_{2.5}^2 A_{2.5}^2} \tag{4.59}$$

$$F_{energy}^{char} = \gamma \dot{m}_{comp} c_v T_{t,char} + \frac{(1-\gamma)\dot{m}_{comp}^3}{\rho_2^2 A_2^2} \tag{4.60}$$

The stagnation temperature is also derived from the steady state model described in chapter 4.1, Steady-State Characteristic Model. For negative mass flow rate conditions, the value of the stagnation temperature was maintained constant and equal to the minimum value calculated by the steady-state compressor model.

4.2.3 Volumes and Plenums

The plenum is represented by one control volume shown in Fig. 4.21. The equations of the mass flow rate entering the plenum i-0.5 and the mass flow rate in volume i-1 were modified to account for the plenum boundary condition and the pipe section variation.
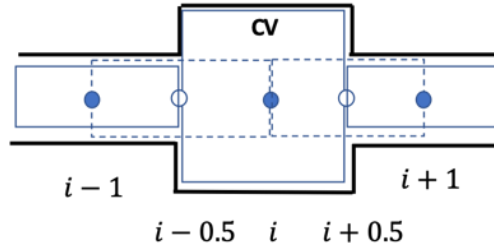
Fig. 4.21 – Plenum Schematic Representation

For the calculation of the temperature and pressure in the plenum the energy equation is substituted with an equation that is directly a function of the temperature, see Equation (4.61), and the momentum is calculated with Equation (4.62).

$$\frac{\partial T_p}{\partial t} = \frac{1}{mc_v}[\dot{m}_{in}c_pT_{in} - \dot{m}_{out}c_pT_{out} - c_vT_p(\dot{m}_{in} - \dot{m}_{out})] \tag{4.61}$$

$$\dot{m}_{i\pm0.5} = sign(p_{IN} - p_{OUT})\sqrt{2\rho_{IN}A_{IN}|p_{IN} - p_{OUT}|} \tag{4.62}$$

Where:

- $\dot{m}$ and m are the mass flow rate and the mass of air in the plenum
- A is the area of the section
- p, T and ρ is the static pressure, temperature and density
- c_v and c_p are the specific heats at constant volume and at constant pressure

Where inlet and outlet conditions in Equation (4.62) depend on the direction of the flow which is function of the pressure difference across the plenum.

4.2.4 Valves and Orifices

In the valve representation shown in Fig. 4.22, the valve is located across two different control volumes and corresponds to one control volume of the staggered grid with center i+0.5. Control volumes following control volume i in Fig. 4.22 are not modified while the isentropic orifice equation, Equation (4.63), is introduced to calculate mass flow rate at i+0.5, inside the valve.
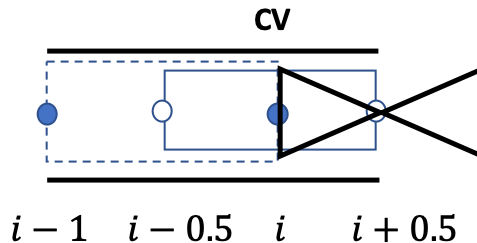
Fig. 4.22 – Valve Schematic Representation

$$\begin{cases} \dot{m}_v = C_d A \dfrac{p_u}{\sqrt{RT_u}} \sqrt{\dfrac{2}{\gamma-1}} \sqrt{\left(\dfrac{p_d}{p_u}\right)^{\frac{2}{\gamma}} - \left(\dfrac{p_d}{p_u}\right)^{\frac{\gamma+1}{\gamma}}} & if \; p_d \geq p_{cr} \\[4ex] \dot{m}_v = C_d A \dfrac{p_u}{\sqrt{RT_u}} \sqrt{\left(\dfrac{2}{\gamma+1}\right)^{\frac{\gamma+1}{\gamma-1}}} & if \; p_d < p_{cr} \end{cases}$$

(4.63)

Where:

- $\dot{m}$ is the mass flow rate

- A and C_d are the area of the section and the discharge coefficient

- p and T are the static pressure and temperature

- p_u and p_d are the upstream and downstream pressure

- γ and R are ratio of the specific heats and the gas constant

Where the critical pressure and the discharge coefficient are defined in Equation (4.64). The discharge coefficient represents the ratio between the actual and ideal mass flow rate and is a function of the throttle position, see Equation (4.65):

$$p_{cr} = p_u \left(\frac{2}{\gamma+1}\right)^{\frac{\gamma}{\gamma-1}}$$

(4.64)

$$C_d = \frac{\dot{m}_{actual}}{\dot{m}_{ideal}}$$

(4.65)

5 Experimental and Modeling Results

The results collected during this work are discussed in this chapter. At first, the results of the first experimental investigation are shown and analyzed. This first set of results provided valuable insight into how the surge phenomena must be modeled. The model development aimed to predict compressor and pipe behavior in stable and unstable behavior while also capturing the phenomena occurring close to the stability limit. The phenomena are highlighted in the first section of this chapter. The analysis of the data collected during the second experimental investigation follows the first experimental investigation results. The final part of this chapter consists of the model calibration, validation and simulation results.

5.1 First Experimental Investigation

The results of the first experimental investigation are presented in two analyses. The first is a thermo-fluid dynamic analysis and the second a vibro-acoustic analysis. The first analysis concentrates on the low frequency components of signals captured by pressure sensors, while the second on the medium and high frequency components captured by the accelerometers.

5.1.1 Thermo-Fluid Dynamic Results

The compressor steady-state characteristic curves were analyzed to verify the measurements matched data previously collected during stable operating conditions. The experimental steady-state curves were compared to results previously obtained by the manufacturer and in previous research developed at DIME. The steady-state characteristic is referred to groups of parameters that take into account the effect of the inlet conditions and preserve the Mach similarity. The groups are reported in Equations (5.1), (5.2) and (5.3).

- Corrected rotational speed [rpm]:

$$n_{cr} = \frac{n \cdot \sqrt{T_0}}{\sqrt{T_{T1}}} \tag{5.1}$$

- Total to total compression ratio [-]:

$$\beta_{cTT} = \frac{p_{T2}}{p_{T1}} \tag{5.2}$$

- Corrected mass flow rate [kg/s]:

$$M_{cr} = \frac{M_c \cdot p_0 \cdot \sqrt{T_{T1}}}{p_{T1} \cdot \sqrt{T_0}} \tag{5.3}$$

where:

- n is the turbocharger rotational speed
- T_0 is the reference temperature (equal to 293.15 K)
- T_{T1} is the compressor inlet total temperature
- p_{T1} is the compressor inlet total pressure
- p_{T2} is the compressor outlet total pressure

- M_c is the compressor mass flow rate

- p_0 is the reference pressure (equal to 0.981 bar)

The compressor pressure ratio plotted versus corrected mass flow rate curves for different outlet pipe lengths with an 8-liter plenum are shown in Fig. 5.1 and the curves with a 12-liter plenum are shown in Fig. 5.2. The steady flow characteristics are very similar for all eight circuit configurations. There is a slight difference in the extension of measured curves in the choking region due to the lower pressure losses associated with the reduced lengths of downstream pipes.
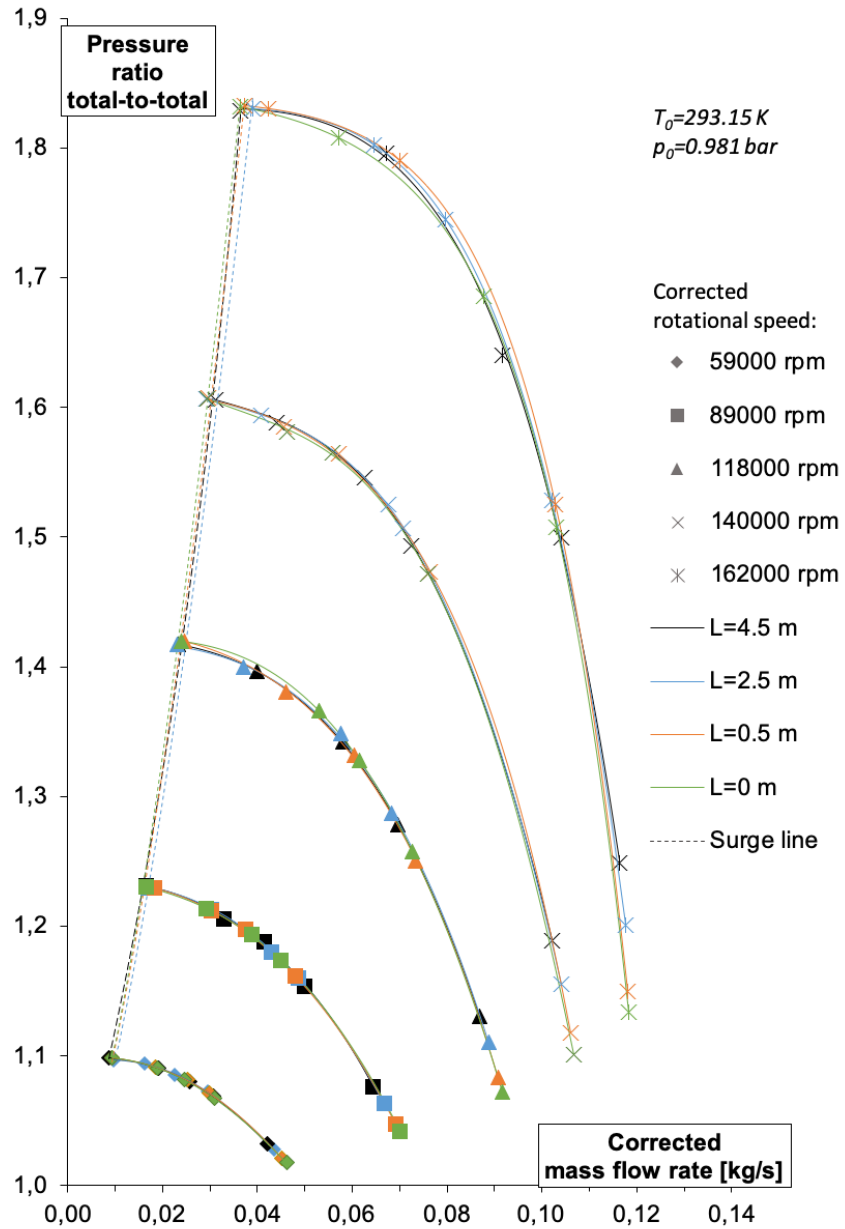
Fig. 5.1 – Comparison of Compressor Steady State Characteristic at Different Length and Constant Plenum Volume (8 Liters)
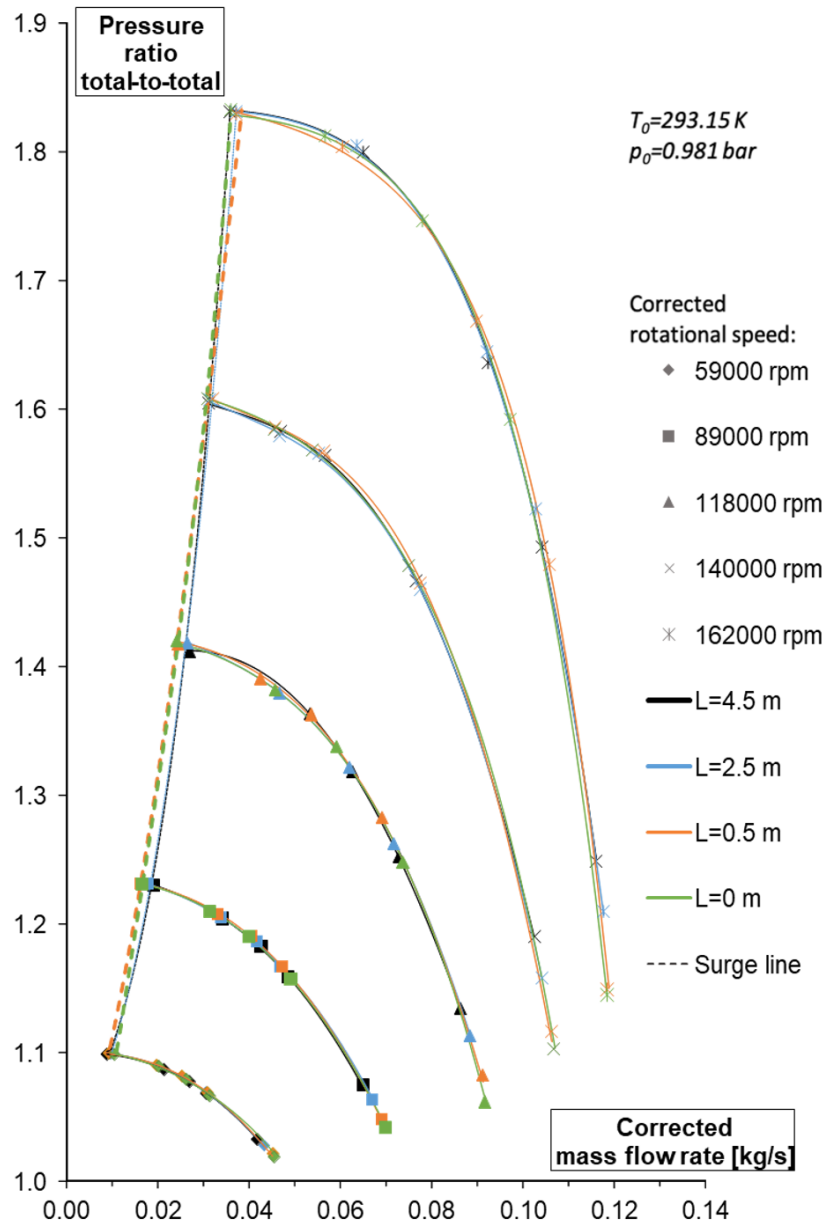
Fig. 5.2 – Comparison of Compressor Steady State Characteristic at Different Length and Constant Plenum Volume (12 Liters)

The amplitude of the fundamental frequency increases with rotational speed for all values of length and volume due to the inertial effects of the higher mass crossing the compressor. For the minimum circuit length (L = 0 m) the frequency spectra at different velocities show the fundamental harmonic associated to the pressure oscillations induced by surge, see Fig. 5.3 and Fig. 5.4. As the length of the circuit increases, the relative amplitude of the fundamental harmonic decreases and other harmonics at higher frequencies appear (not necessarily multiples of the fundamental). This effect is related to the wave propagation phenomena in the delivery

circuit, which introduces nonlinear effects on the frequency spectrum of the compressor outlet pressure due to the coupling of the boundary conditions. This is confirmed by the similar spectra associated to the same circuit length.
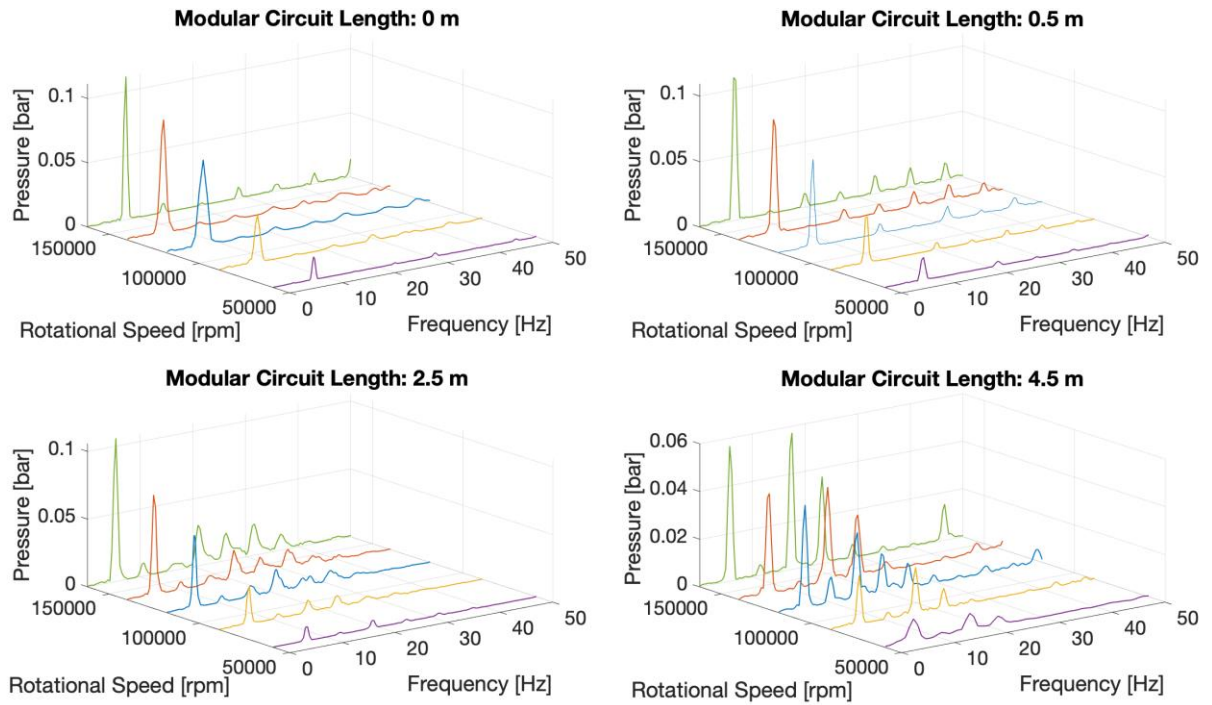
Fig. 5.3 – Comparison of Compressor Outlet Pressure Spectra in Surge Conditions for Different Circuits Lengths at Fixed Plenum Volume (8 Liters)
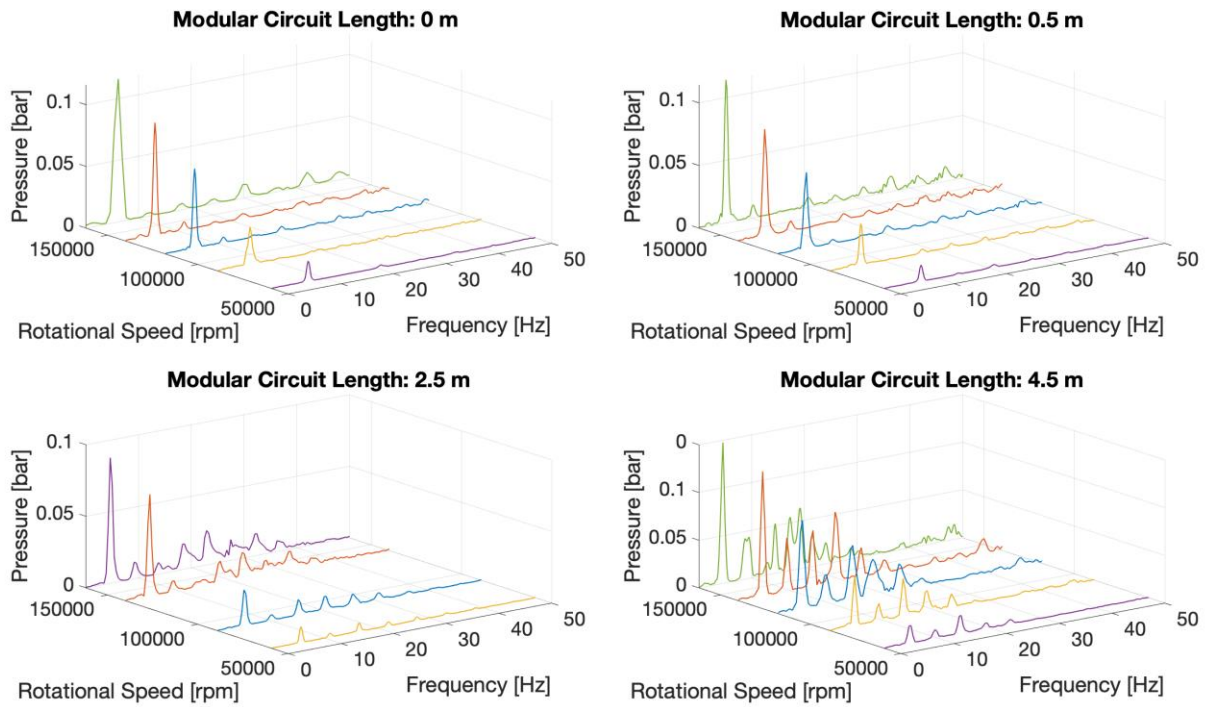
Fig. 5.4 – Comparison of Compressor Outlet Pressure Spectra in Surge Conditions for Different Circuits Lengths at Fixed Plenum Volume (12 Liters)

The frequency and amplitude associated to the fundamental harmonic of the compressor outlet pressure under unstable operation were extracted and listed in Tab. 5.1 and Tab. 5.2. The amplitude of the surge-related harmonics increases with the turbocharger rotational speed and decreases with the circuit length. The trend with respect to the circuit length could be due to the damping effect on the pressure oscillations due to friction and heat transfer, or to the increased wave action in the circuit observed for longer-length configurations. The increase in amplitude of the fundamental harmonic with plenum volume is likely attributed to the inertial effects of the increased mass filling the plenum.

		Plenum Volume	Circuit Modular Length			
			0 m	0.5 m	2.5 m	4.5 m
Rotational Speed	59000 rpm	8 l	0.0178	0.0174	0.0103	0.00960
		12 l	0.0165	0.0131	0.0111	0.00738
	89000 rpm	8 l	0.0369	0.0352	0.0278	0.0206
		12 l	0.0304	0.0331	0.0250	0.0211
	118000 rpm	8 l	0.0670	0.0664	0.0534	0.0430
		12 l	0.0645	0.0607	-	0.0372
	140000 rpm	8 l	0.0884	0.0871	0.0737	0.0421
		12 l	0.0914	0.0853	0.0711	0.0523
	162000 rpm	8 l	0.1114	0.1092	0.1057	0.0566
		12 l	0.116	0.114	0.0877	0.0590

Tab. 5.1 – Amplitude of Surge Fundamental Harmonic in bar

The trends seen in the fundamental frequency of pressure signals measured in surge operation are consistent with the definition of Helmoltz frequency [14], [15], [16].

$$f_H = \frac{a}{2\pi} \sqrt{\frac{A}{V L_t}} \qquad (5.4)$$

where:

- a is the speed of sound
- A is the section of the pipe
- V is the volume of the plenum
- L_t is the total length of the pipe

The fundamental frequency decreases as the length of the pipe or the volume of the plenum increase. An opposite effect was observed on the turbocharger shaft speed where an increase in rotational speed correlated to a decrease in fundamental frequency.

		Plenum Volume	Circuit Modular Length			
			0 m	0.5 m	2.5 m	4.5 m
Rotational Speed	59000 rpm	8 l	7.63	7.25	6.49	5.34
		12 l	6.87	6.87	5.53	4.96
	89000 rpm	8 l	7.25	6.87	5.72	5.34
		12 l	6.10	5.72	4.96	4.58
	118000 rpm	8 l	6.87	6.49	5.15	4.96
		12 l	5.53	5.34	-	4.58
	140000 rpm	8 l	6.87	6.49	4.96	5.72
		12 l	5.53	4.96	4.58	4.58
	162000 rpm	8 l	7.25	6.49	5.34	5.72
		12 l	6.10	5.15	4.58	4.58

Tab. 5.2 – Frequency of Surge Fundamental Harmonic in Hertz

The phenomena leading to the inception of surge was then investigated. Instantaneous signals of compressor outlet pressure and turbocharger rotational speed were measured under stable and unstable operations to analyze the relevant frequency spectra.

First, the compressor stable operating points were considered to determine how the frequency spectra changed when moving towards the surge region. The test was performed for all compressor rotational speeds and outlet circuit configurations previously discussed for the first experimental investigation.

Fig. 5.5, Fig. 5.6 and Fig. 5.7 show the low frequency spectra (0-50 Hz) of the compressor outlet pressure measured for three rotational speeds and three different circuit lengths. Four stable operating points are reported in each diagram, referred to as a "Run", and represent points closer to the surge line as the run number increases. Run 5 is considered the last stable point before entering the unstable region.
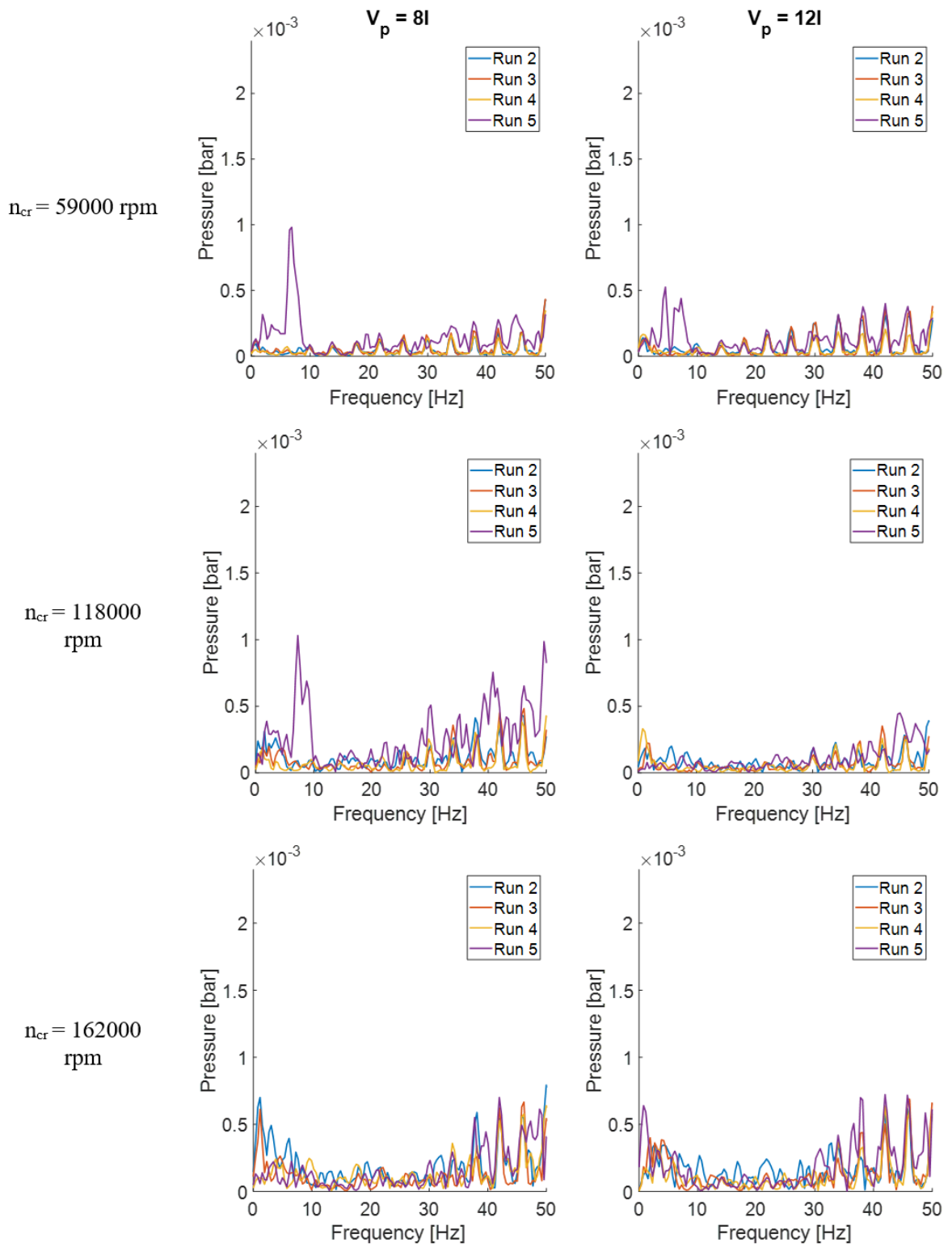
Fig. 5.5 – Compressor Outlet Pressure Spectra Measured in Four Stable Operating Points (Modular Circuit Length: 0.5 m)
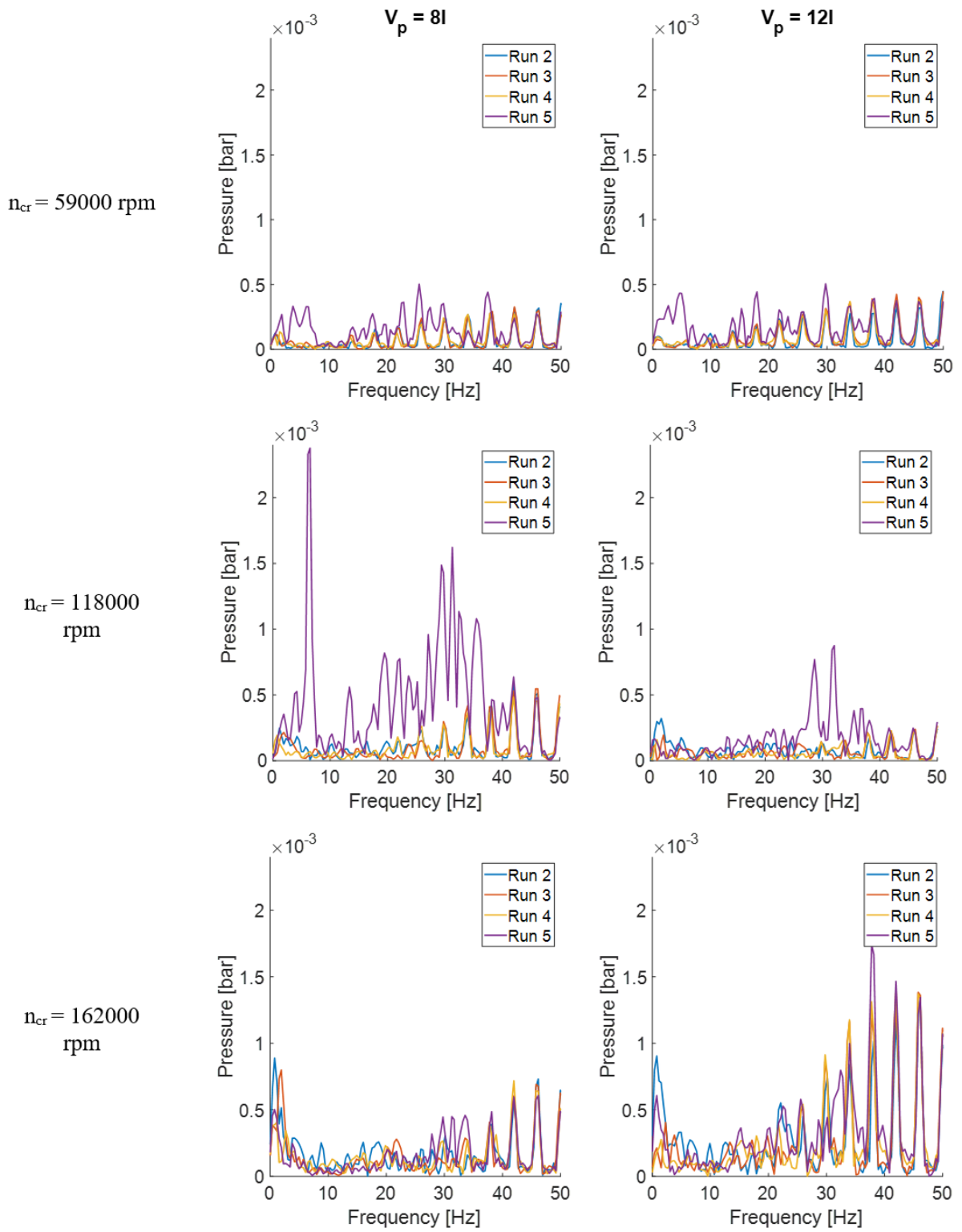
Fig. 5.6 – Compressor Outlet Pressure Spectra Measured in Four Stable Operating Points (Modular Circuit Length: 2.5 m)
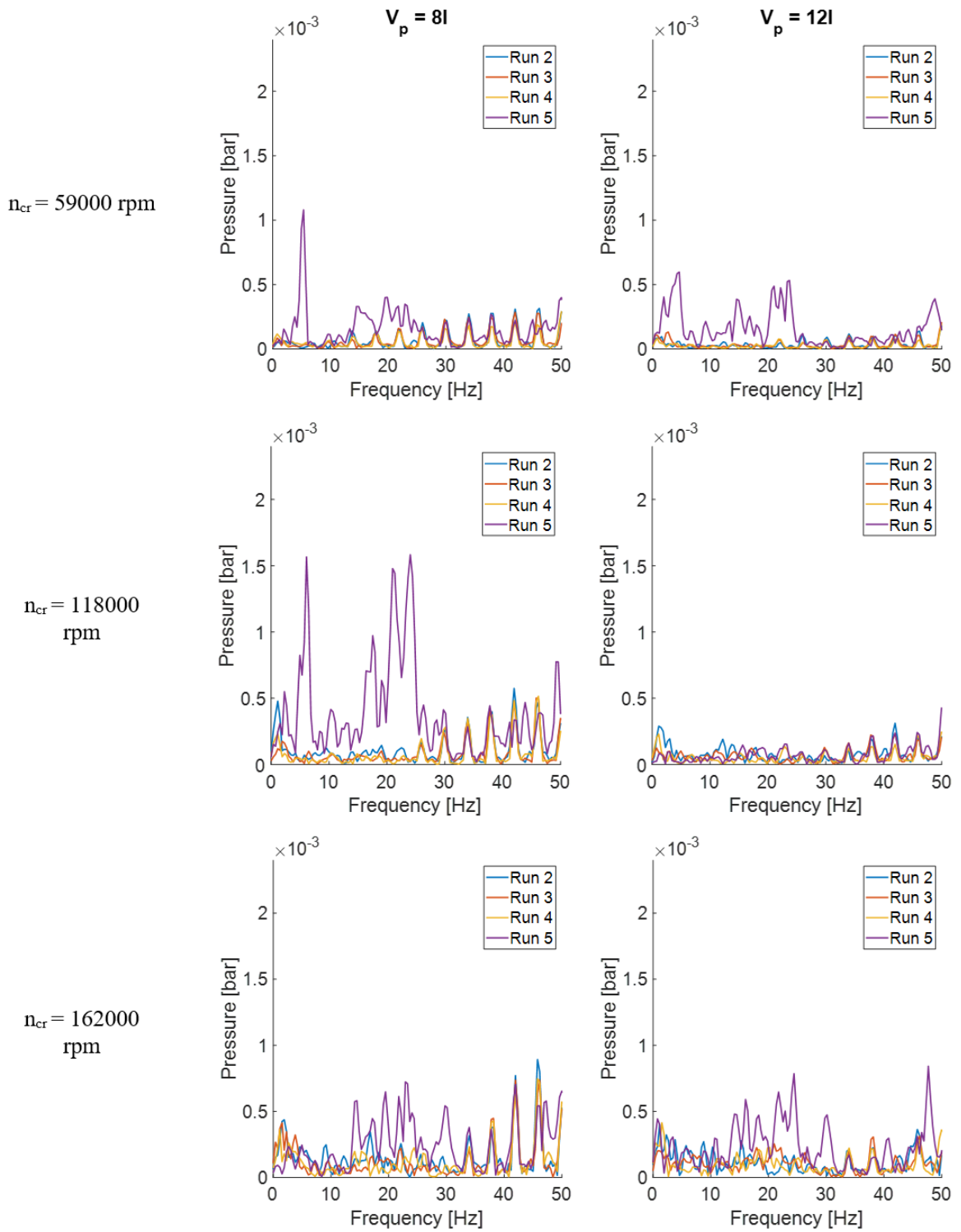
Fig. 5.7 – Compressor Outlet Pressure Spectra Measured in Four Stable Operating Points (Modular Circuit Length: 4.5 m)

Small amplitude oscillations at different frequencies are present in all stable points in the considered range. However, it is possible to observe that in the last stable point the amplitude of low frequency components is greater than the other stable points. This impact is greater for the low and intermediate rotational speed conditions and for lower values of circuit volume but is not noticeable at the highest rotational speeds. This phenomenon was observed in all the analyzed configurations, as shown in Fig. 5.5, Fig. 5.6 and Fig. 5.7.

Next, the compressor outlet pressure frequency spectra measured in the last stable point were compared with spectra measured in the corresponding surge point. As shown in Fig. 5.8, the oscillation amplitudes under unstable operation are considerably higher. The surge frequency appears independent of compressor speed while, in the last stable point, the most prominent frequency of the spectrum varies with the rotational speed. These components move towards higher frequencies as the speed increases. Based on the results discussed, it appears that surge operation could be expected if an increase of the amplitude of the compressor outlet pressure spectrum is detected close to the surge frequency.
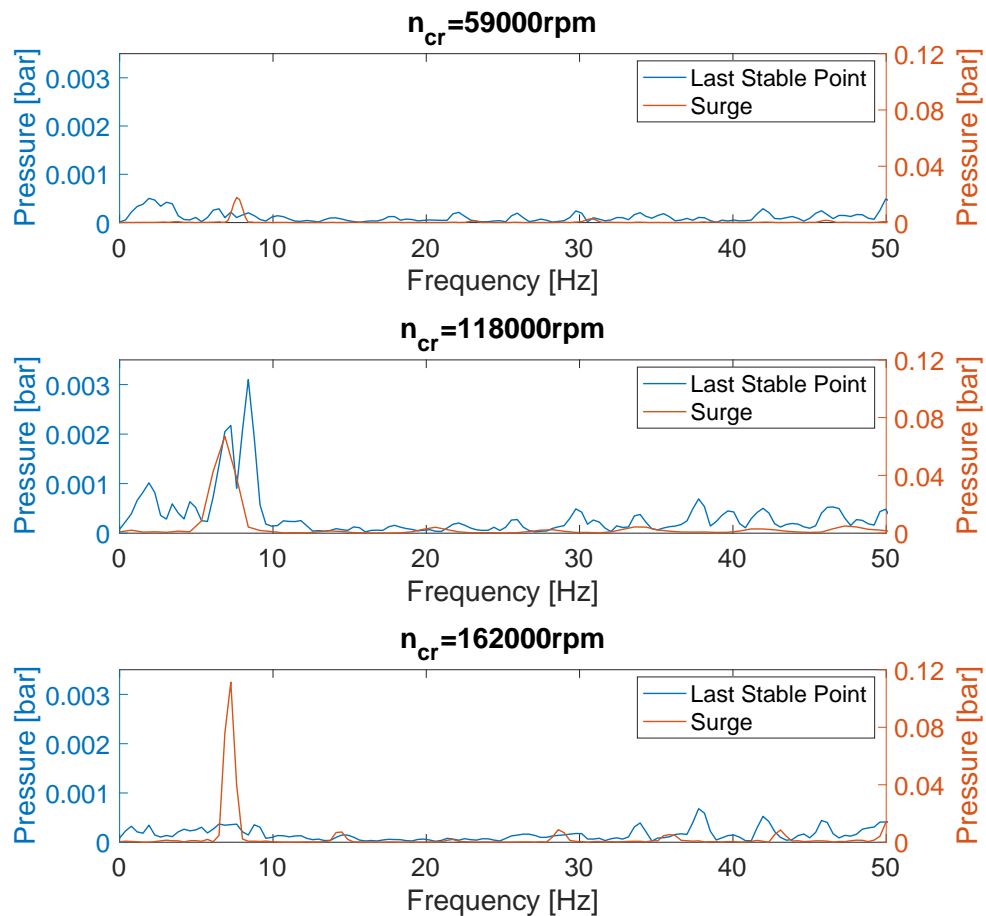
Fig. 5.8 – Comparison of Pressure Spectra in Stable and Surge Conditions for Different Rotational Speed Levels (Modular Circuit Length: 0 m, Plenum Volume: 8 l)

5.1.2 Vibro-Acoustic Results

The vibro-acoustic measurements are not characterized by the same low frequencies as the compressor pressures at the last stable point. The system vibrational behavior was experimentally investigated to obtain a dynamic characterization in stable conditions. For this reason, compressor rotational speed run up tests were carried out. A run up test is used to characterize the natural frequencies of the system: from a starting point corresponding to a compressor operating condition far from the surge line at 32500 rpm, the speed is increased to 171000 rpm. Vibration and acoustic measurements in these conditions identify the frequency components and associate them with the related sources.

A waterfall representation of the compressor housing radial vibration spectra during a run up is shown in Fig. 5.9. The synchronous component 1X (see order cursor 1.0) is related to mass eccentricity in the rotor or shaft. The second order 2X (see order cursor 2.0) is negligible. The sub-synchronous vibration components are significant. Since the considered turbocharger is equipped with floating ring radial bearings, these components are due to whirling or whipping phenomena in the bearings [87], [88]. During turbocharger operation, sub-synchronous vibrations are forced by the hydrodynamic friction of the lubricant against the shaft. Rotational speed of the bearing rings is determined by inner and outer lubricant film resistance forces. In theory, bearing ring rotational speed can reach a value close to 50% of the shaft rotational speed. In reality, this speed is lower because, for a given turbocharger rotational speed, the bearing speed increases proportionally until it reaches an equilibrium point. The first component and the related superior orders are shown in Fig. 5.9. The second component is the most significant: it increases in amplitude as the running speed increases (up to 100000 rpm), then it reaches a saturation level as nonlinearities in the system forbid reaching higher amplitudes [88].
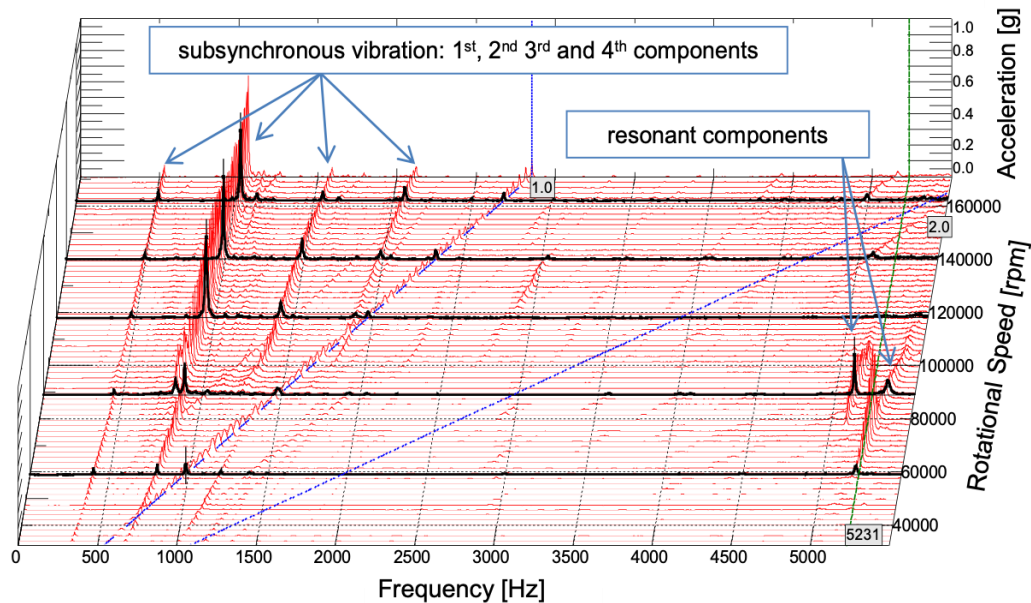
Fig. 5.9 – Waterfall of Compressor Housing Radial Accelerometer Evaluated during Run Up

The auto-power spectrum of the vibration signal on the compressor housing in the radial direction for a compressor rotational speed of 95400 rpm is shown in Fig. 5.10. The blue dashed line shows the 1X component at 1593 Hz, while the black dotted lines show the sub-synchronous components, the component at 437 Hz and the related multiples. In the spectrum, the two green dotted lines show the sidebands at 1156 Hz and 2030 Hz, caused a modulation phenomenon of the 1st sub-synchronous component on the 1X [89]. The peak at 15930 Hz is related to the compressor blade passing frequency and corresponds to order 10X; the blade passing frequency is the product of the rotational frequency time the number of blades, which is ten for the tested compressor. The two blue dotted lines show the modulation phenomenon related to the 1X on the blade passing frequency. The sidebands are a small shift in frequency from the expected values. This is related to complex interactions among different turbocharger dynamic phenomena at this high frequency, which moves spectrum peaks. The black dash-dot lines at 5149 Hz and 5359 Hz show two peaks related to structural resonances. These two frequency peaks are due to the system cylindrical symmetry which often is characterized by vibrational modes with close frequencies. Other sets of two peaks at double frequencies are the 2nd components of the previous sets, related to a non-linear contribution in the system response. These same results are seen in acoustic signals.
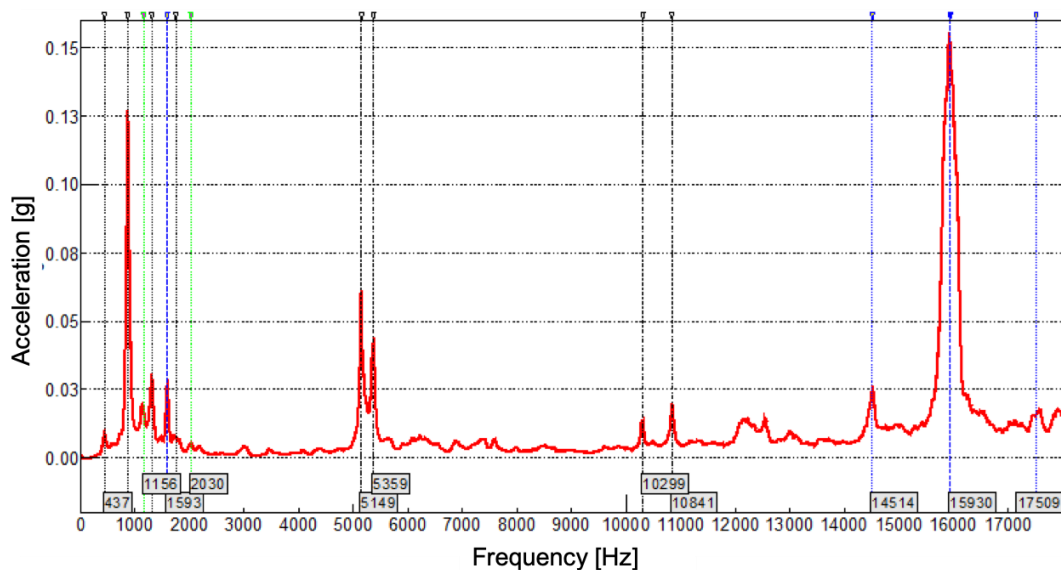
Fig. 5.10 – Compressor Housing Accelerometer (Radial Direction) Auto-Power Spectrum for
n = 95400 rpm

For incipient surge detection, the vibro-acoustic compressor response is analyzed for different values of the throttle valve position considering a fixed compressor rotational speed. This technique allows the analysis of different working points on the compressor map and the observation of the transition from stable operation far from the surge line to stable operation close to the surge line. The signal of the accelerometer mounted at the compressor inlet measuring stations is shown in Fig. 5.11 for Run 1 through 5 at a constant corrected rotational speed of 140000 rpm. The auto-power spectra of these signals are shown in the frequency range below the synchronous component. Run 1 corresponds to fully open throttle valve, while Run 5 to the last stable point on the compressor curve. The blue dashed line indicates the 1X

96

component, which corresponds to 2366 Hz. The amplitude of these signals is lower than the amplitude of the accelerometers located on the compressor casing; since the measuring station where the accelerometer is located is structurally uncoupled from the turbocharger, the intensity of the vibration transferred to the measuring station is lower. The black dotted lines indicate the sub-synchronous components. This figure highlights how the frequency spectrum components change when the mass flow rate through the compressor decreases and the compressor operating condition approaches surge. The vibration content highlighted in the blue oval increases close to surge conditions. A broad-band component appears in the frequency range of 15-20% of the rotational frequency. As described by Fink, this sub-synchronous activity can be associated with the beginning of rotating stall. In this case, the sub-synchronous component can be used to identify surge onset, as is reported in other papers [90], [91] and [92]. Similar results were obtained for different turbocharger rotational speeds and test bench configurations.
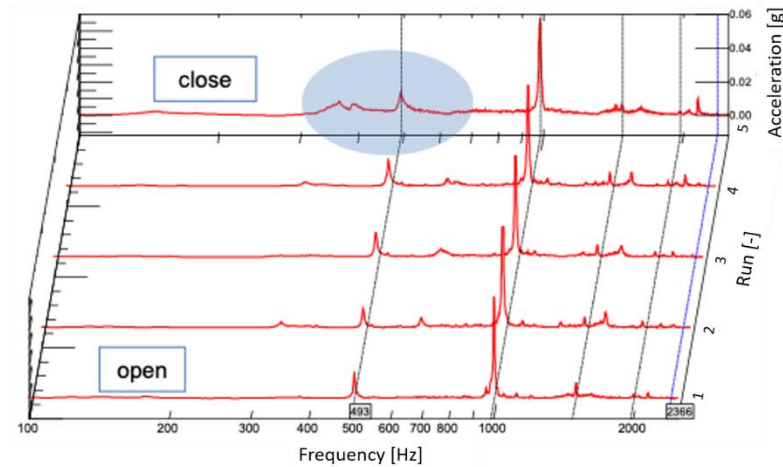
Fig. 5.11 – Compressor Inlet Accelerometer Auto-Power Spectra at n = 14000 rpm

To evaluate the possibility of identifying surge onset from vibration and acoustic data, a filter operation was performed to separate the impeller revolution and the bearing contributions from those related to fluid dynamics phenomena inside the compressor. A band stop filter was used together with the information obtained in the run up analysis, which allowed to set frequencies for the filtering process. This procedure was chosen to consider only sub-synchronous components of the spectrum. This methodology increases the accuracy of surge identification in experimental data. The RMS of the filtered signal is shown in Fig. 5.12; the 1X component measured on the compressor housing of Run 1 through 5 is plotted for five compressor corrected rotational speeds. The filtered RMS value increases when the operating condition approaches the surge line for each turbocharger rotational speed. The magnitude of the filtered RMS values is correlated to the fluid-dynamic modification and distortion in the impeller channel which reflects in a modification of the vibration and acoustic response.

97
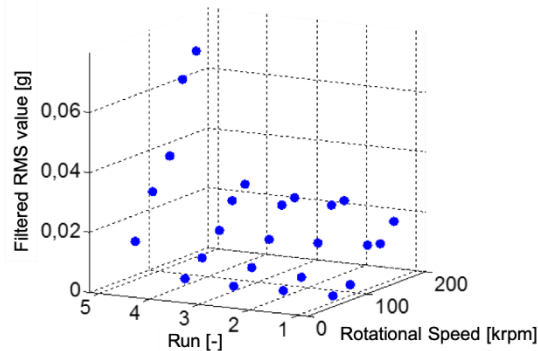
Fig. 5.12 – Filtered RMS Values for 5 Different Compressor Speed Levels from Fully-Open to Almost Fully Closed Throttle Valve

The sub-synchronous components of the vibration spectrum at the compressor inlet for different circuit lengths in a stable condition is compared to the corresponding signal near the surge line, as shown in Fig. 5.13. Frequency spectra in stable conditions are very similar and are not sensitive to circuit length. The behavior is different near the unstable region. In this situation, the circuit geometry has an impact on the shape and amplitude, making the identification of surge easier in certain circuit configurations: specific volumes increase the amplitude of the frequency components used for surge detection. In this specific case, the configurations with higher circuit modular lengths are characterized by a higher amplitude.
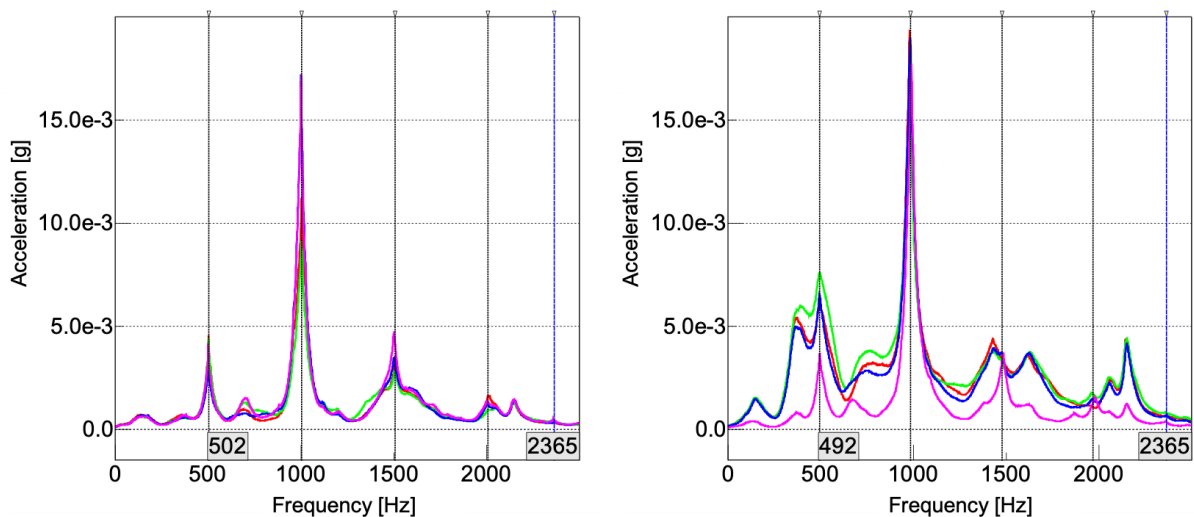
Fig. 5.13 – Compressor Inlet Sub-Synchronous Vibration Spectra for Different Values of Circuit Modular Length in a Stable Condition far from Surge (Left) and near Surge (Right)

The vibrational and acoustic analysis was extended to high frequency values, as shown in Fig. 5.14. The high frequency details of the auto-power spectra measured on the compressor housing in the radial direction at a 140000 rpm are shown in Run 1 (red trace) and at the last stable point (green trace). The frequency peak associated with the blade passing frequency at 23676 Hz becomes less prominent moving from Run 1 to Run 5. Near unstable conditions, the blade passing frequency component loses energy and at the same time new components appear. These

components are related to fluid-dynamic phenomena linked to incipient surge. In Run 5, in addition to the modulation of the blade passing frequency related to turbocharger rotational speed, highlighted in the orange ovals, a second modulation related to sub-synchronous phenomena indicates the approaching of surge, highlighted in the blue oval.
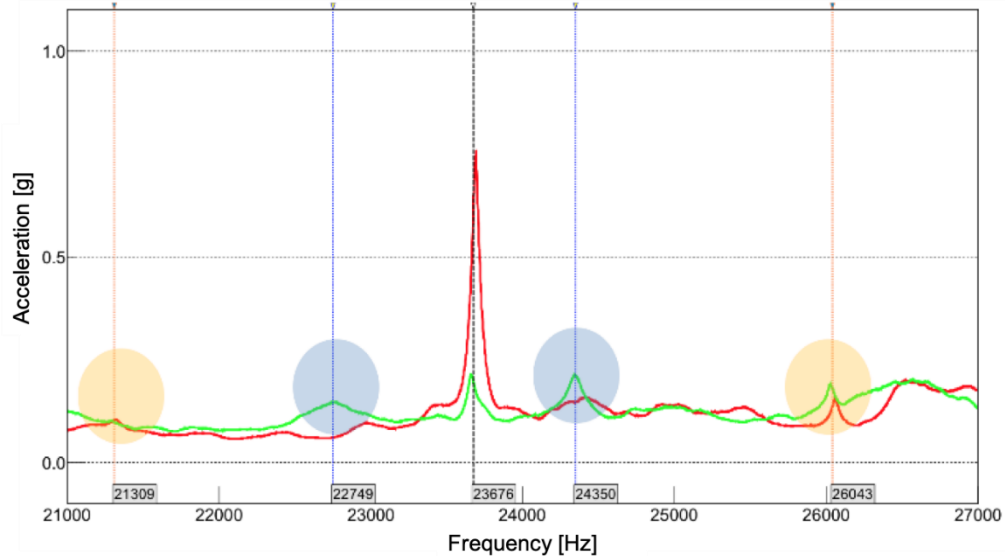
Fig. 5.14 – High Frequency Detail of the Auto-Power Spectra Evaluated on the Compressor Housing

5.2 Second Experimental Investigation

The analysis of the second experimental investigation focused on the shape and position of the surge cycles compared to the compressor steady-state characteristic. The surge cycles were derived by measurements collected during Run 6. The pressure signal measured in the compressor volume is also studied in this section.

To verify the correct execution of the experimental test, the compressor steady-state curves were compared against compressor curves previously measured by DIME. The steady-state characteristics in different configurations are compared in Fig. 5.15 and Fig. 5.16 for two different values of plenum volume, 2 and 6 liters. In steady flow conditions, the surge line position is mildly affected by the length of the circuit and the volume of the plenum. The compressor characteristic curves are plotted against the parameters described in Equations (5.1), (5.2) and (5.3).
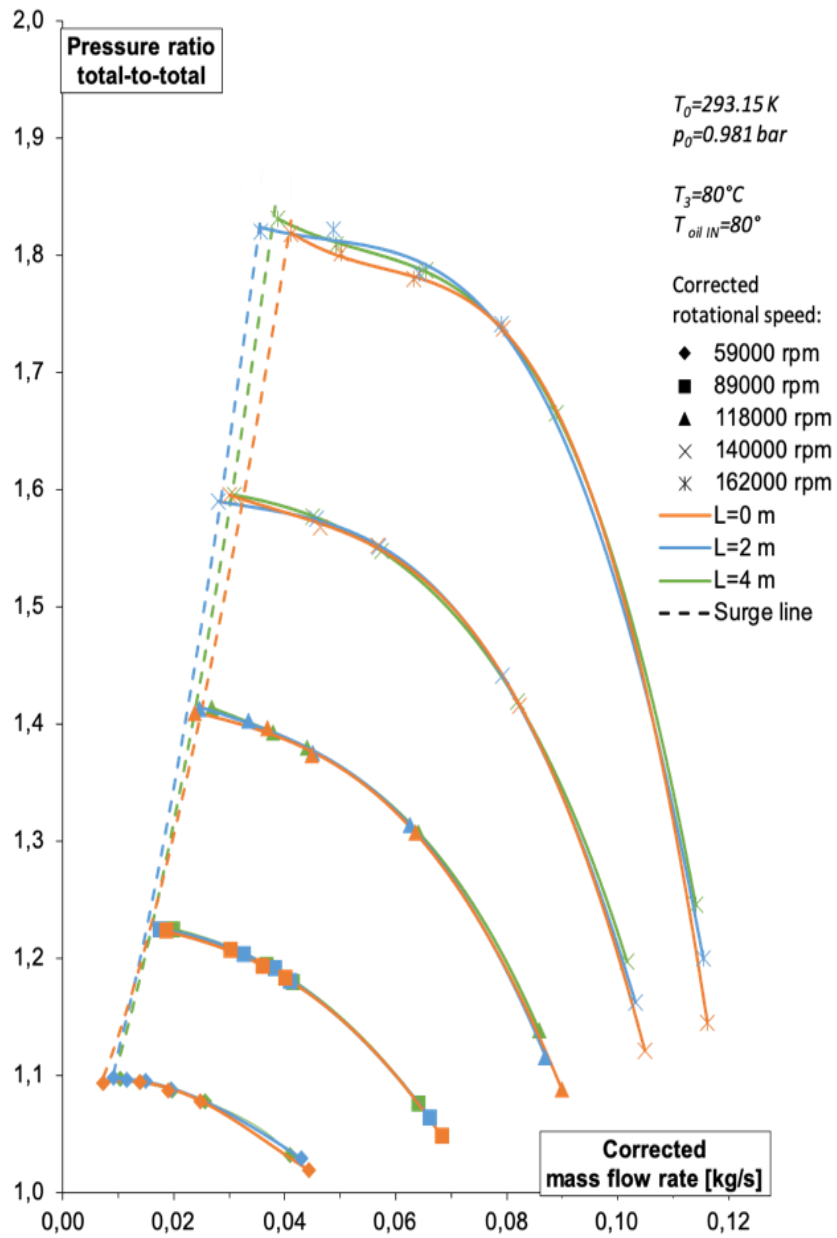
Fig. 5.15 – Comparison of Compressor Steady State Characteristic at Different Length and Constant Plenum Volume (2 liters)

100
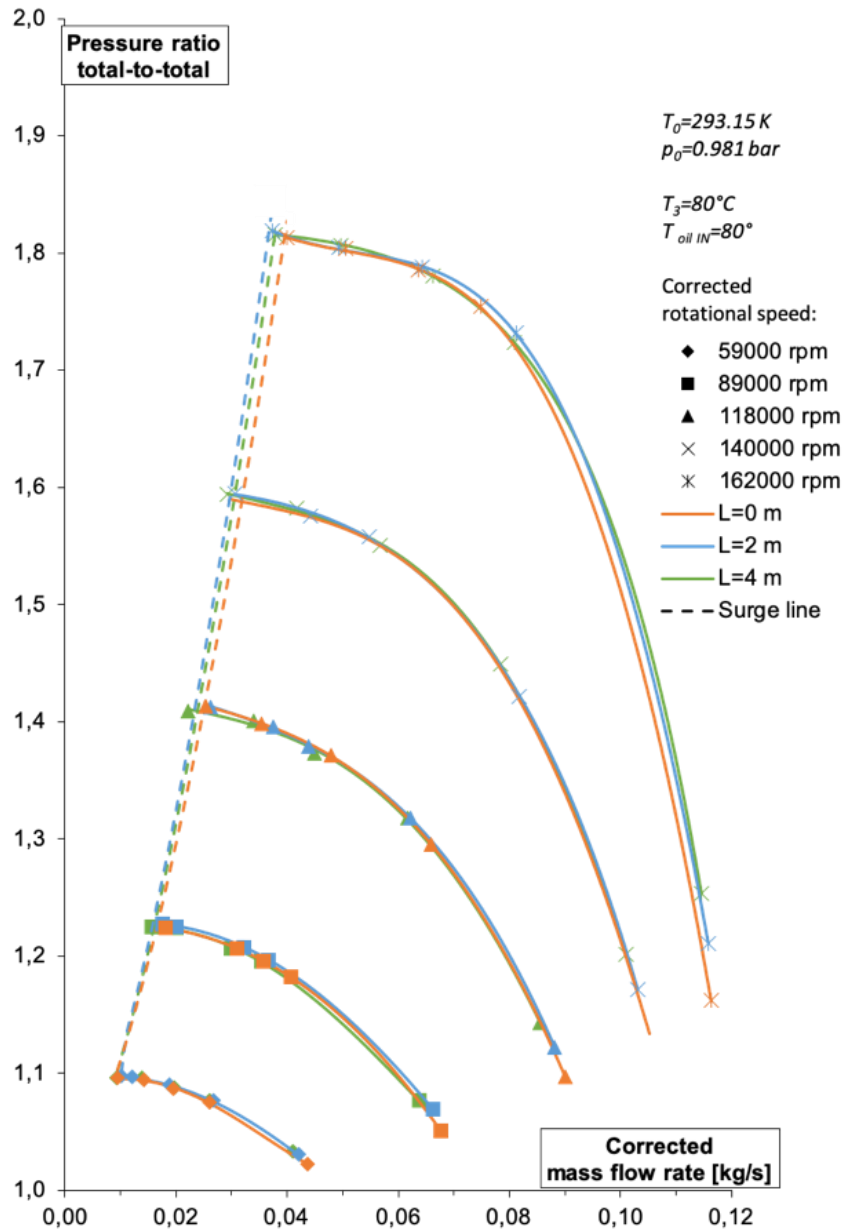
Fig. 5.16 – Comparison of Compressor Steady State Characteristic at Different Length and Constant Plenum Volume (6 liters)

After comparing the steady-state characteristics, the frequencies of pressure and mass flow rate in deep surge were compared. It was observed that the measured surge frequency of the pressure and corresponding mass flow rate were not equal for the same operating condition and configuration. During deep surge, the mass flow rate reverses its direction. This reversal is not captured by the hot fiber film probe because the anemometers used in tests are not sensitive to flow direction. This results in a different frequency of the surge component in the mass flow rate signal. For this reason, it was necessary to identify the points with negative mass flow rate

101

and correct the sign of the mass flow rate in these regions, as shown in Fig. 5.17. After performing this procedure, the Fourier Transforms of the corrected and original signals were compared and shown in Fig. 5.18. The surge frequency component after the mass flow rate signals has been overturned matches the surge frequency in the pressure signal [93].
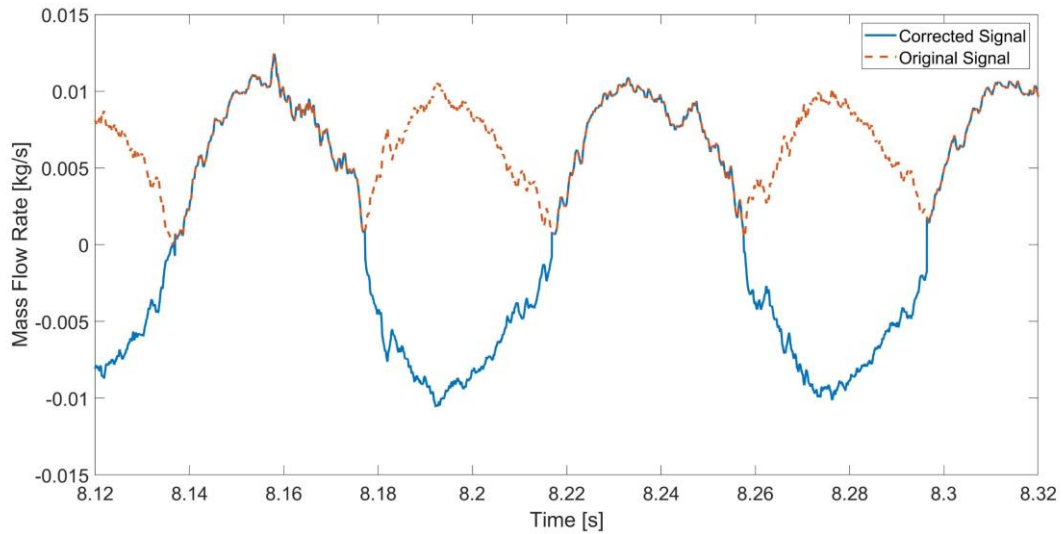
Fig. 5.17 – Mass Flow Rate Signal Measured with a Hot Fiber Film Probe (Original Signal) and Mass Flow Rate Signal after Post-Processing (Corrected Signal)
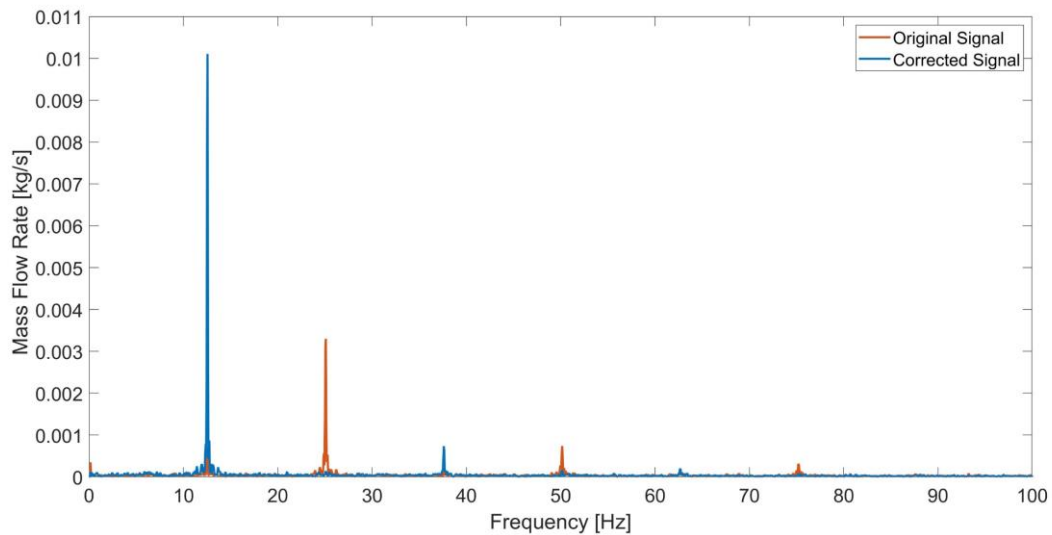
Fig. 5.18 – Fourier Transforms of the Original Mass Flow Rate Signal and of the Corrected Signal

To analyze the deep surge cycles, the time synchronous average of mass flow rate and pressure signals had to be calculated. Since the phenomena is not characterized by a periodicity given by a pulse signal, a slight pulse period variation of each surge cycle was noticed during the observation time. To estimate the real pulse period length cycle by cycle, a processing tool was

102

developed to calculate the point-by-point average signal. The relative position of the points in the cycle was used to perform the time synchronous average. To reduce the noise in the signal a low-pass filter was applied, as shown in Fig. 5.19. The counter anticlockwise arrows indicate the evolution of the pulse cycle during unstable operation. Additional details on the post-processing procedure can be found in the work by Marelli et al. [94].
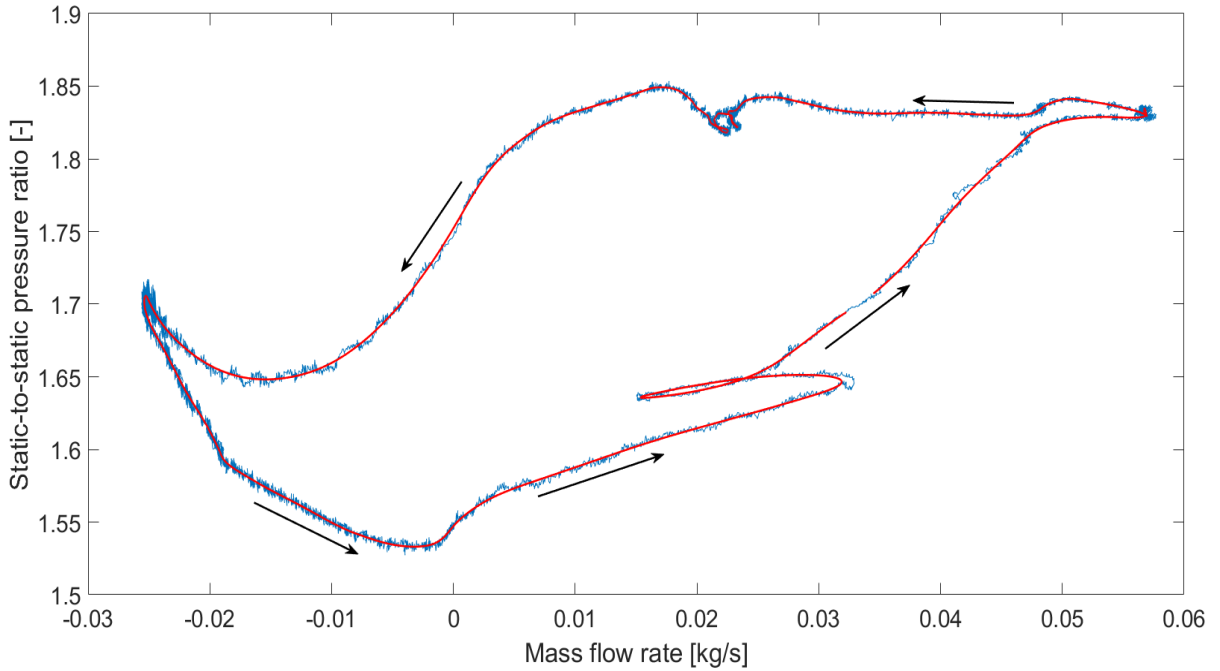
Fig. 5.19 – Time Synchronous Average of the Surge Cycle (Blue) and Filtered Time Synchronous Average of the Surge Cycle (Red)

The surge cycles were analyzed and plotted over the compressor maps, these are shown in Fig. 5.21, Fig. 5.22, Fig. 5.23, Fig. 5.24, Fig. 5.25, and Fig. 5.26 for varying circuit configurations. The pressure sensors measured a static pressure and no instantaneous temperature measurement was recorded. It was not possible to calculate the corrected mass flow rate parameter, so the surge cycle maps are plotted against the mass flow rate and the static-to-static pressure ratio, instead of parameters described in Equations (5.1), (5.2) and (5.3). The area of the surge cycle and the difference between maximum and minimum value of mass flow rate and pressure ratio increases with the corrected rotational speed in all circuit configurations and with length and volume for corrected each rotational speed. The B parameter identified by Greitzer explains this trend: when the speed or the volume increase, B increases, as shown in Equation (5.5); when B increases the variation in mass flow rate increases, while the variation in pressure decreases, as shown in Equations (5.6) and (5.7).

$$B = \frac{u}{2a_p} \sqrt{\frac{V_p}{AL}} \qquad\qquad (5.5)$$

103

$$\frac{d\dot{m}_c^*}{dt^*} = B(p_c^* - p_p^*)$$ (5.6)

$$\frac{dp_c^*}{dt^*} = \frac{1}{B}(\dot{m}_c^* - \dot{m}_t^*)$$ (5.7)

Where:

- u is the tangential speed of the rotor
- a_p is the speed of sound in the plenum
- V_p, A and L are the plenum volume and the area and length of the pipe system
- $\dot{m}_c^*$ and $\dot{m}_t^*$ are the dimensionless compressor and throttle mass flow rates
- p_c^* and p_p^* are the dimensionless compressor outlet and plenum pressures

The circuit configuration affects the position and the shape of the cycle. With the increase in circuit volume, the cycles tend to get thinner and the negative portion of the cycle deviates less from the steady state characteristic. At higher speed, length or volume, the mass in the system increases, making the system slower during transitions. This behavior moves the system to operate closer to the steady-state characteristic also in the negative mass flow rate region. The shape of the steady-state characteristic in the negative area has been measured and calculated in many works: the pressure ratio, approximated as a third order polynomial, decreases moving from the minimum mass flow rate until the mass flow rate becomes zero, as shown in Fig. 5.20 [42], [48]. Therefore, in the negative flow rate region, the surge cycle tends to the steady-state characteristic when the volume or length of the system increases. The position of the cycle is also affected by inertial effects. When circuit volume and rotational speed increase, the delays in the propagation of mass flow rate and pressure waves from the point where instability generates to the measuring station increase. This delay affects the shift between the maximum value of mass flow rate and the maximum value of pressure. For this reason, the cycles at higher rotational speed and for higher configuration volumes shift below the steady state compressor characteristic.
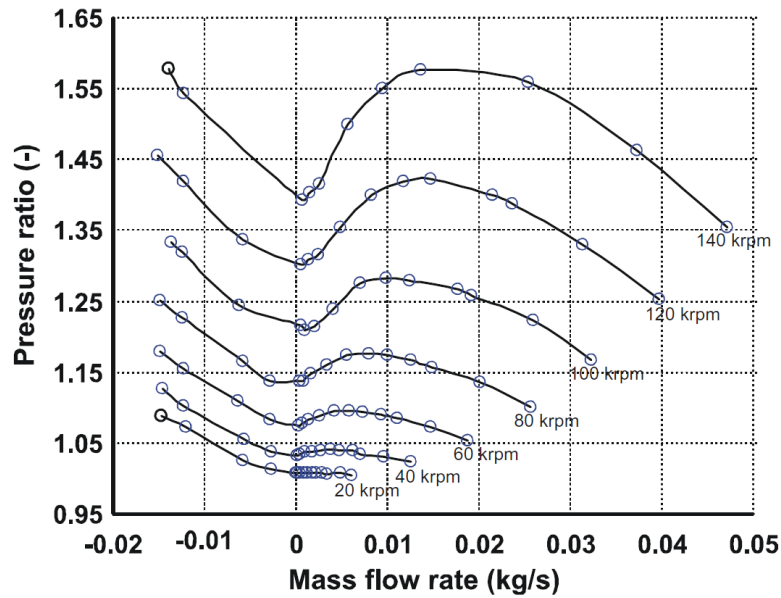
Fig. 5.20 – Compressor Characteristic Curves Extended to the Negative Mass Flow Rate Region [48]
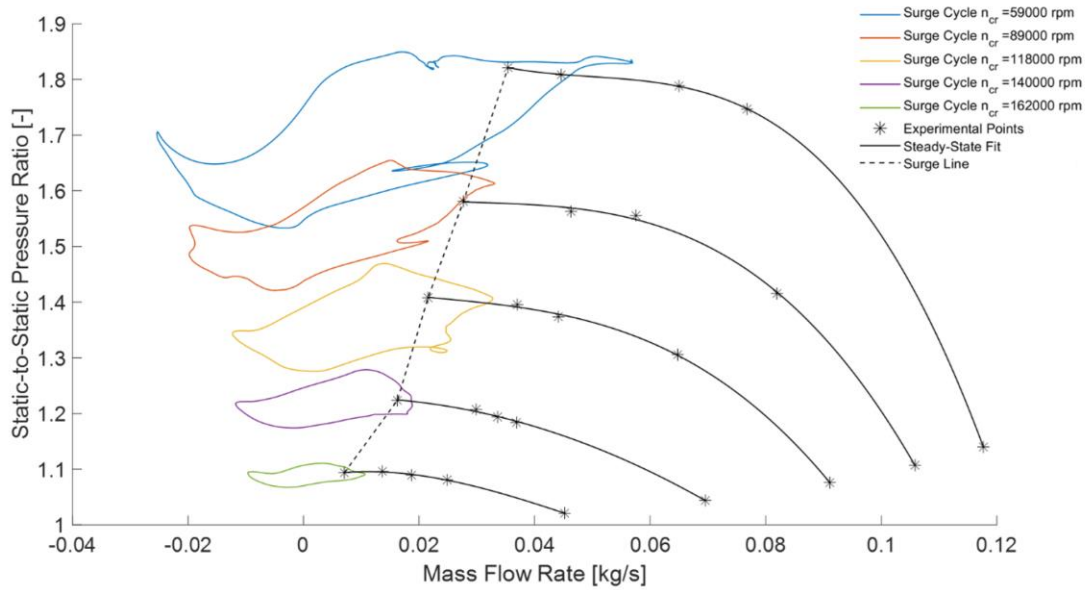
Fig. 5.21 – Compressor Characteristic Curves and Surge Cycles (Circuit Modular Length: 0m, Plenum Volume: 2l)

105
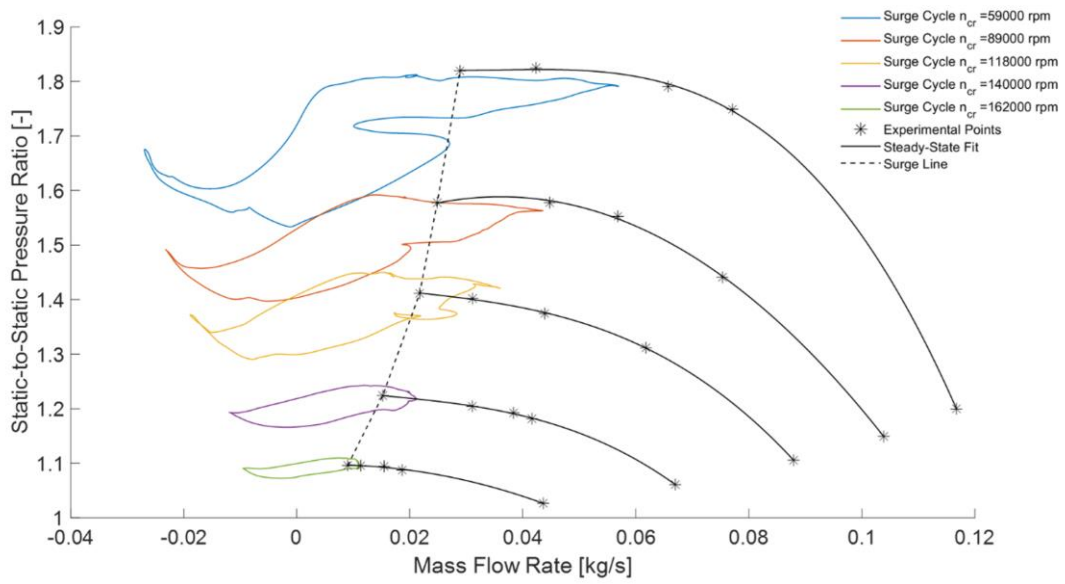
Fig. 5.22 – Compressor Characteristic Curves and Surge Cycles (Circuit Modular Length: 2m, Plenum Volume: 2l)
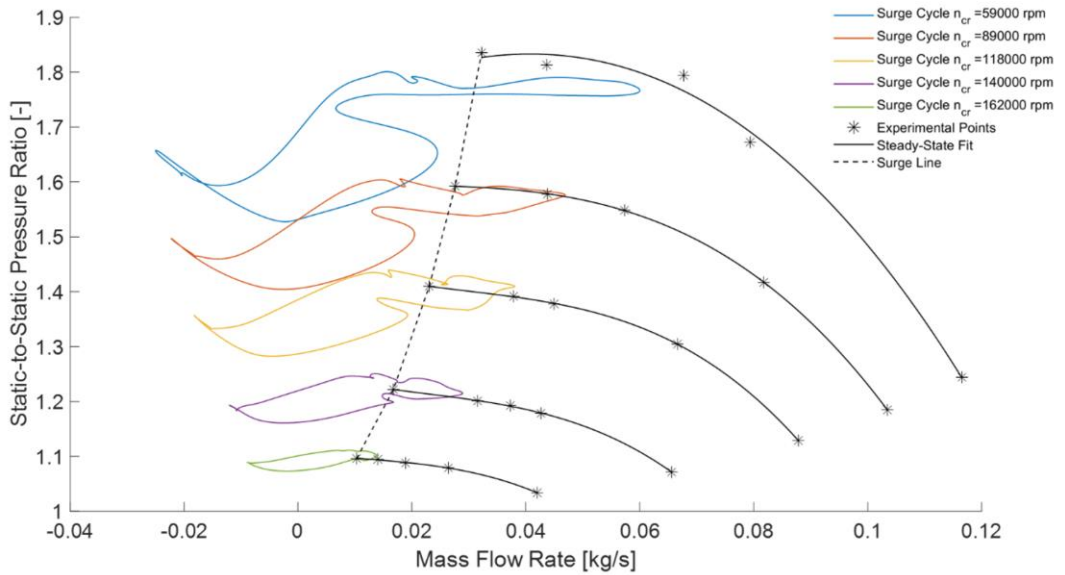
Fig. 5.23 – Compressor Characteristic Curves and Surge Cycles (Circuit Modular Length: 4m, Plenum Volume: 2l)
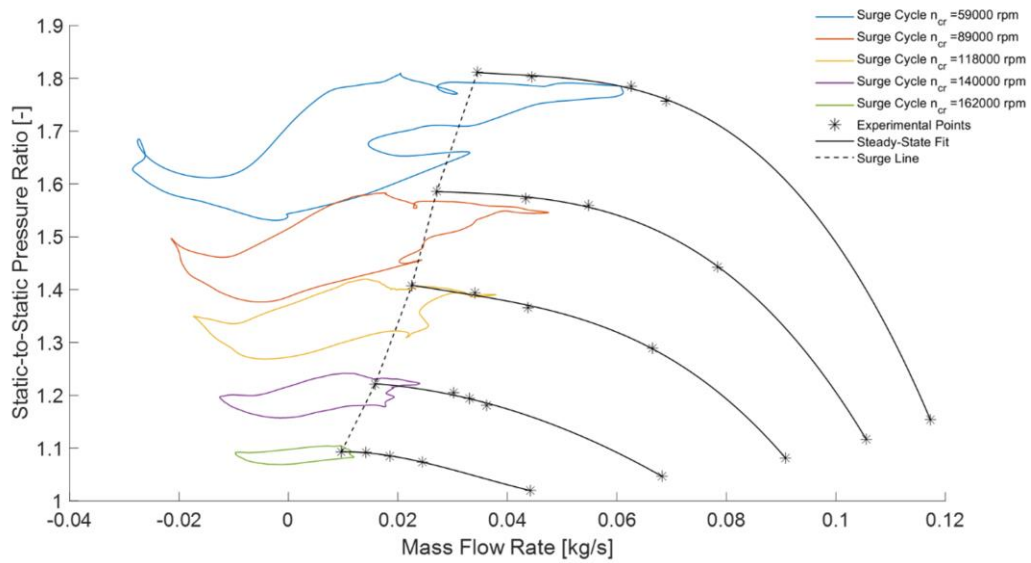
Fig. 5.24 – Compressor Characteristic Curves and Surge Cycles (Circuit Modular Length: 0m, Plenum Volume: 6l)
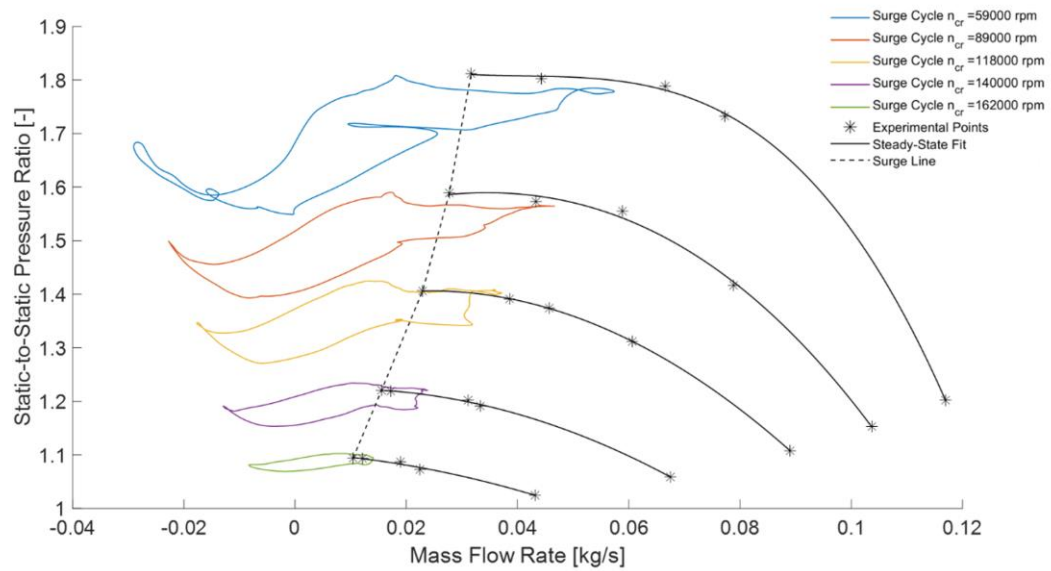
Fig. 5.25 – Compressor Characteristic Curves and Surge Cycles (Circuit Modular Length: 2m, Plenum Volume: 6l)

107
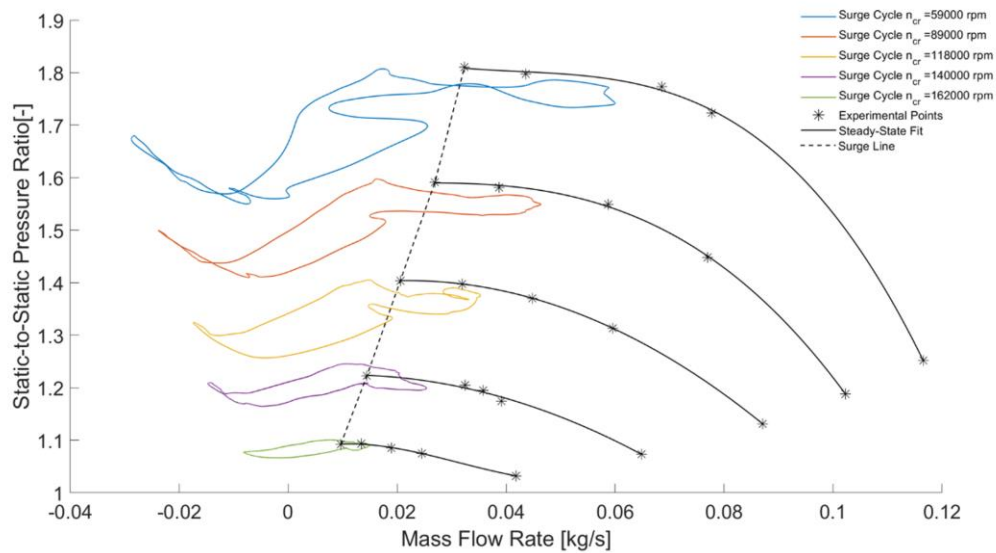
Fig. 5.26 – Compressor Characteristic Curves and Surge Cycles (Circuit Modular Length: 4m, Plenum Volume: 6l)

The time synchronous average of the pressure and the mass flow rate signals at the highest corrected rotational speed are shown in Fig. 5.27 and Fig. 5.28 for the configurations with the lowest and the highest circuit volume. The circuit volume is the sum of the plenum volume and of the pipe volume. The configuration with the highest volume is characterized by a longer cycle, as highlighted by the black boxes. The higher volume of air moving in the systems increases the time necessary for one cycle to occur. In both configurations, the black circles identified with the number one show that a peak in pressure occurs at the lowest values of mass flow rate. This effect is caused by the accumulation of flow in the compressor volute which is not designed for reverse flow conditions. In the highest volume configuration, this behavior increases, due to the higher mass flow present in the system. The filling and emptying behavior of the volute is also highlighted in black circles identified as number two. When the pressure of the volute decreases below the outlet pressure, the mass flow rate reaches a peak. At higher mass flow rates the mass in the volute increases, causing the pressure in the volute to rise. At this point the mass flow rate decreases again. This behavior is more prominent in the configuration higher circuit volume because of the higher mass in the system.
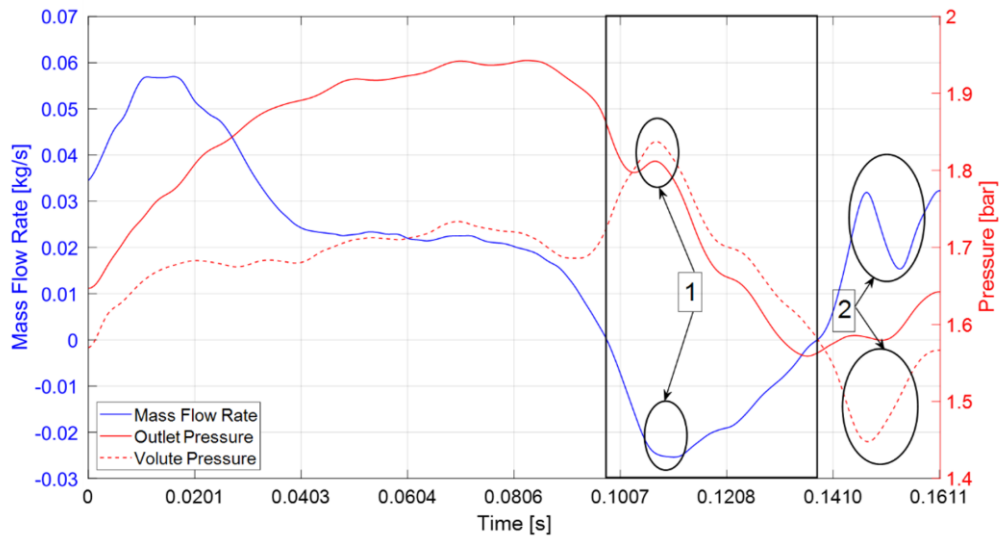
*Fig. 5.27 – Compressor Outlet Pressure, Volute Pressure and Mass Flow Rate Signal
(Rotational Speed: 162000 rpm, Plenum Volume: 2l, Circuit Modular Length: 0m)*
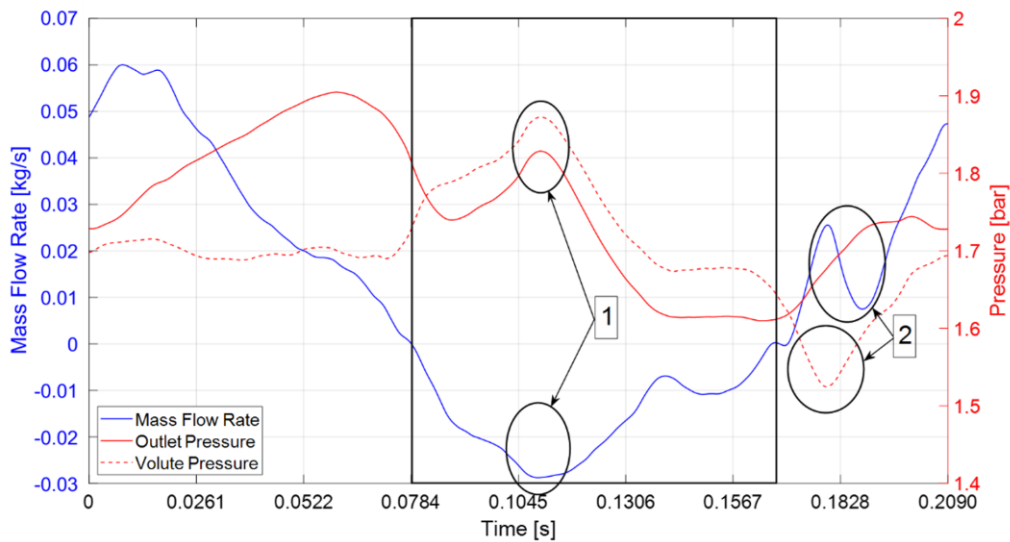
*Fig. 5.28 – Compressor Outlet Pressure, Volute Pressure and Mass Flow Rate Signal
(Rotational Speed: 162000 rpm, Plenum Volume: 6l, Circuit Modular Length: 4m)*

The transient, identified as Run 7, was analyzed to identify surge precursors. The position of the outlet throttle valve was constant, and the compressor speed was increased until the compressor moved into surge. The signals of the microphone, located by the filter, and the pressure transducer in the volute were analyzed. The signals from the microphone were analyzed in the low to medium frequency range to verify the microphone was able to capture low frequency components. The signals from the pressure transducer were analyzed in the high frequency range to verify the ability of the pressure transducer in the volute to capture the appearance of stall components. The auto-power spectra of the microphone signal over the duration of the test

109

is shown in Fig. 5.29. The transient starts in a stable point away from surge where the frequency components in the low frequency region are negligible, shown as the deep blue region towards the bottom of the figure. As the compressor moves towards surge, the amplitude of some frequency components increases and, when surge occurs, the surge amplitude and its multiples appears. The frequency components that appear before the occurrence of surge can be considered as surge precursors. A model that can predict the appearance of these components, can be used to develop a control strategy to identify the limits of compressor operation that can be reached without the occurrence of surge.
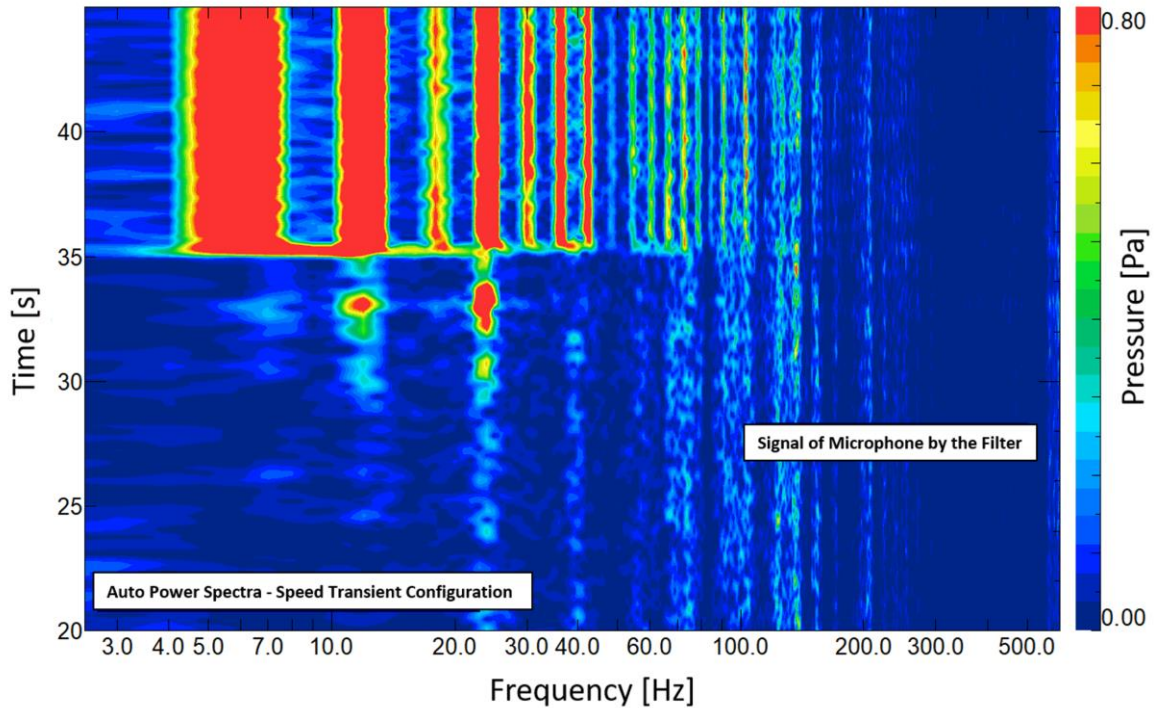
Fig. 5.29 – Auto-Power Spectra of the Signal Measured by the Microphone Located by the Filter (Corrected Rotational Speed: 162000 rpm, Circuit Length: 4 m, Plenum Volume: 6 l)

The auto-power spectra of the pressure in the compressor volute collected during Run 7 is shown as a function of time in the high frequency range in Fig. 5.30. The stable part of the transient ends at second 35; which is the instant when surge occurs. To identify the blade passing frequency, the frequency of the auto-power spectra was divided by the rotational frequency. The normalized value of the blade passing frequency is 10, which is the number of blades in the compressor. During the transient, the amplitude of the blade passing frequency component increases when moving towards the surge limit. In proximity of the surge limit, two other components appear at lower normalized frequencies. These components can be attributed to stall occurrence in the compressor; a phenomenon characterized by a frequency lower than the rotational frequency. This behavior is detected only by the pressure transducer in the volute. When the flow reaches the compressor outlet pressure transducer, these components have been damped and are no longer detectable. The components that appear when moving closer to surge are caused by modulation effects. The modulation of the blade passing frequency component

with the rotating stall component appears with the rotating stall component. These components occurs when the operating point is close to the stability limit.
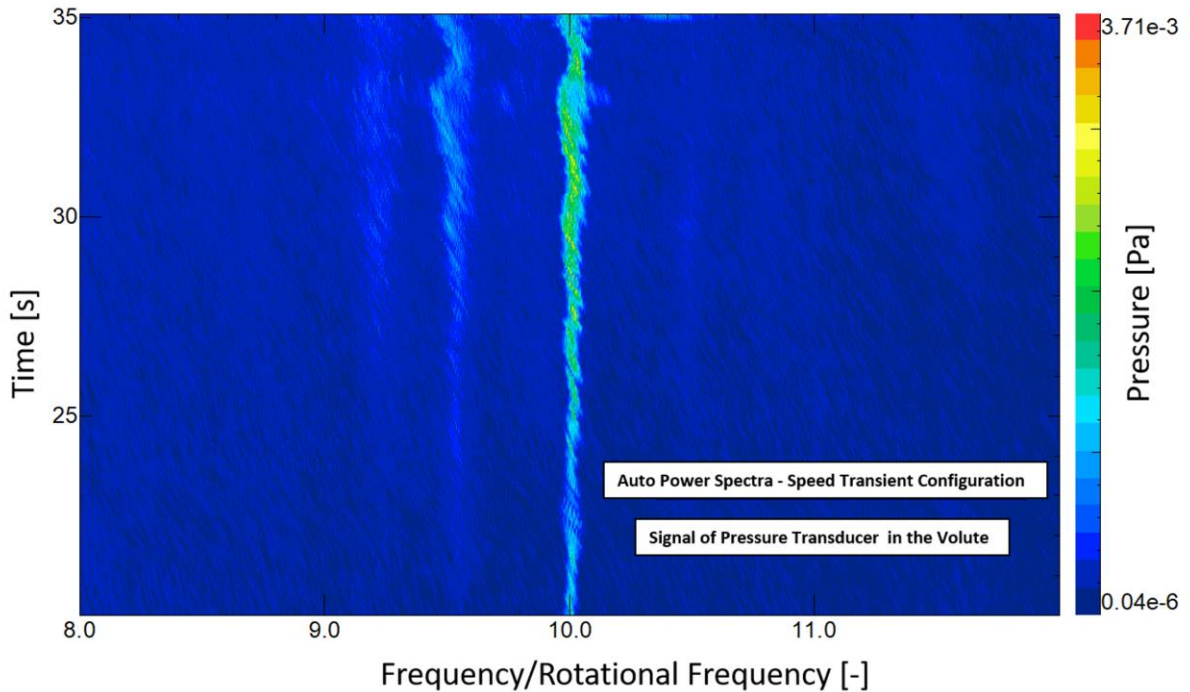
Fig. 5.30 – Auto-Power Spectra of the Signal Measured by the Microphone Located by the Filter (Corrected Rotational Speed: 162000 rpm, Circuit Length: 4 m, Plenum Volume: 6 l)

5.3   Model Results

The model results shown are divided into the calibration and validation of the one-dimensional distributed parameter dynamic model and the analysis of the pressure and mass flow rate signals close to the stability limit.

5.3.1   Model Calibration and Validation

The model was calibrated with a sub-set of the data collected during the second experimental investigation and validated against the data collected in all operating conditions and configurations. The calibration parameters of the dynamic model are the friction coefficients in the pipes upstream and downstream of the compressor, the heat transfer coefficient in the pipe downstream of the compressor and the characteristic length of the compressor. The loss coefficients affect both transient and steady-state conditions, while the characteristic length of the compressor affects the dynamic behavior of the system. The loss parameters were calibrated using data collected during steady-state operation and the compressor characteristic length was calibrated using data collected during surge operation. Before the calibration, the steady-state characteristic of the compressor was extended to the negative mass flow rate region using a third-order polynomial. The polynomial was calculated by imposing the value of total-to-total pressure ratio at zero mass flow rate equal to the pressure ratio predicted by the steady-state model at zero mass flow rate; its first-order derivative with respect to mass flow rate at zero

111

mass flow rate was also imposed equal to the corresponding value calculated by the steady-state characteristic model. The maximum point of the polynomial curve in the positive mass flow rate region corresponded to the maximum point of the calculated steady-state characteristic.

The sub-set of data used to calibrate the model was collected with the two-liter plenum volume and a zero-meter modular length circuit configuration at the corrected rotational speed of 118000 rpm. Since the region of interest consists of the area close to the stability limit, the data collected at maximum mass flow rate was not considered. The calibrated model was then used to calculate system behavior for all steady-state operating conditions and circuit configurations; the values of pressure, mass flow rate and temperature calculated by the model were compared to the experimental values to validate the model. The comparison of mass flow rate, static pressure and total temperature values are shown in Fig. 5.31, Fig. 5.32 and Fig. 5.33. The red line represents the perfect match between the experimental and model value, while the dashed lines represent the 5% error band. The static pressure and total pressure were used to validate the model because these signals are directly measured, and the error of direct measurements is less significant. The pressures and temperatures figures contain data collected at the compressor inlet, at the compressor outlet and in the plenum.
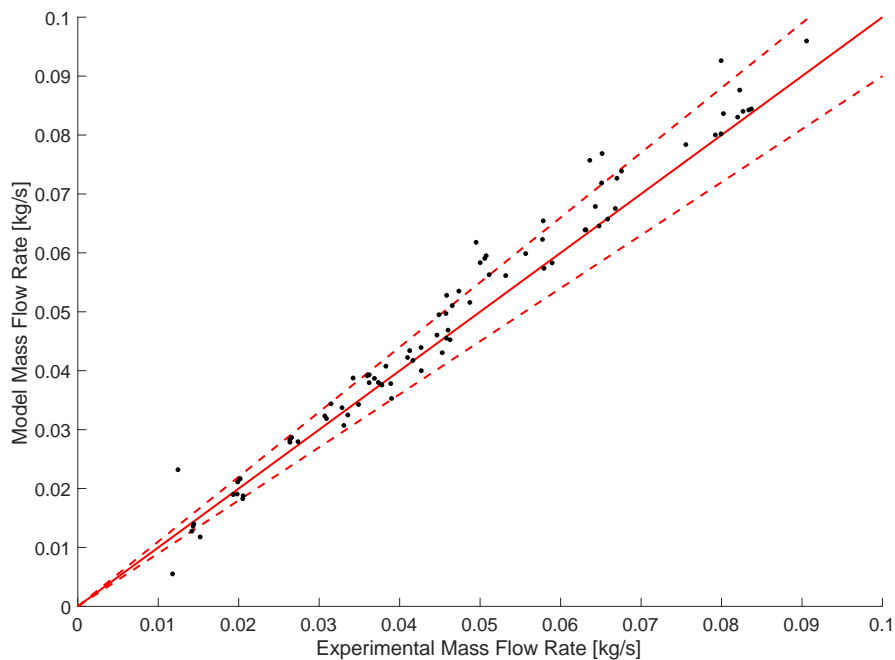
Fig. 5.31 – Comparison of Mass Flow Rate Values Calculated by the Model and Measured Experimentally

112
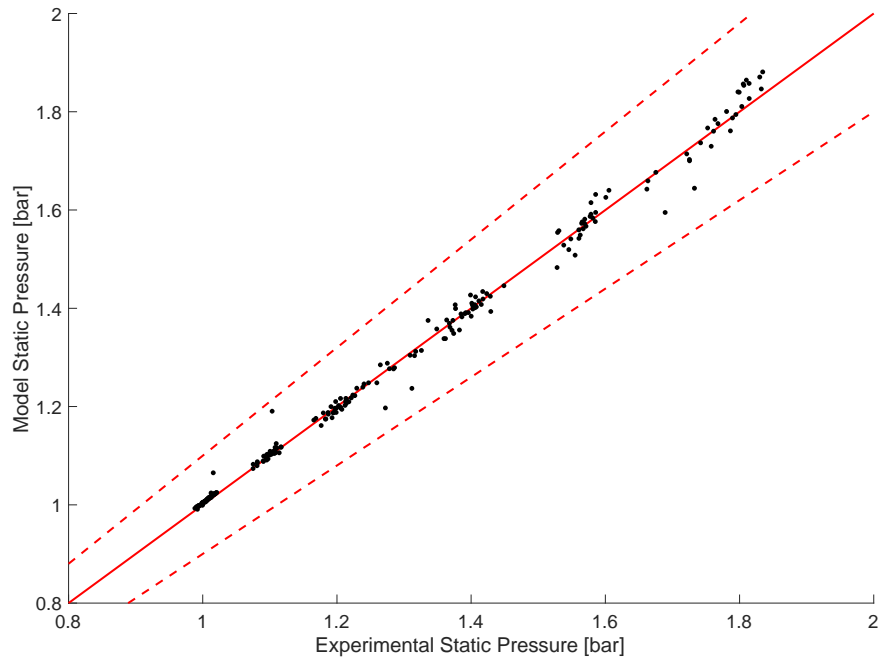
Fig. 5.32 – Comparison of Static Pressure Values Calculated by the Model and Measured Experimentally
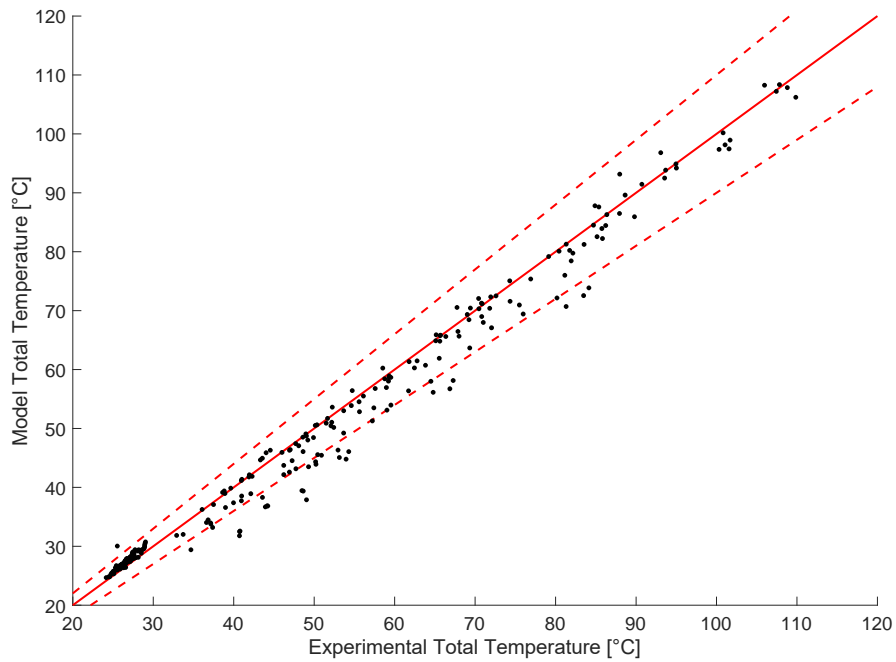
Fig. 5.33 – Comparison of Total Temperature Values Calculated by the Model and Measured Experimentally

113

The majority of the simulation results lie inside the 5% error band, validating the model's ability to predict compressor behavior in the stable region. The points located outside of the band are due to the sub-set of data used for the calibration not having spanned a large enough set compressor corrected rotational speeds. The use of only one compressor characteristic for calibration reduced calibration time at the cost of model accuracy; this becomes more visible at the highest and lowest rotational speeds. The RMS of the error of the signals calculated by location in the system are listed in Tab. 5.3. The error RMS are all less than an acceptable threshold except the plenum total temperature. Using a larger data set for calibration would increase the accuracy of plenum temperature prediction. The losses generated by the rapid section expansion at the plenum inlet are affected by the value of mass flow rate. An increase in the range of mass flow rates over which the model is calibrated allows for better accuracy of both mass flow rate and temperature prediction. Near the stability limit, the characteristic curves become flatter, resulting in a lower effect of mass flow rate on the pressure.

Parameter	Error RMS
Mass Flow Rate	0.002 kg/s
Compressor Inlet Static Pressure	0.007 bar
Compressor Outlet Static Pressure	0.019 bar
Plenum Static Pressure	0.023 bar
Compressor Inlet Total Temperature	0.95 °C
Compressor Outlet Total Temperature	1.59 °C
Plenum Total Temperature	5.18 °C

Tab. 5.3 – RMS of the Error for Different Parameters in Different Points Along the System

The results of calibration and validation in the unstable region are shown in Fig. 5.34. Two different circuit configurations and two different speeds are compared. The model can predict surge amplitude with an error of 9% of the experimental value and the frequency with an error of 10% of the experimental value.
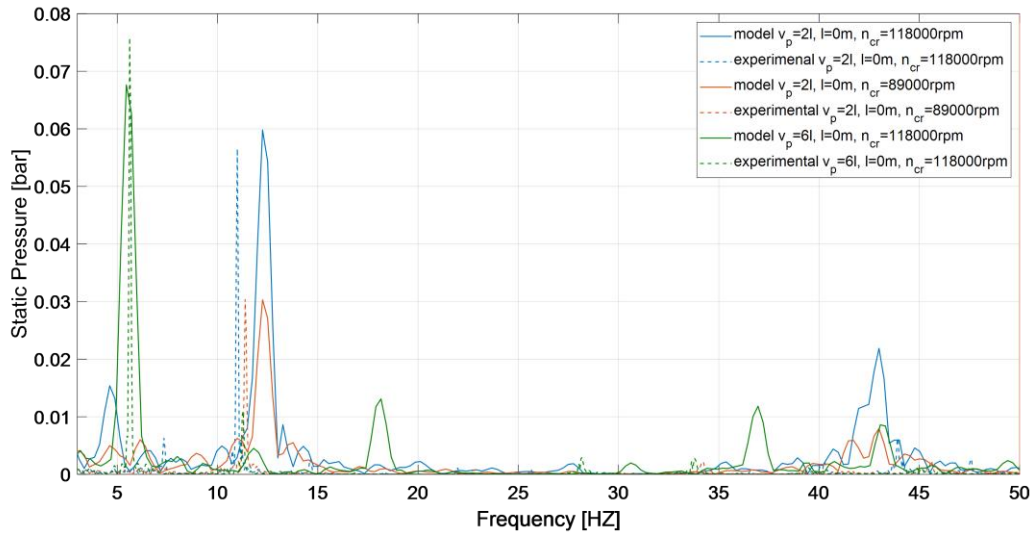
Fig. 5.34 – Comparison of Surge Signals Calculated by the Model and Measured during the Second Experimental Investigation in Three Different Conditions

5.3.2 Analysis of Pressure and Mass Flow Rate Predictions Close to the Stability Limit

Different simulations were then run to evaluate the capability of the model to capture the compressor behavior close to the stability limit. The input valve profile was designed to identify the last stable point before surge. The step profile started from the compressor downstream valve completely open and moved towards the stability limit in smaller and smaller increments. The procedure to choose the valve step profile resembles the experimental procedure to identify the last stable point: the valve is closed in small steps until the compressor operating conditions become unstable; at this point, the valve is opened, and the procedure starts again. This iterative process allows the test operator to identify the valve position corresponding to the last stable point. The procedure to identify the valve profile used as an input to the model was applied and verified on other configurations and at different operating conditions.

The result of a transient from the maximum flow rate point to the last stable point is shown on the compressor characteristic at a corrected rotational speed of 118000 rpm in Fig. 5.35. The model is able to accurately predict the mass flow rate values and pressure ratio of the last stable point.

115
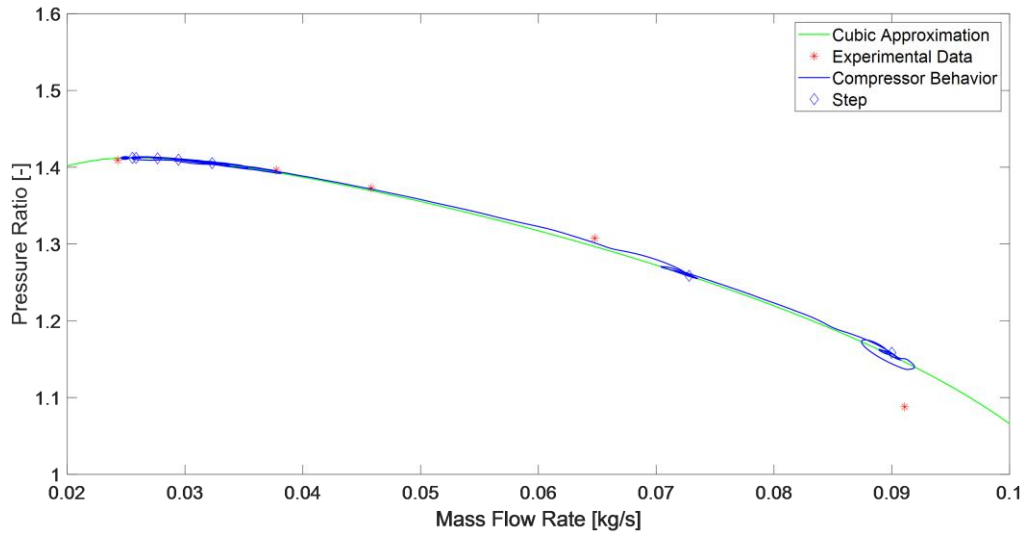
Fig. 5.35 – Compressor Transient Behavior over the Steady-State Characteristic (Corrected Rotational Speed: 118000 rpm, Plenum Volume: 2 l, Modular Circuit Length: 0 m)

For a circuit configuration with a 2-liter plenum volume and a 0-m modular length, the transition to fully developed surge oscillations occurred in three steps: when closing the valve from a stable point close to surge small, stable, oscillations in the mass flow rate and pressure signal occurred; for a small variation in valve position the amplitude of the oscillations increased until the compressor entered a phase of intermittent surge behavior; further closing the valve the compressor entered the unstable operating region where the surge cycles were completely developed. The transition to intermittent surge behavior is shown in Fig. 5.36 between 30 and 40 s.

116
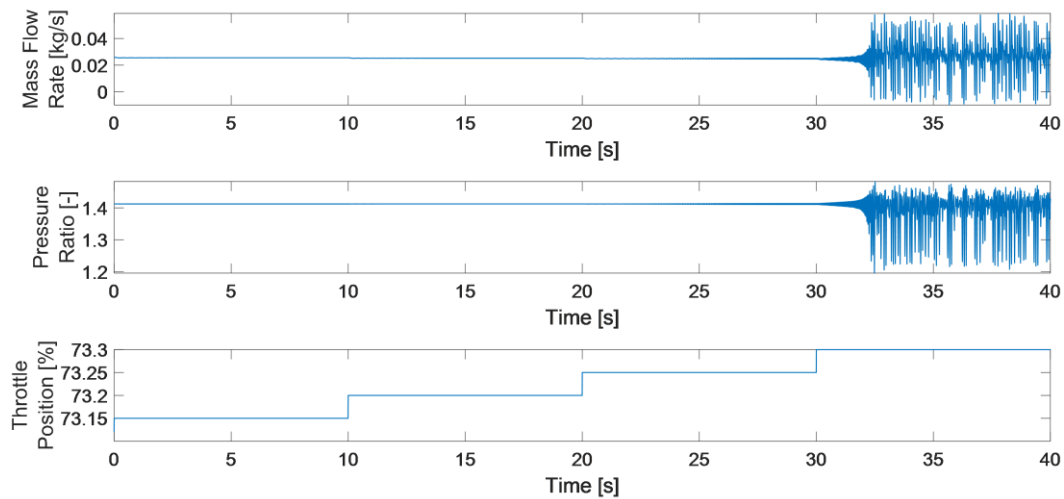
Fig. 5.36 – Compressor Outlet Pressure and Mass Flow Rate Transient Behavior Close to the Stability Limit and in Surge Conditions (Corrected Rotational Speed: 118000 rpm, Plenum Volume: 2 l, Modular Circuit Length: 0 m)

The transient was limited to the stable region to show the appearance of small oscillation in the mass flow rate and pressure signal at the compressor outlet. Surge oscillations are one order of magnitude higher than the small oscillation, making the visibility of the small amplitude oscillations difficult. The small oscillations that appear in mass flow rate and pressure signals close to the stability limit are in shown in Fig. 5.37, Fig. 5.38 and Fig. 5.39. The first figure shows the same transient as Fig. 5.36, while the second and third figure show a different configuration and compressor rotational speed. In all three conditions, the amplitude of the oscillations increases and stabilizes in around 10 seconds. The frequency components present in the signals depend on the operating condition and configuration. At a compressor corrected rotational speed of 140000 rpm and circuit configuration of a 2-liter plenum and 0-meter modular length, the small oscillations preceding surge behavior extend to four different valve positions, as shown in Fig. 5.39. While lumped-parameter surge models, such as the Greitzer model, can capture the small oscillations occurring at the steady-state point with highest pressure ratio, the distributed-parameter model developed in this work can capture the generation of oscillations in different points close to the stability limit [95].

117
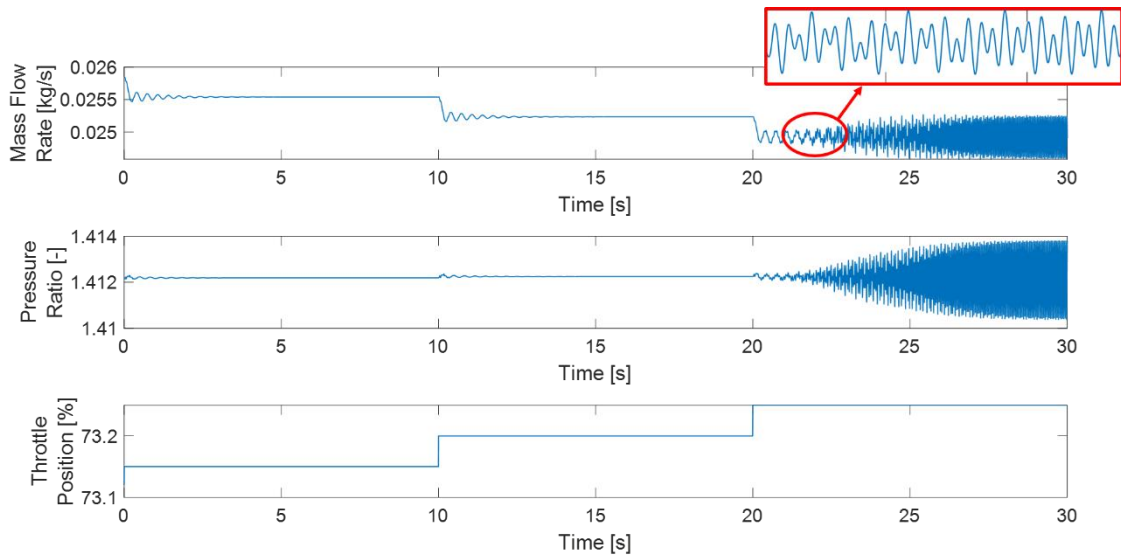
Fig. 5.37 – Compressor Outlet Pressure and Mass Flow Rate Transient Behavior Close to the Stability Limit (Corrected Rotational Speed: 118000 rpm, Plenum Volume: 2 l, Modular Circuit Length: 0 m)
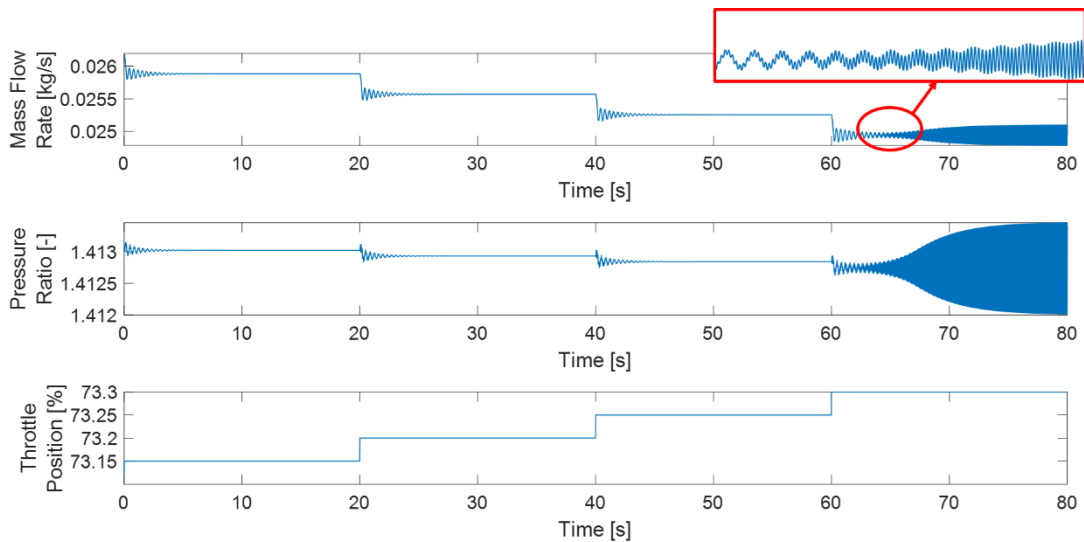
Fig. 5.38 – Compressor Outlet Pressure and Mass Flow Rate Transient Behavior Close to the Stability Limit (Corrected Rotational Speed: 118000 rpm, Plenum Volume: 2 l, Modular Circuit Length: 2 m)

118
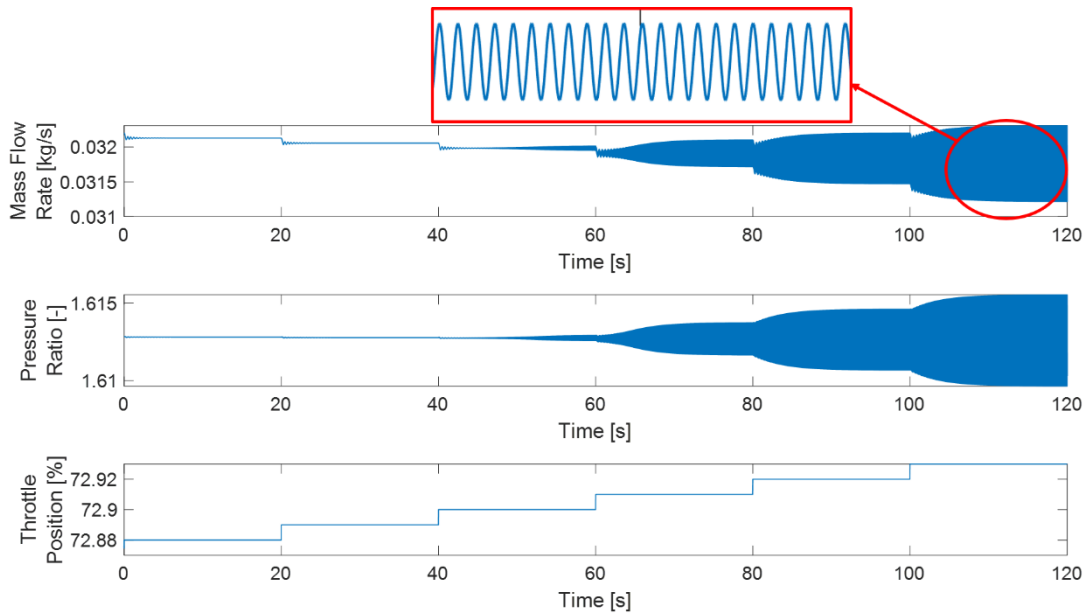
Fig. 5.39 – Compressor Outlet Pressure and Mass Flow Rate Transient Behavior Close to the Stability Limit (Corrected Rotational Speed: 140000 rpm, Plenum Volume: 2 l, Modular Circuit Length: 0 m)

The compressor behavior close to the stability limit is shown in Fig. 5.40. The amplitude of the oscillations close to the stability limit are one order of magnitude less than the surge oscillations. This amplitude increases when moving towards the stability limit. The center of each oscillation, shown as different colored ovals in the figure, move towards the stability limit since the valve is closed to move between oscillation magnitudes.
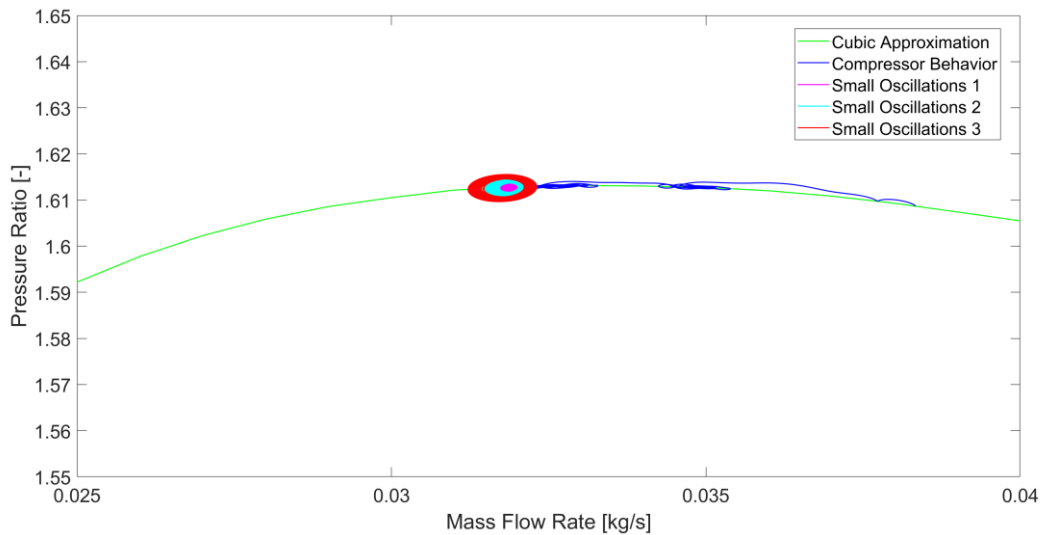
Fig. 5.40 – Compressor Transient Behavior over the Steady-State Characteristic (Corrected Rotational Speed: 140000 rpm, Plenum Volume: 2 l, Modular Circuit Length: 0 m)

119

After studying the compressor behavior, each loss term was analyzed for the same valve profile inputs. While blade loading, recirculation and shear losses increased when the compressor operating point moved close to the surge line, the other loss terms decreased and do not affect the transition to unstable behavior. The values of blade loading, recirculation and shear losses are shown in Fig. 5.41.
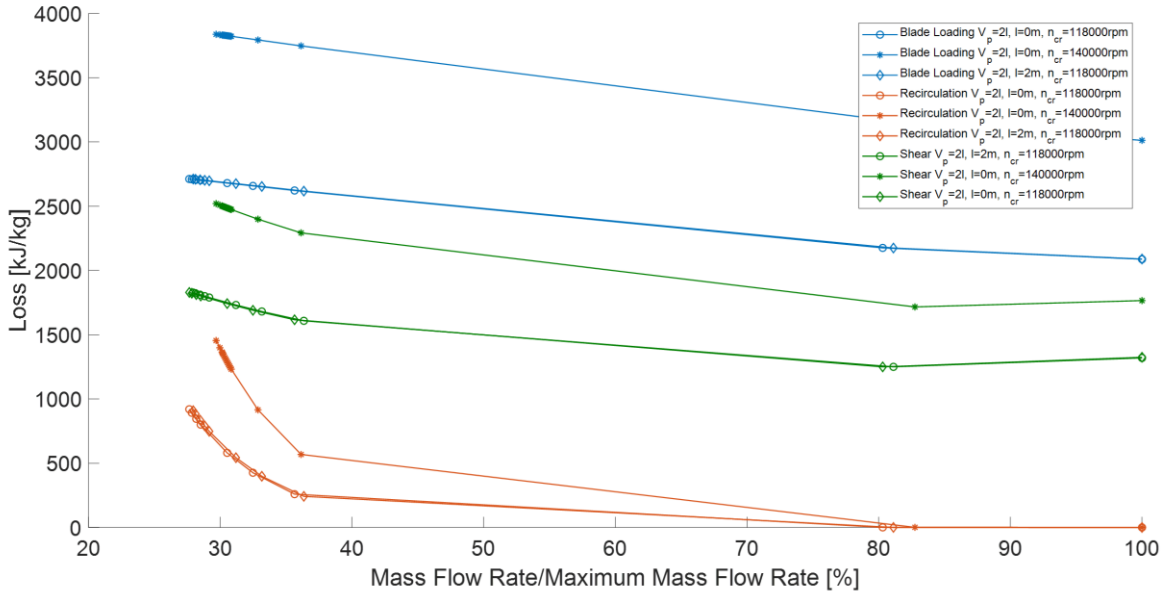
Fig. 5.41 – Blade Loading, Recirculation and Shear Losses for Different Speeds and Circuit Configuration

Even though the blade loading losses are higher than the other two loss terms, the recirculation losses increase rapidly close to the stability limit having been negligible in the choking region. The derivative of each loss terms with respect to mass flow rate was calculated and is shown in Fig. 5.42. The derivative of the recirculation losses increases rapidly when moving close to the surge line, proving that this loss term is the main factor in the drop of pressure ratio which occurs in unstable behavior. This behavior suggests the highly tangential flow at the impeller outlet generates stall regions that can cause the transition from stable to unstable behavior in the compressor.

120
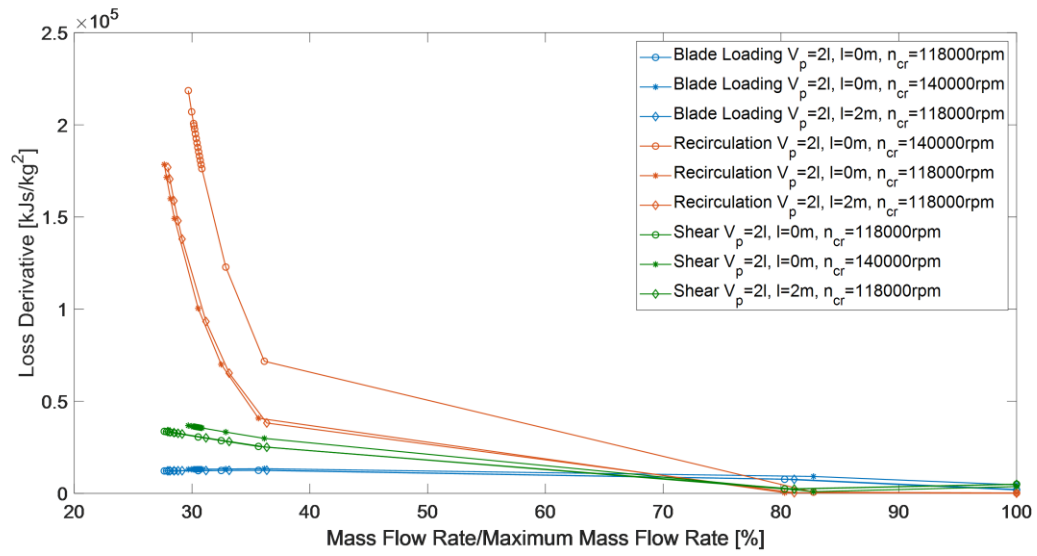
Fig. 5.42– Derivative of Blade Loading, Recirculation and Shear Losses for Different Speeds and Circuit Configuration

121

6 Conclusion

This works describes the experimental and modeling activity developed to increase the understanding of surge phenomena in an automotive turbocharger compressor and prepare a foundation for a control model for surge avoidance. The work is divided in three stages: during the first stage an experimental investigation was performed; in the second stage a control oriented model was developed, and during the third stage a second experimental investigation was conducted, and its results used to calibrate and validate the model.

The aim of the fist experimental investigation was to design and conduct a set of tests that would increase the knowledge on compressor behavior close to the stability limit and analyze the impact of the compressor outlet circuit on the transition from stable to unstable behavior. The experimental investigation was conducted at the internal combustion engine component test facility of the University of Genoa. The data collected on a small turbocharger centrifugal compressor was analyzed and the results were used to develop a one-dimensional distributed-parameter model of the compressor and the pipe system. The second experimental investigation was performed to collect data to validate the model, an increased number of measurements allowed the analysis of compressor behavior during deep surge operation.

The experimental facility at the University of Genoa is designed to test automotive turbochargers. It consists of an open-loop configuration, where the inlet conditions to turbine and compressor can be independently controlled. The layout allows the testing of the compressor and turbine independently by using the other machine as either a motor or a dynamometer. The testing facility also allows for either high temperature or unsteady testing. The turbine feeding line has two branches: in one branch an electrical heater allows testing at high temperature and the analysis of heat exchange in turbocharger, in the other branch a rotating valve system or a cylinder head allows the testing of the turbine during unsteady operating conditions. The measuring and acquisition systems allow the measurement of temperatures, pressures, mass flow rates, frequency and position in different points along the system at a high sampling frequency.

The turbocharger characteristics, the experimental layout and the experimental procedures were described for the first and second experimental investigation. The compressor is a small centrifugal compressor with a vaneless diffuser. It is part of a turbocharger for automotive application, used on 1.4 liter, 4-cylinder internal combustion engines. The experimental layout was designed specifically for surge tests: a modular compressor outlet circuit was designed. The length of the pipe at compressor outlet could be varied between 1.6 and 6.1 m in steps of 0.5 m. The volume of a plenum located downstream of the compressor outlet pipe and upstream of the motorized throttle valve could be varied between 2 l and 12 l in steps of 1 l. This compressor outlet layout was maintained for both experimental investigations, though the tested configurations were varied between the first and second experimental investigation. Instantaneous pressure was measured in different locations along the system. The instantaneous and average turbocharger speed was measured during all tests. During both experimental investigations, the stable area of the compressor map was analyzed at five different compressor corrected rotational speeds. Since the region of interest is close to the stability limit, the test

operating conditions analyzed were concentrated close to the surge line. After the measurements in stable operation, different transient tests were performed.

With mentorship from the Center for Automotive Research at the Ohio State University, the model was developed in two phases: the first concentrated on the calculation of compressor the steady-state characteristic in the stable and unstable regions, and the second on the integration of the steady-state characteristic into a dynamic model of the compressor and pipe system. The steady-state was calculated with a stream line analysis of the inducer, impeller and diffuser of the compressor. The conservation of mass, momentum and energy equations were applied to each component. A sensitivity analysis was performed to establish the impact of different loss terms found in literature on the shape and position of the compressor steady-state characteristic. The results of the sensitivity analysis were then used to calibrate the steady-state characteristic and verify the ability to calculate the compressors characteristics in the stable operating region. The jet and wake theory was then analyzed and applied to extend the calculation to the unstable region. The limitations were highlighted, and the results provided insight into the loss terms that needed to be added and modified to predict the compressor behavior in the unstable region. The extended compressor steady-state model was then calibrated and integrated in the dynamic model. The dynamic model of the compressor and pipe system consist of one-dimensional conservation of mass, momentum and energy equations applied to a staggered grid. The baseline pipe equations were modified to take into account the different behavior of the compressor, plenum, throttle valve and open-end pipes. For the compressor equations, the momentum equation was modified so that the rate of change of compressor mass flow rate would be proportional to the difference between the total pressure given by the steady-state characteristic and the actual total pressure at the compressor outlet.

The results of the first experimental investigation showed the appearance of small amplitude oscillations at the last stable operating point. The amplitude of these oscillations was an order of magnitude smaller than the surge oscillations, and the frequency varied with the compressor rotational speed and circuit configuration. The frequency of the small amplitude oscillations did not match the surge frequency and were only present at lower rotational speed conditions. This behavior was observed for all compressor outlet circuit length and plenum volume. The additional measurements collected during the second experimental investigation gave the opportunity to study the pressure and mass flow rate signals collected during deep surge operation. The shape and position of the surge cycles was affected by the compressor outlet circuit configuration and by the compressor corrected rotational speed. At higher rotational speeds and higher circuit volume, the pressure amplitude decreased, while the mass flow rate amplitude increased. This behavior was confirmed by Greitzer's compressor theory. The position of the surge cycles was also affected by the same parameters: at high rotational speeds and volumes the different propagation time in the mass flow rate and pressure signals generated a shift between the maximum mass flow rate and maximum pressure. The pressure signals in the compressor volute and at the compressor outlet with the mass flow rate signals also highlighted the volute emptying and filling phenomena and how the compressor outlet circuit affects this behavior. At higher rotational speeds and volumes, the higher mass in the system increases the emptying and filling phenomena in the volute resulting in higher pressure and mass flow rate variations. The model results showed the ability of the model to predict compressor behavior in stable and unstable behavior. The model predicted surge amplitude and

123

frequency with a maximum error of 10 %. The model also predicted the small amplitude oscillations that occur close to the stability limit for different circuit configurations.

Throughout the course of this work, many lessons were discovered that would make repeating or continuing the development of the experimental tests and model more efficient and accurate. On the experimental side, simplifying the compressor circuit while maintaining the measurements of instantaneous and average signals in the system would simplify the model to concentrate on the key elements of the system that cause a transition to unstable behavior. The use of a closed-loop control of the throttle valve would allow a quantitative technique to identify the position of the surge line and perform different types of transients into unstable behavior. Component level testing would have also provided data to set up each calibration parameter in the dynamic model and characterize the losses in the system independently from compressor losses. While the model developed in this work can accurately predict compressor behavior, there were many assumptions that were made on which physical phenomena were most crucial to the transition to surge behavior. These assumptions could have been better proven through collaboration with a computational fluid dynamics group. In addition, a different calibration procedure could have increased the accuracy of the model results; for example, using a swarm or brute-force optimization technique along with more computational power could have improved the final calibration.

This compressor model reduces the amount of calibration data to a few compressor characteristics curves and transients. While the compressor transients were collected during the transition from stable to unstable behavior to study surge behavior, data collected during a transient in the stable region would be sufficient for calibrating the model. This model could be used as a foundation for model predictive control or similar control methodologies. The development of the control model would allow the compressor to operate close to the stability limit in the higher efficiency area, increasing not only the efficiency of the whole system but also the operating range of the coupled internal combustion engine.

Bibliography

[1]   "Official Journal of The European Union L 175," 7 July 2017.

[2]   "Worldwide harmonized Light vehicles Test Procedure (WLTP)," UNECE Wiki.

[3]   W. Bandel, G. K. Fraidl, P. E. Kapus and H. Sikinger, "The Turbocharged GDI Engine: Boosted Synergies for High Fuel Economy Plus Ultra-Low Emissions," in *SAE Technical Paper 2006-01-1266*, 2006.

[4]   L. Cornolti, A. Onorati, T. Cerri, G. Montenegro and F. Piscaglia, "1D Simulation of a Turbocharged Diesel Engine with Comparison of Short and Long EGR route Solutions," *Journal of Applied Energy,* vol. 111, pp. 1-15, 2013.

[5]   F. Bozza, A. Gimelli, L. Strazzullo, E. Torella and C. Cascone, "Steady State and Transient Operation Simulation of a Downsized Turbocharged SI Engine," in *SAE Technical Paper, 2007-01-0381*, 2007.

[6]   N. Fraser, H. Blaxill, G. Lumsden and M. Bassett, "Challenges for Increased Efficiency thorugh Gasoline Engine Downsizing," *SAE International Journal of Engines,* vol. 2, no. 1, pp. 991-1008, 2009.

[7]   R. Hunziker, H. P. Dickmann and R. Emmrich, "Numerical and Experimental Investigation of a Centrifugal Compressor with an Inducer Casing Bleed System," *Proceeding of the Institution of Mechanical Engineers, Part A: Journal of Power and Energy,* vol. 215, pp. 783-791, 2001.

[8]   H. Kindl, N. Schorn, H. Schulte and J. R. Serrano et al., "Influence of Various Compressor Inlet Design on Compressor Performance," in *THIESEL, Conference on Thermo and FLuid Dynamics Processes in Diesel Engines*, 2004.

[9]   T. Lake et al., "Turbocharging Concepts for Downsized DI Gasoline Engines," in *SAE Technical Paper 2003-01-0036*, 2004.

[10]   B. Lecoint and G. Monnier, "Downsizing a Gasoline Engine Using Turbocharging with Direct Injection," in *SAE Technical Paper 2003-01-0542*, 2003.

[11]   S. Marelli, "Sistemi Propulsivi a Ridotto Impatto Ambientale," Class Notes, Università degli Studi di Genova.

[12]   J. Galindo, A. Tiseira, R. Navarro, D. Tarì and C. M. Meano, "Effect of the inlet geometry on performance, surge margin and noise emission of an automotive turbocharger compressor," *Applied Thermal Engineering,* vol. 110, pp. 875-882, 2017.

[13]   A. Stein, S. Niazi and L. N. Sankar, "Numerical Studies of Stall and Surge Alleviation in Compressors," Class Notes, School of Aerospace Engineering, Georgia Tech.

[14] R. Dehner, A. Selamet, P. Keller and M. Becker, "Simulation of Mild Surge in a Turbocharger Compression System," in *SAE Technical Paper 2011-01-1527*, 2011.

[15] M. Dehner, A. Selamet, P. Keller and M. Becker, "Prediction of Surge in a Turbocharger Compression System vs. Measurements," in *SAE Technical Paper 2010-01-2142*, 2010.

[16] R. Dehner, A. Selamet, P. Keller and M. Becker, "Instabilities at the Low-Flow Range of a Turbocharger Compressor," in *SAE Technical Paper 2013-01-1886*, 2013.

[17] E. M. Geitzer, "Surge and Rotating Stall in Axial Flow Compressors - Part I: Theoretical Compression System Model," *Journal of Engineering for Gas Turbines and Power*, vol. 98, no. 2, pp. 190-198, 1976.

[18] E. M. Greitzer, "Surge and Rotating Stall in Axial Flow Compressors Part II: Experimental Results and Comparison with Theory," *ASME Transaction - Journal of Engineering for Power,* vol. 98, pp. 199-217, 1976.

[19] F. K. Moore and E. M. Greitzer, "A Theory of Post-Stall Transients in Axial Compression Systems: Part I - Developement of Equations," *Journal of Engineering for Gas Turbines and Power,* vol. 108, no. 1, pp. 68-76, 1986.

[20] K. Toyama, P. W. Runstadler and R. C. Dean, "An Experimental Study of Surge in Centrifugal Compressors," *ASME Journal of Fluids Engineering,* vol. 99, pp. 115-131, 1977.

[21] R. C. Dean and L. R. Young, "The Time Domain of Centrifugal Compressor and Pump Stability and Surge," *Journal of Fluids Engineering,* vol. 99, pp. 53-63, 1977.

[22] D. A. Fink, N. A. Cumpsty and E. M. Greitzer, "Surge Dynamics in a Free-Spool Centrifugal Compressor System," *Journal of Turbomachinery,* vol. 114, pp. 321-332, 1992.

[23] K. E. Hansen, P. Jorgensen and P. S. Larsen, "Experimental and theoretical study of surge in a small centrifugal compressor," *Journal of Fluids Engineering,* vol. 103, no. 3, pp. 391-395, 1981.

[24] J. Galindo, J. R. Serrano, X. Margot, A. Tiseira, N. Schorn and H. Kindl, "Potential of Flow Pre-Whirl at the Compressor Inlet of Automotive Turbochargers to Enlarge Surge Margin and Overcome Packaging Limitations," *International Journal of Heat and Fluid Flow,* vol. 28, pp. 374-387, 2007.

[25] S. Marelli, C. Carraro, S. Moggia and M. Capobianco, "Effect of Circuit Geometry on Steady Flow Performance of an Automotive Turbocharger Compressor," *Energy Procedia,* vol. 101, pp. 630-637, 2016.

[26] S. Marelli, M. Capobianco and G. Zamboni, "Pulsating Flow Performance of a Turbocharger Compressor for Automotive Application," *International Journal of Heat and Fluid Flow,* vol. 45, no. 1, pp. 158-165, 2014.

126

[27] J. Galindo, J. R. Serrano, C. Guardiola and C. Cervellò, "Surge Limit Definition in a Specific Test Bench for the Characterization of Automotive Turbochargers," *Journal of Experimental Thermal and Fluid Science,* vol. 30, pp. 449-462, 2006.

[28] F. Bozza, V. De Bellis, S. Marelli and M. Capobianco, "1D Simulation and Experimental Analysis of a Turbocharger Compressor for Automotive Engines under Unsteady Flow Conditions," *SAE International Journal of Engines,* vol. 4, pp. 1365-1385, 2011.

[29] S. Marelli and M. Capobianco, "Experimental investigation under unsteady flow conditions on turbocharger compressors for automotive gasoline engines," in *IMechE, 10th International Conference on Turbochargers and Turbocharging*, 2012.

[30] M. Shu, M. yang, K. Zhang, K. Deng, B. Yang and R. Martinez-Botas, "Experimental study on performance of centrifugal compressor exposed to pulsating backpressure," in *Aerospace Science and Technology*, 2019.

[31] J. Galindo, H. Climent, C. Guardiola and A. Tiseira, "On the effect of pulsating flow on surge margin of small centrifugal compressors for automotive engines," *Experimental Thermal and Fluid Science,* vol. 33, pp. 1163-1171, 2009.

[32] M. Yunfei et al., "Numerical Prediction of Stall Inception in Centrifugal Compressor Using Eigenvalue Method," in *ASME Turbo Expo 2015: Turbine Technical Conference and Exposition*, 2015.

[33] M. Vagani, A. Engeda and M. J. Cave, "Prediction of Impeller Rotating Stall Onset Using Numerical Simulations of a Centrifugal Compressor. Part 1: Detection of Rotating Stall Using Fixed-Flow Transient Simulations," *Proceeding of the Institution of Mechanical Engineers, Part A: Journal of Power and Energy,* vol. 227, no. 4, pp. 403-414, 2013.

[34] M. Carretta, C. Cravero and D. Marsano, "Numerical Prediction of Centrifugal Compressor Stability Limit," in *Turbo Expo 2017*, 2017.

[35] M. Bardelli, C. Cravero, M. Marini, D. Marsano and O. Milingi, "Numerical Investigation of Impeller-Vaned Diffuser Interaction in a Centrifugal Compressor," *Applied Sciences,* vol. 9, no. 8, p. 1619, 2019.

[36] D. Eckardt, "Instantaneous Measurements in the Jet-Wake Discharge Flow of a Centrifugal Compressor Impeller," *Journal of Engineering for Power,* vol. 97, no. 3, pp. 337-345, 1975.

[37] R. C. Dean and Y. Senoo, "Rotating Wakes in Vaneless Diffusers," *Journal of Basic Engineering,* vol. 82, no. 3, pp. 563-570, 1960.

[38] S. Ljevar, H. C. De Lange and A. A. Van Steenhoven, "Two-Dimensional Rotating Stall Analysis in a Wide Vaneless Diffuser," *Internationa Journal of Rotating Machinery,* 2006.

127

[39] M. Schleer, S. Jin Song and R. S. Abhari, "Clearance Effects on the Onset of Instability in a Centrifugal Compressor," *Journal of Turbomachinery,* vol. 130, no. 3, p. 031002, 2008.

[40] O. Leufvén and L. Eriksson, "A Surge and Choke Capable Compressor Flow Model-Validation and Extrapolation Capability," *Journal of Control Engineering Practice,* vol. 21, no. 12, pp. 1871-1883, 2013.

[41] O. Leufvén and L. Eriksson, "Time to Surge Concept and Surge Control for Acceleration Performance," *Proceeding of the 17th IFAC World Congress,* pp. 2063-2068, 2008.

[42] J. T. Gravdahl et al., "Modeling of Surge in Free-Spool Centrifugal Compressors: Experimental Validation," *Journal of Propulsion and Power,* vol. 20, no. 5, pp. 849-857, 2004.

[43] H. W. Oh and E. S. Yoon, "An Optimum Set of Loss Models for Performance Prediction of Centrifugal Compressors," *Proceedings of the Institution of Mechanical Engineers, Part A: Journal of Power and Energy,* vol. 211, no. 4, pp. 331-338, 1997.

[44] R. H. Aungier, "Mean Streamline Aerodynamic Performance Analysis of Centrifugal Compressors," *Journal of Turbomachinery,* vol. 117, no. 3, pp. 360-366, 1995.

[45] M. R. Galvas, "Fortran Program for Predicting Off-Design Performance of Centrifugal Compressors," NASA Technical Note, 1973.

[46] P. Harley, S. Spence, J. Early, D. Filsinger and M. Dietrich, "An Evaluation of 1D Loss Model Collections for the Off-Design Performance Prediction of Automotive Turbocharger Compressors," *IOP Conference Series: Material Science and Engineering,* vol. 52, no. 4, p. IOP Publishing, 2013.

[47] F. Bozza and V. De Bellis, "Steady and Unsteady Modeling of Turbocharger Compressors for Automotive Engines," in *SAE Technical Paper 2010-01-1536*, 2010.

[48] J. Galindo, J. R. Serrano, H. Climent and A. Tiseira, "Experiments and Modeling of Surge in Small Centrifugal Compressors for Automotive Engines," *Journal of Experimental Thermal and Fluid Sciences,* vol. 32, no. 3, pp. 818-826, 2008.

[49] S. Marelli, A. Misley, A. Taylor, P. Silvestri, M. Canova and M. Capobianco, "Exprerimental Investigation on Surge Phenomena in an Automotive Turbocharger Compressor," in *SAE Technical Paper 2018-01-0976*, 2018.

[50] KAESER, "kompresory-chlazeni.cz," [Online]. Available: http://www.kompresory-chlazeni.cz/data/file/dokumenty/Kompresory-Kaeser45-75kW-CSD.pdf.

[51] Parker, "parker.com," [Online]. Available: https://www.parker.com/literature/Finite%20Airtek%20Filtration%20Division/PDF%20Static%20Files/ZANDER%20CAT/Zander%20GL%20Series%20High%20Efficiency%20Filters.pdf.

128

[52] CUSSONS TECHNOLOGY, "cussons.co.uk," [Online]. Available: https://www.cussons.co.uk/admin/resources/data-sheets/p7200-17-issue-3-1.pdf.

[53] Summit Dynamics, Inc., "sdiohio.com," 01 06 2005. [Online]. Available: http://www.sdiohio.com/Documents/Sylvania%20Heater%20Docs/SureHeat%20Max %20Operating%20Manual%202005%2003%2003.pdf.

[54] Unitech srl, "unitechsrl.com," [Online]. Available: http://www.unitechsrl.com/wp-content/uploads/2017/06/TF-1.pdf.

[55] Valpes, "valpes.fr," [Online]. Available: http://www.valpes.fr/pdf/documentation/valpes-ft-er-plus.pdf.

[56] S. Marelli et al., "Experimental Analysis on the Performance of a Turbocharger Compressor in the Unstable Operating Region and Close to the Surge Line," *Journal of Experimental Thermal and Fluid Science,* vol. 53, pp. 154-160, 2014.

[57] Italcoppie, "italcoppie.com," [Online]. Available: http://www.italcoppie.it/prodotto/trm200-it/.

[58] Italcoppie, "italcoppie.com," [Online]. Available: http://www.italcoppie.it/prodotto/tcmd-it/.

[59] Gems Sensors & Controls, "gemssensors.com," [Online]. Available: https://www.gemssensors.com/~/media/files/resources/na_english/catalogpages/catalog -h_2200series-2600series.ashx.

[60] S. Gandolfi, "Theoretical and Experimental Study of Road Vehicles Turbochargers Energetic Performance," Ph.D. Thesis, 2017.

[61] Kulite, "kulite.com," [Online]. Available: https://www.kulite.com/docs/products/XTEL-190.pdf.

[62] Kulite, "kulite.com," [Online]. Available: http://www.kulitesensors.com.cn/pdf_Data_Sheets/5-31/ETL-173-190.pdf.

[63] K. Semiconductor, "Data Sheet MINITUARE AUTOMOTIVE 5VDC OUTPUT IS PRESSURE TRANSDUCER ETL-173-190M".

[64] ABB, "abb.com," [Online]. Available: https://library.e.abb.com/public/f0b59b01c8d5ae40c1256a0d003b84a0/15_631sd.pdf.

[65] PRECISION MEASUREMENT TECHNOLOGIES, "pmt.com," [Online]. Available: https://www.pmt-fl.com/uploads/2017/09/precision-measurement-db-picoturnbm-e.pdf.

[66] ABB, "abb.com," [Online]. Available: https://library.e.abb.com/public/ee015c8c6af332ddc1257b0c00547f6c/42-14-40-EN-B-01_05.pdf.

129

[67] FLOMEC, "flomecmeters.com," [Online]. Available: https://flomecmeters.com/downloads/om-small-data-sheet.pdf.

[68] DANTEC DYNAMICS, "dantecdynamics.com," [Online]. Available: https://www.dantecdynamics.com/components/hot-wire-and-hot-film-probes/single-sensor-probes/fiber-film/.

[69] DANTEC DYNAMICS, "dantecdynamics.com," [Online]. Available: https://www.dantecdynamics.com/solutions-applications/solutions/fluid-mechanics/constant-temperature-anemometry-cta/minicta/.

[70] PCB PIEZOTRONICS, "pcb.com," [Online]. Available: https://www.pcb.com/products?m=352C33.

[71] Brüel & Kjær, "bskv.com," [Online]. Available: https://www.bksv.com/-/media/literature/Product-Data/bp2043.ashx.

[72] G.R.A.S. Sound & Vibration, "gras.dk," [Online]. Available: https://www.gras.dk/products/measurement-microphone-cartridge/prepolarized-cartridges-0-volt/product/ss_export/pdf2?product_id=150.

[73] G.R.A.S. Sound & Vibration, "gras.dk," [Online]. Available: https://www.gras.dk/files/p/d/pd_26ca_cs4_04022010.pdf.

[74] BELL Electronics, "bellnw.com," [Online]. Available: https://www.bellnw.com/downloads/datasheet/Agilent/34980A.pdf.

[75] National Instruments, "ni.com," [Online]. Available: http://www.ni.com/pdf/product-flyers/multifunction-io.pdf.

[76] National Instruments, "ni.com," [Online]. Available: https://www.ni.com/pdf/manuals/375212c.pdf.

[77] J. E. Coppage, et al., "Study of Supersonic Radial Compressors for Refrigeration and Pressurization Systems," WADC report: 55-257, 1956.

[78] J. W. Daily and R. E. Nece, "Chamber Dimension Effects on Induced Flow and Frictional Resistance of Enclosed Rotating Disks," *Trans. ASME, Journal of Basic Engineering,* vol. 82, pp. 217-232, 1960.

[79] W. Jansen, "A Method for Calculating the Flow in a Centrifugal Impeller when Entropy Gradients are Present," in *Royal Society Conference on Internal Aerodynamics (Turbomachinery)*, 1967.

[80] J. P. Johnston and R. C. Dean Jr, "Losses in Vaneless Diffusers of Centrifugal Compressors and Pumps," *Trans. ASME, Journal of Engineering for Power,* vol. 88, pp. 49-62, 1966.

[81] O. Dubitsky and D. Japickse, "Vaneless Diffuser Advanced Model," *Journal of Turbomachinery,* vol. 130, no. 1, 2008.

[82] D. Japickse, "Assessment of Signle- and Two-Zone Modeling of Centrifugal Compressors, Studies in Component Performance: Part 3," in *Proceedings of the ASME 1985 International Gas Turbine Conference and Exhibit. Volume 1: Aircraft Engine; Marine; Turbomachinery; Microturbines and Small Turbomachinery*, Houston, Texas, USA, 1985.

[83] S. Stockar, M. Canova, Y. Guezennec, A. Della Torre, G. Montenegro and A. Onorati, "Modeling Wave Action Effects in Internal Combustion Engine Air Path Systems: Comparison of Numerical and System Dynamics Approaches," *International Journal of Engine Reseach,* vol. 14, no. 4, pp. 391-408, 2013.

[84] S. Stockar, M. Canova, Y. Guezennec, A. Della Torre, G. Montenegro and A. Onorati, "Model-Order Reduction for Wave Propagation Dynamics in Internal Combustion Engine Air Path Systems," *International Journal of Engine Research,* vol. 16, no. 4, pp. 547-564, 2015.

[85] S. Stockar, M. Canova, Y. Guezennec and G. Rizzoni, "A Lumped-Parameter Modeling Methodology for One-Dimensional Hyperbolic Partial Differential Equations Describing Nonlinear Wave Propagation in Fluids," *Journal of Dynamic Systems, Measurement, and Control,* vol. 137, no. 1, pp. 1-11, 2014.

[86] S. Stockar, "Model-Order Reduction for Non-Linear Distributed Parameter Systems with Application to Internal Combustion Engine Modeling and Simulation," Ph.D. Dissertation, 2013.

[87] R. Holmes, M. J. Brennan and B. Gottrand, "Vibration of an Automotive Tubocharger - A Case Study," in *Proceeding of the 8th International Conference on Vibrations in Rotating Machinery*, Swansea, UK, 2004.

[88] M. Tanaka, K. Hatekenaka and K. Suzuki, "A Theoretical Analysis of Floating Bush Journal Bearings with Axial Oil Film Rupture Being Considered," *ASME Journal of Tribology,* vol. 124, no. 3, pp. 494-505, 2002.

[89] A. V. Oppenheim and R. W. Schafer, Discrete-Time Signal Processing, Upper Saddle River, NJ, USA: Prentice-Hall, 1999.

[90] N. Aretakis, K. Mathioudakis and K. Papailiou, "Turbocharger Unstable Operation Diagnosis Using Vibroacoustic Measurements," *ASME Transactions - Journal of Engineering for Gas Turbine and Power,* vol. 126, pp. 840-847, 2004.

[91] N. Hagino, K. Uda and Y. Kashiwabara, "Prediction and Active Control of Surge Inception of a Centrifugal Compressor," in *Proceeding of the International Gas Turbine Congress*, 2003.

[92] M. L. Ferrari, P. Silvestri, M. Pascenti, F. Reggio and A. F. Massardo, "Experimental Dynamic Analysis on a T100 Microturbine Connected with Different Volume Sizes," *ASME Transactions - Journal of Engineering for Gas Turbine and Power,* vol. 140, pp. 021701-1-12, 2018.

[93] F. Satta, D. Simoni, M. Ubaldi, P. Zunino and F. Bertini, "Synthetic Jet Design Criteria and Application for Boundary Layer Separation," in *WSEAS Transactions on Fluid Mechanics*, 2010.

[94] S. Marelli, A. Misley and M. Ferrando, "Experimental Investigation in Turbocharger Compressors during Surge Operation," in *ASME Turbo Expo 2020*, London, 2020.

[95] A. Misley, A. Taylor, M. Canova, S. Marelli and M. Capobianco, "A Physics-Based, Control-Oriented Turbocharger Compressor Model for the Prediction of Pressure Ratio at the Limit of Stable Operations," in *SAE Technical Paper 2019-01-0320*, 2019.

[96] D. A. Fink, H. P. Dickmann and R. Emmerich, "Numerical and Experimental Investigation of a Centrifugal Compressor with an Inducer Casing Bleed System," *Proceeding of the Institution of Mechanical Engineers, Part A: Journal of Power and Energy,* vol. 215, pp. 783-791, 2001.

A Appendix: Details of Test Bench and Measurement Equipment

A.1. Test Bench Details

Fig. A.1 shows a picture of the KAESER compressor, which is one of the three compressor part of the lab's compression unit.
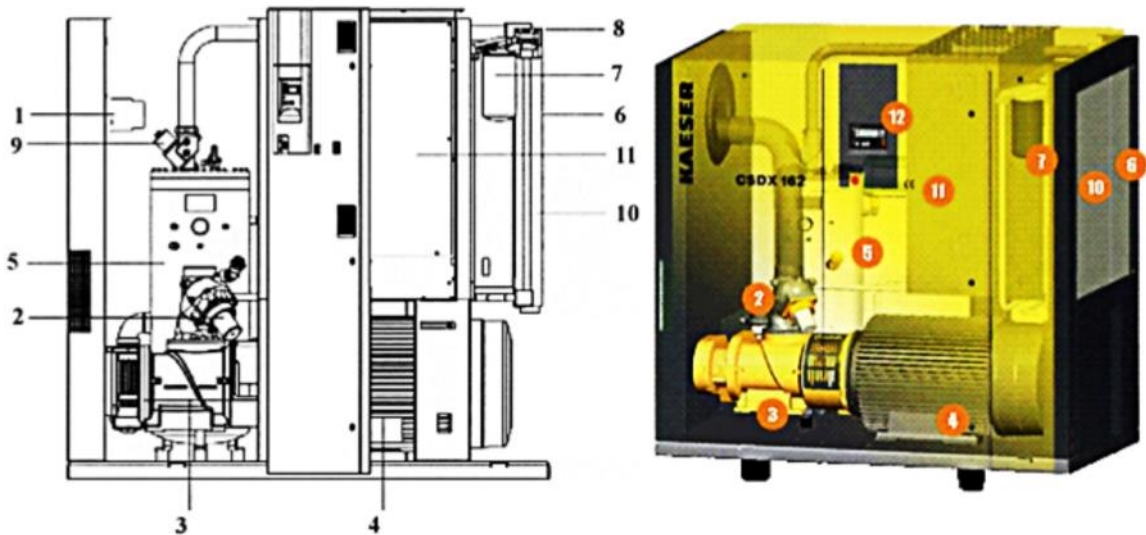
1	Inlet filter	7	Oil filter
2	Air inlet valve	8	Thermostatic valve
3	Screw compressor	9	Control valve
4	Electric motor	10	Heat exchanger
5	Air-oil separator	11	Electrical panel
6	Cooler	12	Sigma control system

Fig. A.1 – KAESER Screw Compressor [60]

Fig. A.2 shows the schematic of the whole lab. Segments of Fig. A.2 are shown in Chapter 0, Section 2.1, Test Bench Description. Tab. A.1 is the legend for the schematic of the test lab, shown in Fig. A.2, and for Fig. 2.2, Fig. 2.3, Fig. 2.5 and Fig. 2.6.
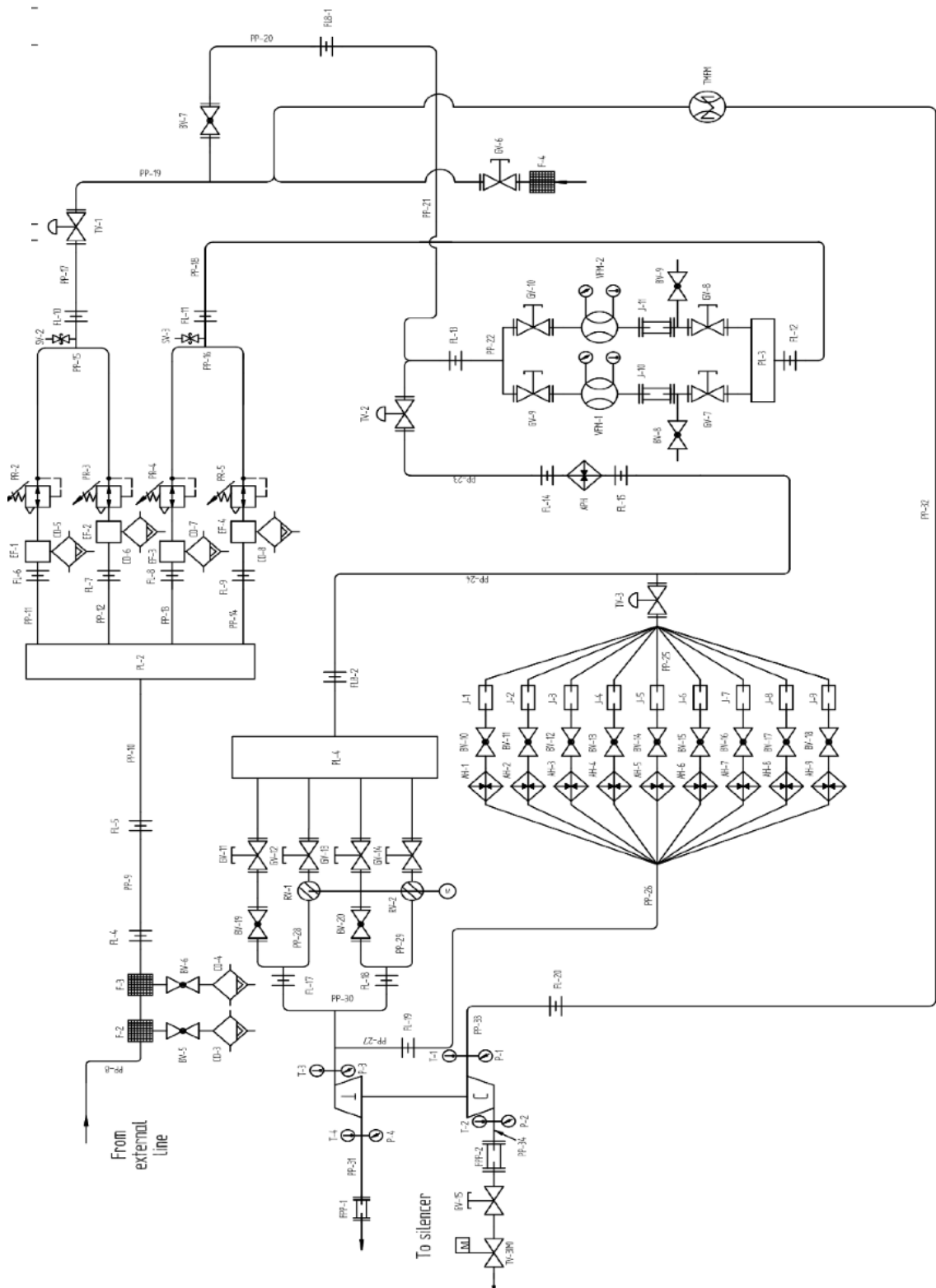
Fig. A.2 – Lab Schematic Representation

Acronym	Significance	Symbol
AD	Air Drier	
AH	Air Heater	
APH	Air Pre-heater	
BV	Ball Valve	
CD	Condense Discharger	
EF	Empty Filter	
F	Filter	
FL	Flange	
FPP	Flexible Pipe	
GV	Gate Valve	
J	Joint	
M	Motor	
P	Pressure	
PL	Plenum	
PP	Pipe	
PR	Pressure Regulator	
RV	Rotating Valve	
SC	Screw	
SV	Safety Valve	
T	Temperature	
TMFM	Thermal Mass Flow Meter	
TV	Throttle Valve	
VFM	Viscous Flow Meter	

(M) indicates a motorized component

Tab. A.1 – Legend for Fig. 2.2, Fig. 2.3, Fig. 2.5 and Fig. 2.6

Fig. A.3 shows the electrical heater element located in the hot air line, part of the turbine feeding line described in section 2.1.2.2, Turbine Feeding Line.

Fig. A.3 – A Single Electrical Heater Element and Electro-Pneumatic Valve

A.2. Measuring Equipment Details

Fig. A.4 and Fig. A.5 show an image of the resistance thermometers and of the thermocouples, used during tests and described in 2.2.2, Temperature Measurements.

Fig. A.4 – Pt100 Resistance Thermometers [57]

Fig. A.5 – K-Type Thermocouple [58]

Tab. A.2 lists all the characteristics of the pressure sensors described in section 2.2.3, Pressure Measurements.

CODE	MANUFACTURER	MODEL	RANGE	PRESSURE CONNECTION	TEMP. COMPENS.	OUTPUT VOLTAGE	ACCURACY
7.01	Gems Sensors	2600SGA2500G3UB	0÷2.5 bar VG	G 1/4" (f)	-54÷120 °C	10V±1mV	±0.15% f.s.
7.02	Gems Sensors	2600SGA2500G3UB	0÷2.5 bar VG	G 1/4" (f)	-54÷120 °C	10V±1mV	±0.15% f.s.
7.03	Gems Sensors	2600SGA2500G3UB	0÷2.5 bar VG	G 1/4" (f)	-54÷120 °C	10V±1mV	±0.15% f.s.
7.04	Gems Sensors	2600SGA4000G3UB	0÷4 bar VG	G 1/4" (f)	-54÷123 °C	10V±1mV	±0.15% f.s.
7.05	Gems Sensors	2600SGA4000G3UB	0÷4 bar VG	G 1/4" (f)	-54÷123 °C	10V±1mV	±0.15% f.s.
7.06	Sensing & Inspection Technologies	A5076TBA2CAHOPA	0÷2.5 bar VG	G 1/4" (f)	-20÷80 °C	10V±1mV	±0.1% f.s.
7.07	Sensing & Inspection Technologies	A5076TBA2CAHOPA	0÷2.5 bar VG	G 1/4" (f)	-20÷80 °C	10V±1mV	±0.1% f.s.
7.08	Sensing & Inspection Technologies	A5076TBA2CAHOPA	0÷4 bar VG	G 1/4" (f)	-20÷80 °C	10V±1mV	±0.1% f.s.
7.09	Sensing & Inspection Technologies	A5076TBA2CAHOPA	0÷4 bar VG	G 1/4" (f)	-20÷80 °C	10V±1mV	±0.1% f.s.
7.10	Sensing & Inspection Technologies	A5076TBA2CAHOPA	0÷0.35 bar VG	G 1/4" (f)	-20÷80 °C	10V±1mV	±0.1% f.s.
7.11	Sensing & Inspection Technologies	A5076TBA2CAHOPA	0÷0.35 bar VG	G 1/4" (f)	-20÷80 °C	10V±1mV	±0.1% f.s.
7.12	Sensing & Inspection Technologies	A5076TBA2CAHOPA	0÷0.35 bar VG	G 1/4" (f)	-20÷80 °C	10V±1mV	±0.1% f.s.
7.13	Sensing & Inspection Technologies	A5076TBA2CAHOPA	0÷0.35 bar VG	G 1/4" (f)	-20÷80 °C	10V±1mV	±0.1% f.s.
7.14	Kulite Semiconductor	XTEL-37-IA-190M-65PSIG	0÷4.48 bar G	M5 (m)	25÷232 °C	500mV±50mV	±0.1% f.s.
7.15	Kulite Semiconductor	XTEL-37-IA-190M-65PSIG	0÷4.48 bar G	M5 (m)	25÷232 °C	500mV±50mV	±0.1% f.s.
7.16	Kulite Semiconductor	XTEL-37-IA-190M-65PSIG	0÷4.48 bar G	M5 (m)	25÷232 °C	500mV±50mV	±0.1% f.s.
7.17	Kulite Semiconductor	XTEL-37-IA-190M-65PSIG	0÷4.48 bar G	M5 (m)	25÷232 °C	500mV±50mV	±0.1% f.s.
7.18	Kulite Semiconductor	XTEL-37-IA-190M-65PSIG	0÷4.48 bar G	M5 (m)	25÷232 °C	500mV±50mV	±0.1% f.s.
7.19	Kulite Semiconductor	XTEL-37-IA-190M-65PSIG	0÷4.48 bar G	M5 (m)	25÷232 °C	500mV±50mV	±0.1% f.s.
7.20	Kulite Semiconductor	XTEL-37-IA-190M-65PSIG	0÷4.48 bar G	M5 (m)	25÷232 °C	500mV±50mV	±0.1% f.s.
7.21	Kulite Semiconductor	ETL-173-190M-2BARA	0÷2 bar A	M5 (m)	20÷120 °C	500mV±50mV	±0.1% f.s.
7.22	Kulite Semiconductor	ETL-173-190M-1.7BARA	0÷1.7 bar A	M5 (m)	-40÷177 °C	500mV±50mV	±0.1% f.s.
7.23	Kulite Semiconductor	ETL-175-190M-1.7BARA	0÷1.7 bar A	M5 (m)	-40÷177 °C	500mV±50mV	±0.1% f.s.

Tab. A.2 – Pressure Sensors' Characteristics

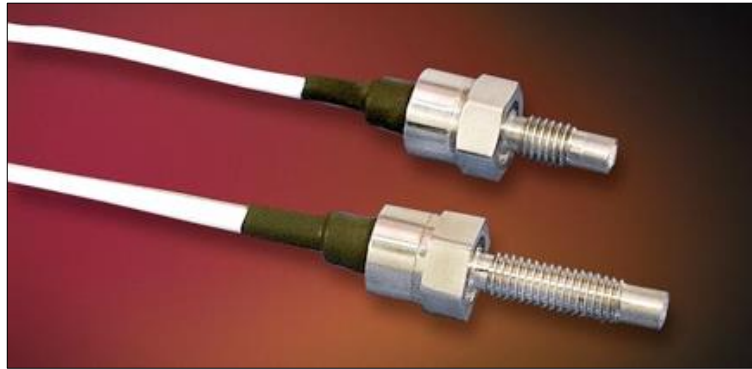Fig. A.6 and Fig. A.7 show an image and the drawing of the Kulite Semicondutor sensor model XTEL-37-IA-190M-65PSIG.
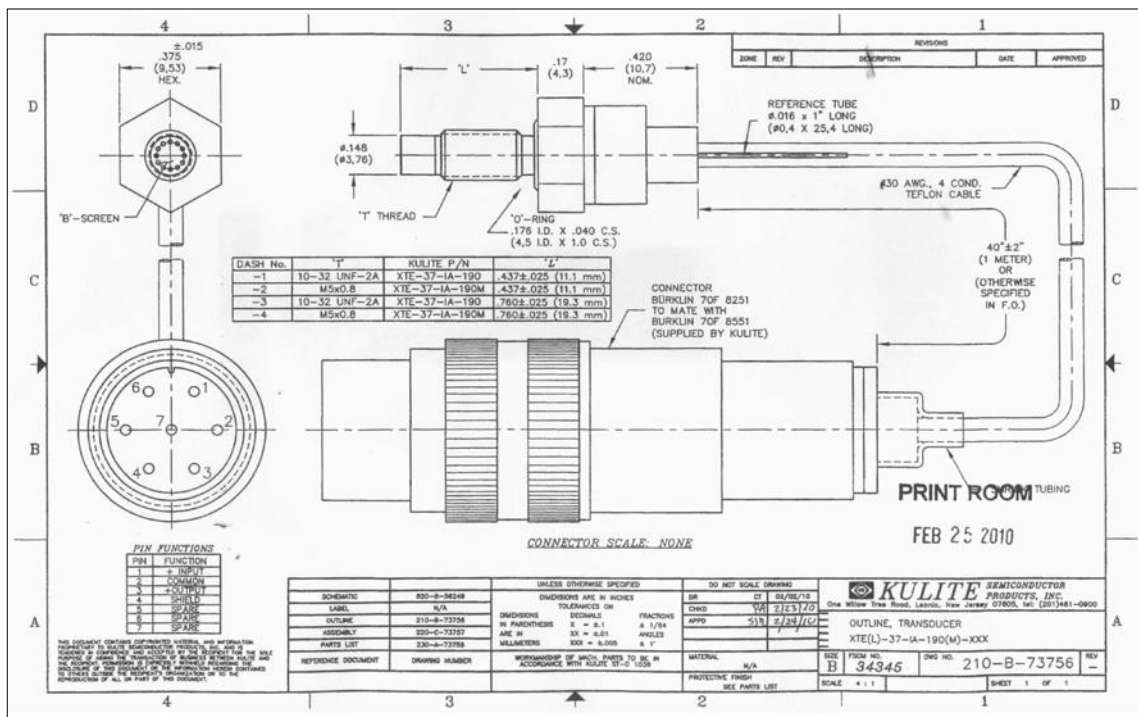
137

Fig. A.6 – Kulite Sensors [61]

Fig. A.7 – Schematic Representation of Kulite Transducers [61]

Fig. A.8 shows the thermal mass flow meter used for the measurement of the compressor mass flow rate and described in section 2.2.5, Flow Rate Measurements.

Fig. A.8 – ABB Sensyflow FTM500-IG [66]

Fig. A.9 and Fig. A.10 show the two types of accelerometers used during the tests and describe in section 2.2.6, Vibration Measurements.

Fig. A.9 – Accelerometer PCB 352C33 [70]

Fig. A.10 – Accelerometer Brüel & Kjær type 4393 [71]

Fig. A.11 and Fig. A.12 show the two types of accelerometers used during the tests and describe in section 2.2.7, Acoustic Measurements.

Fig. A.11 – Microphone G.R.A.S. 40AE 1/2" [72]

Fig. A.12 – Microphone G.R.A.S. 26CA 1/2" CCP [45]

Fig. A.13 shows the data acquisition system used for the acquisition of time-averaged data and described in Section 2.3, Acquisition System.

Fig. A.13 – AGILENT 34980A Data Acquisition System [74]

Details on TURBO acquisition code

The acquisition code TURBO requires a number of input files with a specific identification. Input and output files are defined through a technique previously established by the research group which allows the operator to easily identify the tested components and the type of test. For this reason, the component number (nt) and the test configuration (cfg) need to be specified before the start of a test. The test number (ppp), the test point (p) and the number of measurements for each test point (m) also need to be provided.

The input files are:

- CONFIG_nt_cfg.txt contains general information on the test,

- CANALI_nt_cfg.txt contains information on the measured parameters with the respective measurements channel number and sensor code,

- DIMGRUPPO_nt_cfg.txt contains information on the tested turbocharger's geometric characteristics and dimensions;

- VIELABORAZIONE_nt_cfg.txt contains a list of the Virtual Instruments (sub-Vis) used for the first phase of data post-processing;

- TRASDUTTORI AMPLIFICATI.txt contains the calibration coefficients for all pressure sensors;

- FATTORE DI VISCOSITÀ.txt allows the software to calculate the mass flow rate value from the laminar mass flow meter signal.

The code provides as output files:

140

- V_nt_ppp_p_m.txt is created after the acquisition of each measurement and records the different readings of the measures used to more accurately calculatedly the average value,

- T_nt_ppp.txt contains the values of the quantities that were directly measured (i.e. total temperature and static pressure) and the ones derived from the measured quantities (i.e. power and efficiency);

- CFG_nt_ppp.txt: contains general information on the test.